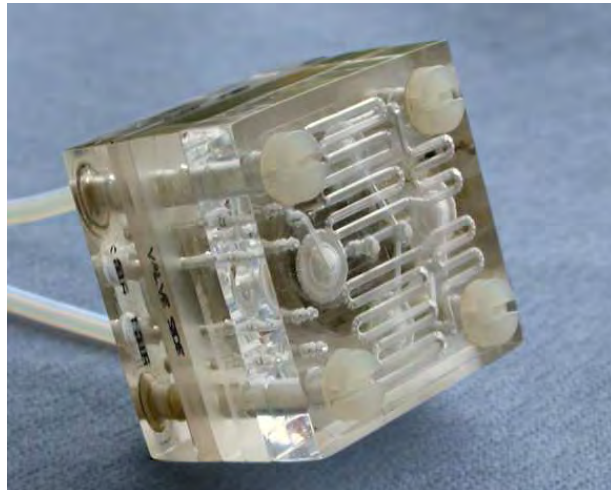


Electroosmotic micropumps

Anders Brask



Main supervisor: Henrik Bruus
Co-supervisor: Jörg P. Kutter

MIC – Department of Micro and Nanotechnology
Technical University of Denmark

31 August 2005

Abstract

The goal of this thesis has been to develop electroosmotic pumping technology in relation to micro total analysis systems (μ TAS), also known as lab-on-chip systems. The present micropump technologies do not offer compact, reliable and low-cost pumping solutions. Micropumps based on electroosmosis are believed to have the potential of reaching that goal. This thesis therefore covers the development of polymer based electroosmotic micropumps and valve systems. Different aspects of design, theoretical calculations, fabrication and characterization are covered.

The presented pumps are powered by electricity in three different ways or modes: (1) Direct current operation (DC EO), (2) low-frequency alternating current (AC EO) and (3) high-frequency induced-charge (IC EO). During the project, one DC EO, two AC EO and two IC EO pumps have been developed. The main focus has been on the DC EO and AC EO pumps. The following flow rate and pressure characteristics have been obtained at an applied voltage of $\Delta V = 30$ V: The DC EO pump achieved $\Delta p_m = 4.5$ bar and $Q_m = 6 \mu\text{L min}^{-1}$ whereas the AC EO pump achieved $\Delta p_m = 2.0$ bar and $Q_m = 10 \mu\text{L min}^{-1}$ with a period of $T = 90$ s. The flow characteristics have been obtained through several hours of continuous testing.

Micropumps, in particular electroosmotic micropumps, are usually not very reliable so this has also been an important factor in this project. A significant effort has been devoted to increasing the reliability and reducing the required maintenance of the EO pumps. Several new technologies were developed: (1) The use of ion exchange membranes enabled free ventilation of electrolytic gases. (2) An engineered flow pattern improved the ion transport and hence the EO flow in the DC EO pump. (3) AC operation of an EO pump enabled bubble-free electrodes and the possibility of rendering the pump independent of the pumped liquid. (4) Two different valve systems were developed, both capable of rectifying a pulsating microflow. (5) Finally, an integrated induced-charge EO pump was designed and successfully tested.

All of the above described technologies aim to improve EO based micropump technology, and thereby making the goal of a reliable, compact and low-cost micropump more feasible.

Resumé

Formålet med denne afhandling har været at udvikle pumpeteknologi baseret på elektroosmose (EO) i forbindelse med mikrosystemer. Disse systemer går også under navnet *micro total analysis systems* (μ TAS) eller *lab-on-chip* systemer. De nuværende pumpeteknologier kan ikke tilbyde kompakte, pålidelige og billige pumpeløsninger. Man tror, at mikropumper baseret på elektroosmose vil kunne indfri dette mål. Denne afhandling beskriver derfor udviklingen af polymerbaserede elektroosmotiske pumper og ventilsystemer. Afhandlingen dækker mange forskellige områder såsom design, teoretiske beregninger, fabrikation og karakterisering.

De udviklede pumper er alle drevet af elektricitet men på tre forskellige måder: (1) Jævnstrøm (DC EO), (2) lavfrekvent vekselstrøm (AC EO) eller (3) højfrekvent induceret ladning (IC EO). I løbet af projektet er der blevet udviklet 1 DC EO-, 2 AC EO- og 2 IC EO pumper. Fokuset har i langt overvejende grad været på DC EO- og AC EO pumperne. De følgende pumpekaraktistiker er opnået ved en spænding på $\Delta V = 30$ V: DC EO pumpen opnåede $\Delta p_m = 4.5$ bar og $Q_m = 6 \mu\text{L min}^{-1}$ hvorimod AC EO pumpen opnåede $\Delta p_m = 2.0$ bar og $Q_m = 10 \mu\text{L min}^{-1}$ med en periode på $T = 90$ s. Pumpekaraktistikerne blev opnået igennem kontinuerlige tests over flere timer.

Generelt er mikropumper ikke særlig pålidelige. Elektroosmotiske pumper er ingen undtagelse for denne regel. Derfor har stabilitet været en høj prioritet i dette projekt. Der er blevet gjort en stor indsats for at forbedre stabiliteten og mindske den nødvendige vedligeholdelse af pumperne. I den forbindelse blev flere nye teknologier udviklet: (1) Ionbyttermembraner muliggjorde ventilation af de dannede elektrodegasser, (2) et ændret strømningsmønster forbedrede iontransporten og dermed det elektroosmotiske flow i DC EO pumpen, (3) brugen af AC strøm muliggjorde brugen af boblefri palladium elektroder. Endvidere er det teoretisk muligt at gøre pumpen uafhængig af den pumpede væske, (4) to forskellige ventilsystemer blev udviklet og testet. Begge var istand til at ensrette et mikropulserende flow (5) og til sidst blev der designet og testet en induceret-ladning EO pumpe.

Alle de ovenstående teknologier sigter mod at forbedre EO baserede mikropumper. Tanken er at komme tættere på målet med en pålidelig, kompakt og billig mikropumpe.

Preface

This thesis is written as a requirement for obtaining the PhD degree at the Technical University of Denmark (DTU). The PhD project was performed at MIC – Department of Micro and Nanotechnology, DTU, from September 2002 to September 2005, within the Microfluidic Theory and Simulation group (MIFTS). In the period from February to July 2004, I worked in the Microfluidics group at the University of Michigan in Ann Arbor, MI, USA. The PhD project was supervised by Prof. Henrik Bruus (main supervisor), Assoc. Prof. Jörg P. Kutter and while abroad by Assoc. Prof. Ernest F. (Charlie) Hasselbrink and Prof. Henrik Bruus.

The PhD project had a good starting point because of my theoretical master thesis entitled *Principles of electroosmotic pumps*. I soon realized that theory and experiments are two very different things but nevertheless my theoretical background helped me tremendously throughout the project.

I would like to thank the people in μ TAS here at MIC, especially Detlef Snakenborg for good friendship and assistance in the laboratory. I would also like to thank the microfluidics group at the University of Michigan and especially Meng-Ping Chang for his help with the fabrication of microvalves. My appreciation also goes to Charlie Hasselbrink for his supervision and for making me feel welcome in the research group. Torben Jacobsen from the Department of Chemistry also deserves credit for setting up a special course on *Electrokinetic transport in membranes* and for helpful discussions about electrochemistry. I would also like to thank my supervisors for our inspiring weekly meetings and the people in the MIFTS cave for listening to a not insignificant amount of nonwork related stories. Finally I would like to thank my family and friends for their encouragement and support.

Anders Brask
MIC – Department of Micro and Nanotechnology
Technical University of Denmark
31 August 2005

Contents

List of figures	xv
List of tables	xvii
List of symbols	xix
1 Introduction	1
1.1 μ TAS	1
1.2 Micropumps	1
1.3 Electroosmotic micropumps	2
1.4 Outline of the thesis	3
1.5 Publications during the project	5
2 DC electroosmotic pump	7
2.1 Introduction	7
2.2 A. Brask <i>et al.</i> , Lab Chip, 2005, 5, 730-738	7
2.2.1 Introduction	8
2.2.2 A model of EO flow in a frit	8
2.2.3 The design	10
2.2.4 Fabrication	12
2.2.5 Measurements	14
2.2.6 Results	18
2.2.7 Conclusion	23
3 Additional material for the DC EO pump	25
3.1 The frit	25
3.1.1 Surface preparation	26
3.1.2 Pore size	26
3.1.3 The frit mount	27
3.2 Ion exchange membranes	27
3.2.1 Selectivity and strength	28
3.2.2 Handling of the membranes	28
3.2.3 Reverse osmosis	29
3.3 Limiting current density	29

3.3.1	Limiting current theory	29
3.3.2	Boundary layer experiments	30
3.4	Sealing and fluidic connections	32
3.5	Buffer conductivity and pH	33
3.5.1	Ion transport	35
3.6	Theoretical flow characteristics	36
3.6.1	Debye layer overlap	36
3.6.2	Relation between flow and electrical current	37
4	Microvalves overview	41
4.1	Valve parameters	41
4.1.1	Flow resistance and diodicity	41
4.1.2	Internal volume	42
4.1.3	Opening pressure	42
4.1.4	Valve history	42
4.1.5	Robustness	42
4.2	Duckbill and umbrella valves	43
4.3	Foam valve	44
4.4	Membrane slit valve	45
4.5	Mobile polymer plug valve	46
5	AC EO pump with membrane valves	47
5.1	Introduction	47
5.2	A. Brask <i>et al.</i> , Lab Chip, 2006, 6, 280-288	47
5.2.1	Introduction	48
5.2.2	General concept	49
5.2.3	EO actuator	50
5.2.4	Bubble-free electrodes	50
5.2.5	Valve system	52
5.2.6	Integration issues	58
5.2.7	Pump characteristics	60
5.2.8	Outlook	63
5.2.9	Conclusion	63
6	Additional material for the AC EO pump	65
6.1	Bubble-free electrodes	65
6.2	Valve and membrane material testing	66
6.3	Automated valve testing setup	68
6.4	The reservoir and separator module	69
6.5	Design and fabrication	70
6.5.1	Computer aided design	70
6.5.2	Fabrication of the layers	71
6.5.3	Bonding and alignment	72

7	AC EO pump with mobile plug valves	73
7.1	General	73
7.2	EO Actuator with bubble-free electrodes	73
7.3	Valve system	74
7.3.1	Valve chip fabrication	75
7.3.2	Customizing the polymer compound	77
7.3.3	Loading the polymer solution	79
7.3.4	Controlling the exposure	80
7.3.5	Valve characterization	83
7.4	Pump characteristics	85
7.5	Conclusion	86
8	Additional pump projects	89
8.1	The two-liquid viscous EO pump	89
8.1.1	Background	89
8.1.2	Introduction	90
8.1.3	Pressure valves	90
8.1.4	Conclusion	91
8.2	Equivalent circuit theory	91
8.2.1	Background	91
8.2.2	Introduction	92
8.2.3	Analysis of the EO pump	93
8.2.4	Fluidic network model	94
8.2.5	Conclusion	95
8.3	Induced-charge EO pumping	96
8.3.1	Background	96
8.3.2	Introduction	96
8.3.3	First IC EO pump generation	96
8.3.4	Second IC EO pump generation	96
8.3.5	Conclusion	98
9	Outlook and conclusion	99
A	Equivalent circuit theory	103
B	Experimental setup	107
C	Paper published in J. Micromech. Microeng.	111
D	Paper published in Sens. Actuators B	121
	Bibliography	129

List of Figures

1.1	Electroosmotic effect	2
2.1	Sketch of the frit	9
2.2	Schematic view of the functional components in the DC EO pump	9
2.3	Concentration profiles in the vicinity of an ion exchange membrane	12
2.4	Picture of the DC EO pump	13
2.5	Diagram of the experimental setup	14
2.6	Flow diagram of the flushing system	15
2.7	Data recorded during a pump test	17
2.8	Q - p characteristics with 5 mM buffer	18
2.9	All Q - p characteristics	19
2.10	Decay of current	20
2.11	Flow rate vs. current	21
2.12	Current dependence on backpressure	22
2.13	SEM picture of the nanoporous frit	23
3.1	SEM pictures of the microporous frit	26
3.2	Inner loop in DC EO pump	27
3.3	Limiting current experimental setup	31
3.4	Current vs. voltage	32
3.5	Different versions of feed systems	32
3.6	Tube mounting	33
3.7	Buffer capacity, titration of borax	34
3.8	EO mobility dependence on concentration and pH	34
3.9	Ion balance	36
3.10	Theoretical model of EO flow with finite Debye layers	37
3.11	Theoretical current regulation	39
4.1	Schematic of internal volume	42
4.2	Duckbill and umbrella valves	43
4.3	Schematics of foam valve	44
4.4	Pictures of foam valve	44
4.5	3D illustration of membrane valve	45
4.6	Illustration of the plug valve principle	46

5.1	Diagram of rectifying bridge	49
5.2	Bubble formation - simulation and experiments	51
5.3	Membrane valve	53
5.4	Picture of four-way valve system	55
5.5	Picture of cut tool	55
5.6	Diagram of the valve test setup	56
5.7	Examples of valve test configurations	56
5.8	Q - p characteristics	57
5.9	Opening pressure vs. cavity dia.	58
5.10	Picture of the assembled pump	59
5.11	Pump characteristics, Q vs. t	61
5.12	Pump characteristics, Q vs. T	62
5.13	Pump characteristics, phase lag	63
6.1	Young's modulus measurements	67
6.2	Membrane deflection vs. thickness	67
6.3	Picture of the valve test setup	68
6.4	Picture support and reservoir chip	69
6.5	AC EO pump components	71
6.6	Picture of alignment and bonding setup	72
7.1	Picture of the AC EO with mobile plug valves	74
7.2	Mobile plug valve	75
7.3	Fabrication of valve chip	76
7.4	Nanoport fittings	77
7.5	Dimensions of the valve system	78
7.6	Plug deformities	80
7.7	Optical path	81
7.8	Optical boom	82
7.9	Exposure region	82
7.10	Plug length	83
7.11	Microvalves with polymer plugs	85
7.12	Q - p characteristics AC plug valve	86
7.13	Flow rate vs. period	87
8.1	Schematics of the two-liquid viscous EO pump	90
8.2	Schematics of the low-voltage cascade EO pump	92
8.3	Schematic of one step in the low-voltage cascade EO pump	93
8.4	Equivalent circuit model, low-voltage cascade EO pump	94
8.5	Picture of 1st generation of IC EO pump	97
8.6	Picture of 2nd generation of IC EO pumps	97
8.7	Picture of 2nd generation of IC EO pump in chip holder	98
A.1	Circuit model of AC EO pump with compliance	104
A.2	Simulation results from circuit theory	105

A.3	Model of plug valve resistance	106
B.1	Diagram of the electrical setup	108
B.2	Labview program - constant voltage	108
B.3	Hydraulic resistance measurement setup	109
B.4	Labview program	109
B.5	Labview program	110

List of Tables

1.1	EO pump issues	3
2.1	Complete list of DC EO pump experiments	16
2.2	Pore size estimates	23
3.1	Frit properties	25
3.2	List of ion exchange membranes tested	28
3.3	Buffer conductivities	33
3.4	Electrode reactions	35
5.1	Calculations of the membrane deflection	53
5.2	Membrane deflection ratio	58
7.1	List of ingredients in the polymer compound	78
7.2	Plug valve system 1	84
7.3	Plug valve system 2	85
7.4	Plug valve system 3	85
8.1	Hydraulic resistances for different cross sectional shapes	95
A.1	Equivalent circuit theory	103

List of symbols

Symbol	Description	Unit
a	Pore radius	m
A	Cross sectional area	m^2
c	Concentration	mol m^{-3}
D	Mass diffusion	$\text{m}^2 \text{s}^{-1}$
e	Elementary charge	$1.602 \times 10^{-19} \text{ C}$
E	Young's modulus	$\text{N m}^{-2} = \text{Pa}$
f	Frequency	$\text{Hz} = \text{s}^{-1}$
F	Faraday constant	$9.649 \times 10^4 \text{ C mol}^{-1}$
i	Current density	A m^{-2}
I	Electrical current	A
j	Molar flux	$\text{mol s}^{-1} \text{m}^{-2}$
k	Boltzmann constant	$1.381 \times 10^{-23} \text{ J K}^{-1}$
ℓ	Boundary layer thickness	m
K	Compliance	$\text{m}^3 \text{Pa}^{-1} = \text{m}^4 \text{kg}^{-1} \text{s}^2$
m	Mass	kg
n	Molar amount	mol
p	Pressure	$\text{Pa} = 10^{-5} \text{ bar}$
Δp_m	Maximum backpressure	$\text{Pa} = 10^{-5} \text{ bar}$
Q	Volume flow rate	$\text{m}^3 \text{s}^{-1}$
Q_m	Maximum flow rate	$\text{m}^3 \text{s}^{-1}$
R	Gas constant	$8.315 \text{ J mol}^{-1} \text{K}^{-1}$
R_{hyd}	Hydraulic resistance	$\text{kg m}^{-4} \text{s}^{-1}$
T	Period	s
u	Velocity	m s^{-1}
u_d	Deflection	m
\mathcal{V}	Volume	m^3
ΔV	Applied potential	V
z	Signed ion valence	

Symbol	Description	Unit
α_{eo}	Electroosmotic mobility	$\text{m}^2 (\text{V s})^{-1}$
ϵ_0	Dielectricity constant	$8.854 \times 10^{-12} \text{ F m}^{-1}$
ζ	Potential at shear interface	V
η	Thermodynamic efficiency	
λ_D	Debye length	m
μ	Dynamic viscosity	$\text{kg m}^{-1} \text{ s}^{-1}$
ν	Kinematic viscosity	$\text{m}^2 \text{ s}^{-1}$
ν_p	Poisson's ratio	
ρ	Mass density	kg m^{-3}
ϕ	Electric potential	V
ψ	Porosity	

Chapter 1

Introduction

1.1 μ TAS

The concept of micro total analysis systems (μ TAS) refers to devices capable of controlling and manipulating fluid flows with length scales less than a millimeter, [1]. The concept, originating from the early nineties, was originally developed by Manz *et al.* as a means to increase the performance of analytical chemistry, [2]. Later the field expanded to also involve biological systems due to the large commercial interest within this area. Complex microsystems are also denoted lab-on-a-chip systems. These systems usually require one or more micropumps to control the fluids. However, it has proven very difficult to integrate micropumps in lab-on-chip systems. In many cases the pumping is therefore done by external laboratory pumps. An obvious improvement would be to use external micropumps instead. This would reduce the size and cost of these systems considerably. In some cases a micropump will also be superior to a laboratory pump with respect to response time and accuracy.

1.2 Micropumps

We can divide micropumps into two major categories: (1) Displacement pumps, which exert a force on the working fluid through a moving boundary and (2) dynamic pumps, which continuously add energy to the working fluid in a manner that increases its momentum or pressure directly, [3]. Electroosmotic pumps belong to the category of dynamic pumps. Here the electric field exerts a force on the charged liquid and thereby increases its momentum or pressure. A typical displacement micropump has three key elements: (1) A diaphragm actuated by, e.g., piezoelectric, electrostatic or thermopneumatic principles. (2) A valve system achieved by, e.g., flap valves, membrane valves or diffuser-nozzle valves. (3) Chambers, either a single or multiple chambers (peristaltic pump). Displacement micropumps are often very sensitive to particles because of the microvalves. A particle may get stuck in a flap valve rendering it permanently open. Another issue is the bubble sensitivity. If a bubble is trapped in the displacement chamber the added compliance will decrease the performance of the pump dramatically. Pumps of this nature are beginning to

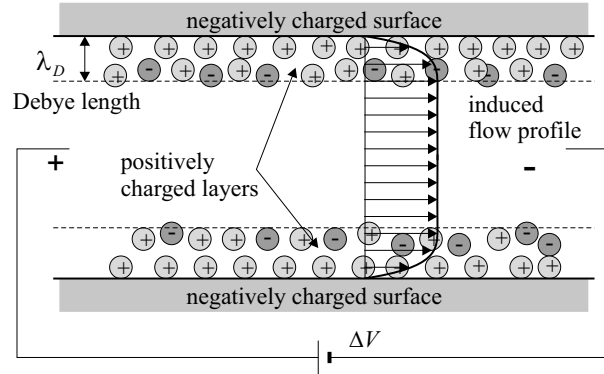


Figure 1.1: Schematic illustration of electroosmotic (EO) flow in a channel. The two electrodes generate an electric field that exerts a force on the charged Debye layers, $\lambda_D = 1 - 100$ nm. In the stationary state this force is balanced by the viscous shear force.

become available for purchase. Reliability and cost are, however, still the main concerns.

1.3 Electroosmotic micropumps

Electroosmosis was discovered in 1809 by the Russian physicist Reuss and in 1897 the theoretical aspects of the electrokinetic phenomena were investigated by Kohlrausch, [4]. Today, people most often quote Hunter, Probstein, Rice and Whitehead as fundamental sources for electrokinetic theory, [5, 6, 7].

Electroosmosis is an electrokinetic effect, which can be used for pumping in small channels, i.e., when the surface-to-volume ratio is large, see Fig. 1.1. Consider a channel filled with an electrolyte. Ions in the liquid form a thin ($\lambda_D = 1 - 100$ nm) electric double layer, denoted the Debye layer, at the walls of the channel due to chemical interactions. An electric potential drop ΔV applied along the channel will exert a force on the charged Debye layers. The force will accelerate the ions and hence the liquid until the viscous shear force balances the applied electrical force. The terminal velocity is denoted the Helmholtz-Smoluchowski velocity u_{eo} , and it is given by

$$u_{eo} = \alpha_{eo} E, \quad (1.1)$$

$$\alpha_{eo} = -\frac{\epsilon \zeta}{\mu}, \quad (1.2)$$

where α_{eo} is the electroosmotic mobility, E the electric field, ϵ the liquids dielectricity constant, ζ the surface potential at the shear interface and μ the dynamic viscosity of the liquid. For more details on the principles of electroosmotic pumps the reader is referred to Brask, [8].

Electroosmotic pumps are suitable for applications where high pressures are needed $\Delta p_m = 10^{-1} - 10^2$ bar. Other types of micropumps usually generate much lower pressures $\Delta p_m = 10^{-3} - 10^0$ bar. An EO induced pressure as high as $\Delta p_m = 83$ bar has been reported by Mosier *et al.*, [9]. The achievable EO driven flow rates are typically similar or

smaller $Q_m = 10^{-2} - 10^1 \mu\text{L s}^{-1}$ compared to other micropumps. This is obviously highly dependent on the applied voltage and on the size of the given micropump. A direct current (DC) EO pump does not contain any moving parts and can produce a silent non-pulsating flow. Another advantage is that the simplicity of an EO pump enables low production cost. In Sec. 2.2.1 more DC EO pump history is given.

Although EO pumping has been around for more than a decade there are still many unsolved issues associated with the pumping method. The purpose of this thesis is to investigate these issues and to solve as many of them as possible thereby evaluating the potential of EO pumping in microfluidics. In Table 1.1 some of the most challenging issues are presented.

issue
1. The EO flow is very dependent on the properties of the pumped liquid
2. The pumped liquid must pass through a sub-micron structure acting as a filter
3. The efficiency of the pump is very low, typically less than 1%
4. The electrodes generate gases that can interfere with the operation
5. The EO pumping effect degrades over time

Table 1.1: List of issues associated with traditional DC EO pumping

In an inline DC EO pump the liquid passes through a sub-micron structure. A small spatial dimension is essential for generating high pressure. In addition, the EO mobility α_{eo} is dependent on the pumped liquid. Issues (1-3) are therefore inherent to the inline DC EO pumping method, while (4-5) can be eliminated through engineering. These issues are addressed in Chap. 2.

If the pump is operated with alternating currents (AC) issues (1-2) can be overcome. The EO pump will then be a hybrid between a displacement and a dynamic pump. The actuation principle is based on EO, and hence dynamic, but the pumping principle is similar to a reciprocating diaphragm pump with valves. An AC EO pump has the advantage of a strong actuator but suffers from the same problems as a reciprocating pump. This is the topic of Chap. 5, 6 and 7.

High-frequency AC combined with asymmetric electrode arrays can be used to generate induced-charge EO pumping (IC EO). In this configuration the EO pump is a dynamic pump with no moving parts. The IC EO pumping method is relatively weak and inefficient compared to traditional EO pumping but suffers only from issues (1) and (3). Two different IC EO pump realizations are described in Chap. 8.

1.4 Outline of the thesis

- **Chap. 2: DC electroosmotic pump**

During the three year PhD project approximately half the time was devoted to the DC EO pump project. In the initial pump designs the pump performance degraded

over time. Various configurations of ion exchange membranes and frits were tested. A major breakthrough in terms of stability was the understanding of limiting current. Although the phenomenon is well-understood in the field of membrane research it had not been applied to microfluidics. Most of this work was published in the paper *Long-term stable electroosmotic pump with ion exchange membranes*, [10]. The chapter is therefore based on this paper.

- **Chap. 3: Additional material for the DC EO pump**

As previously mentioned a lot of effort went into the DC EO pump design. In this chapter some of the material that was omitted in Chap. 2 is presented. The chapter begins with more information about different types of frits and ion exchange membranes. Then follows a theory section about limiting current and experiments to support the theory. The many hours spent on fabrication of the pumps resulted in knowhow about fittings and sealing which is also presented. The ion transport in the pump is very important since it is directly correlated to the pumping effect. It is very difficult to measure the pH and the concentration of the different ion species within the pump during operation. Hence only a hypothesis for the ion transport exists. However, measurements of the electrical and chemical properties of the buffer are presented. Finally, the difference between operating the pump with a constant voltage compared to a constant current is considered from a theoretical point of view. This work was also published in the paper *Nanofluidic components for electrokinetic micropumps*, [11].

- **Chap. 4: Microvalves overview**

In this chapter five different types of microvalves are presented. The reason is that the following chapters with AC EO pumps all feature microvalves. The development of microvalves has indeed been a large part of the PhD project. The concept of dead and swept volume is presented along with other parameters that are important in relation to microvalves.

- **Chap. 5: AC EO pump with membrane valves**

The AC EO pump was developed in order to remove some of the problematic issues with DC EO pumping. Firstly, an AC pump can use bubble-free electrodes which reduce problems with electrolytic gases. Secondly, it is possible to construct a system that separates the EO actuator liquid from the pumped liquid. In this way the pump may be independent of the pumped liquid which is a great advantage. However, the AC operation comes at the cost of extra complexity in the form of a valve and a separator system. The membrane valves were specifically developed for this pump. Most of this work is presented in the paper *AC electroosmotic pump with bubble-free palladium electrodes and rectifying polymer membrane valves*, [12]. The chapter is therefore based on this paper. The work was carried out in the final part of the PhD project.

- **Chap. 6: Additional material for the AC EO pump**

In this chapter the testing and modelling of the bubble-free palladium electrodes are

described in details. The chapter also holds some information about polymer device fabrication and hydraulic resistance measurement techniques.

- **Chap. 7: AC EO pump with mobile plug valves**

The pumping scheme is very similar to what is described in Chap. 5, however, the valve system is completely different. Hence, this chapter is mostly concerned with the design and fabrication of the mobile plug valves. The work was done at the University of Michigan in collaboration with Assist. Prof. E.F. Hasselbrink and PhD student M.P. Chang.

- **Chap. 8: Additional pump projects**

In this chapter three pump related projects are summarized. The first project is a design idea for an EO pump capable of pumping all types of liquids. The idea resulted in the paper *A novel electroosmotic pump design for nonconducting liquids: theoretical analysis of flow rate-pressure characteristics and stability*, [13]. The second project is a theoretical analysis of an existing EO pump. The analysis was published as *Theoretical analysis of the low-voltage cascade electroosmotic pump*, [14]. The third and ongoing project involves the initial steps in the development of an induced-charge EO pump.

1.5 Publications during the project

Papers in peer reviewed journals

1. *Theoretical analysis of the low-voltage cascade electroosmotic pump*
A. Brask, G. Goranović, and H. Bruus
Sens. Actuators B, (2003), **92**, 127-132.
2. *Nanofluidic components for electrokinetic micropumps*
A. Brask, Jörg P. Kutter and H. Bruus
J. Adv. Nat. Sci., (2004), **5**, 423-430.
3. *A novel electroosmotic pump design for nonconducting liquids: theoretical analysis of flow rate-pressure characteristics and stability*
A. Brask, G. Goranović, M. J. Jensen and H. Bruus
J. Micromech. Microeng., (2005), **15**, 883-891.
4. *Long-term stable electroosmotic pump with ion exchange membranes*
A. Brask, Jörg P. Kutter and H. Bruus
Lab. Chip., (2005), **5**, 730-738.
5. *AC electroosmotic pump with bubble-free palladium electrodes and rectifying polymer membrane valves*
A. Brask, D. Snakenborg, Jörg P. Kutter and H. Bruus
Lab. Chip., (2006), **6**, 280-288.

Conference proceedings with peer review

1. *The low-voltage cascade EOF pump: comparing theory with published data*, Anders Brask, Goran Goranović and Henrik Bruus, Proc. μ TAS 2002, Nara, Japan, November 2002, vol. **1**, p. 79-81.
2. *Electroosmotically driven two-liquid viscous pump for nonconducting liquids* Anders Brask, Goran Goranović and Henrik Bruus, Proc. μ TAS 2002, Nara, Japan, November 2002, vol. **1**, p. 45-47.
3. *Electroosmotic pumping of nonconducting liquids by viscous drag from a secondary conducting liquid*, Anders Brask, Goran Goranović and Henrik Bruus, Proc. NanoTech 2003, San Francisco (CA) USA, March 2003, vol. **1**, p. 190-193.
4. *Long-term stability for frit-based EO pumps under varying load conditions using ion exchange membranes with controlled diffusion layer widths*, Anders Brask, Henrik Bruus and Jörg P. Kutter, Proc. μ TAS 2004, Malmö, Sweden, September 2004, vol. **2**, p. 136-138.

Co-supervision

1. *Asymmetric electrode micropumps*
Morten Arnoldus and Michael Hansen
BSc. thesis, MIC, DTU, 2004.
2. *Electrokinetic micropumps*
Misha M. Gregersen
MSc. thesis, MIC, DTU, 2005.

Chapter 2

DC electroosmotic pump

2.1 Introduction

The PhD project started with the development of a DC EO pump. The first designs were inspired by Yao *et al.* and Morf *et al.*, [15, 16, 17]. The initial versions of the DC EO pump only worked for a couple of minutes before the performance dropped dramatically. A literature study confirmed that the temporal behaviour of EO pumping was rarely described. It is my belief that the temporal stability is, in fact, one of the main concerns for the application of DC EO pumps. The following paper, [10] presented in Sec. 2.2 describes the final version of the DC EO pump. Additional material follows in Chap. 3.

2.2 A. Brask *et al.*, Lab Chip, 2005, 5, 730-738

beginning of paper

Long-term stable electroosmotic pump with ion exchange membranes

Anders Brask, Jörg P. Kutter, and Henrik Bruus

MIC - Department of Micro and Nanotechnology, DTU Bldg. 345 east, Technical University of Denmark, DK-2800 Kgs. Lyngby, Denmark

We present the design, fabrication and test of a novel inline frit-based electroosmotic (EO) pump with ion exchange membranes. The pump is more stable than previous types due to a new flow component that ensures a controlled width of the diffusion layer close to the ion exchange membranes. The pump casing is constructed in polymers while the EO active part, the frit, is made in a nanoporous silica. The pressure capability of the pump is $\Delta p_m/\Delta V = 0.15$ bar/V. The flow rate to current ratio is $Q_m/I = 6$ $\mu\text{L}/(\text{min mA})$. This translates to $\Delta p_m = 4.5$ bar and $Q_m = 6$ $\mu\text{L}/\text{min}$ at $\Delta V = 30$ V. The pump has been tested with four different buffer concentrations. In order to investigate day-to-day reproducibility each Q - p pump characteristic has been recorded several times during hour-long operation runs under realistic operating conditions.

2.2.1 Introduction

Electroosmotic (EO) pumps are suitable for microfluidic applications because they can be made very compact and deliver high pressures. Moreover, they can produce a pulse-free flow without containing any moving parts. In EO pumps an electrolyte is pumped by applying an electric field to the charged Debye layer. The Debye layer is formed by the ions in the electrolyte due to electric screening of the immobile charges on the walls of the pump [5]. Traditionally, EO pumps are driven by voltages in the kilovolt range [18, 16, 19], but in many applications high voltages are impractical. As a consequence a low-voltage EO pump was presented by Takamura *et al.* [20] and analyzed by Brask *et al.* [14]. This low-voltage pump design allows for arbitrary pressure accumulation without increasing the voltage. However, EO pumps based on porous structures have proved to produce very high pressures with simpler geometries [21, 9, 22, 23]. A high flow rate variant of the porous EO pump is the so-called frit-based EO pump [24, 25]. For a recent review of micropumps see Ref. [3].

Some of the inherent problems for continuously operated DC EO pumps are the development of electrolytic gases and long-term stability. The gas development issue is traditionally avoided by separating the electrodes from the electroosmotic pumping with an ion exchange system [16, 18, 9, 20] or by using induced hydraulic pumping [26]. A system that recombines the electrolytic gases has been reported by Yao *et al.* [25].

The work presented here differs from most previous work on EO pumps by emphasizing stability. In particular, we investigate and address some of the stability issues for EO pumps with ion exchange membranes. We focus on two main stability criteria: (1) Temporal analysis of the flow rate and pressure under varying operating conditions. (2) The day-to-day reproducibility, i.e., the importance of proper priming and conditioning.

The paper is organized in the following way. In Sec. 2.2.2 the basic equations and concepts for electroosmotic pumping are presented. In Sec. 2.2.3 we present the final EO pump design as a result of a long development history. The functionality and design of the individual components are described in detail. Especially the concept of limiting current density is introduced in relation to EO pumps with ion exchange membranes. In Sec. 2.2.4 the fabrication of the pump is described. In Sec. 2.2.5 we deal with the fluidic setup and the measurement protocol. Finally the results and conclusions are presented in Sec. 2.2.6 and Sec. 2.2.7, respectively.

2.2.2 A model of EO flow in a frit

Our aim is to develop a long-term stable EO pump with high flow rate and pressure capacity. At the same time we want to use a low driving voltage. The solution is to use a structure with a large number of nanochannels. A nanoporous frit fulfills these requirements, see Fig. 2.1.

To a first approximation the geometry of the porous frit may be modelled as a large number of parallel coupled capillaries with length L and radius a . The cross sectional area and thickness of the frit is denoted A and L respectively. The porosity is defined as $\psi = \mathcal{V}_e/\mathcal{V}$ where \mathcal{V}_e is the void volume of the frit, i.e., the volume available to an electrolyte solution

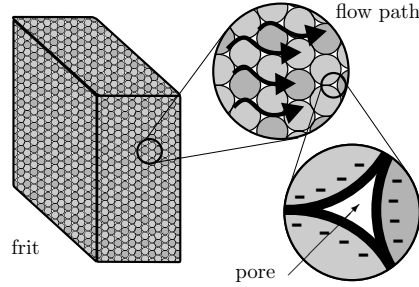


Figure 2.1: A rough sketch of a frit. The frit is made of a porous material, in this case silica. When silica comes in contact with an electrolyte it typically forms a negative surface charge. This effect makes the silica frit ideal for electroosmotic pumping.

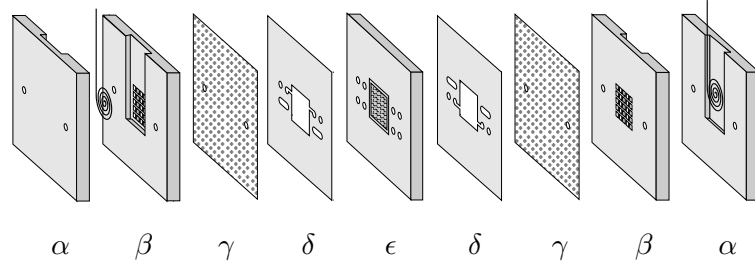


Figure 2.2: Schematic view of the functional components in the EO pump: Electrode chamber (α), electrode chamber and membrane support (β), ion exchange membrane (γ), spacer and bypass system (δ), and frit holder and through-holes for the bypass system (ϵ).

and $\mathcal{V} = A L$ is the total volume.

The surface charge generates a potential distribution within the capillaries. In a cylindrical capillary this can be solved analytically for a symmetric electrolyte by invoking the Debye-Hückle approximation in the Poisson-Boltzmann equation [7]. The governing equations for the theoretical Q - p performance of a frit-based EO pump are as follows:

$$Q_m = \alpha_{eo} \psi \frac{A}{L} \left[1 - \frac{2\lambda_D I_1(a/\lambda_D)}{a I_0(a/\lambda_D)} \right] \Delta V, \quad (2.1)$$

$$\Delta p_m = \alpha_{eo} \frac{8\mu}{a^2} \left[1 - \frac{2\lambda_D I_1(a/\lambda_D)}{a I_0(a/\lambda_D)} \right] \Delta V, \quad (2.2)$$

$$\lambda_D = \left(\frac{\epsilon k T}{e^2 \sum_i c_i z_i^2} \right)^{1/2}, \quad (2.3)$$

$$Q = Q_m \left(1 - \frac{\Delta p}{\Delta p_m} \right). \quad (2.4)$$

Here, α_{eo} is the electroosmotic mobility, μ the dynamic viscosity, ϵ the dielectric constant of the electrolyte, ΔV the applied voltage, c_i and z_i the concentration and valence of the i -th species, respectively. λ_D is the Debye length, Q_m the maximum flow rate, and Δp_m

the maximum backpressure. I_k is the k 'th-order modified Bessel function of the first kind. For more details see Ref. [21].

The term in the brackets in Eqs. (2.1) and (2.2) is denoted the correction factor. In the case of $a/\lambda_D \gg 1$ the correction factor equals unity. If the channel radius a and the Debye length λ_D become comparable, the flow Q_m is reduced due to an effect termed Debye layer overlap, e.g., for $a/\lambda_D = 1$ the correction factor is 0.11. Starting from large values of a/λ_D the electroosmotic pressure increases with decreasing a/λ_D until $a/\lambda_D \approx 1$ hereafter it does not change considerably.

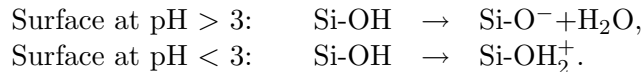
A nanoporous silica frit is chosen as the pumping media because it gives a high flow rate, $Q_m \propto A$, and a high backpressure capacity $p_m \propto a^{-2}$, see Eqs. (2.1) and (2.2). Furthermore, it is also commercially available and easy to integrate.

2.2.3 The design

The frit-based EO pump consists of an assembly of nine layers as shown in Fig. 2.2. The electrode compartments formed by α and β are separated from the frit compartment ϵ by anion exchange membranes (AEM) γ , which allow only anions (negative ions) to pass, while bulk fluid and positive ions are retained. The pressure buildup generated by the frit is therefore confined to the inner loop of the pump, δ - ϵ - δ , which enables free ventilation of electrolytic gases developed in electrode compartments.

The frit

Electroosmosis is based on separation of charges where one polarity is mobile in the electrolyte and the other is immobile on the wall. The surface charge density and pore size are very important in relation to the performance. The frit considered here is based on silica (SiO_2), a material that will typically form a negative surface charge. The EO flow direction is hence from the anode to the cathode. The surface charge and hence the EO mobility is highly dependent on pH [18],



A constant pH level is required for stable operation. In fact, this is a problem in many previously reported EO pumps [9, 15]. A more detailed discussion on how to maintain a stable pH follows in the next sections.

Ion exchange membranes

The pumping stability is governed by the pH and flow conditions in the inner loop, δ - ϵ - δ in Fig. 2.2. Consider the onset of a current between the two electrodes in a pH neutral electrolyte. At the anode the pH will tend to drop because of the generation of hydronium ions (solvated H^+). The hydronium ions will migrate towards the cathode. A low pH environment will effectively remove the surface charge in the frit and thus stop the EO flow. To stabilize the pH level we insert an anion exchange membrane capable of preventing

the hydronium ions from entering the inner loop. In this way the pump will continue to work after the buffer in the reservoir has been depleted. The anion exchange membrane only allows negative ions to pass because of the Donnan exclusion principle [27].

The electrolyte used in these experiments is a disodium tetraborate buffer with pH=9.2. Since most of the hydronium ions will be blocked by the AEM the electric current in the stationary state will be transported mainly by hydroxyl OH⁻ and sodium Na⁺ ions.

The second main function of the ion exchange membranes is that they block bulk flow. The ion exchange membranes are made of a nanoporous polymer with a permanently charged surface. The pores are so small that they act exclusively as ion channels. We estimate the pressure driven flow through the membranes due to reverse osmosis to be less than 1 % of the overall flow rate. As a consequence, both reservoirs can be kept at atmospheric pressure allowing for free ventilation of electrolytic gases. Over a period of two hours this system works well but eventually the reservoirs would need to be refilled due to evaporation and electrolytic gas generation.

Spacer

Let us consider an ion exchange membrane immersed in an electrolyte solution. The ionic concentration within an ion exchange membrane is usually a factor 10¹ to 10³ higher than in the ambient liquid. The membrane phase therefore conducts electric current much better than the liquid phase, see Fig. 2.3. Hence, after a while the liquid in the vicinity of the cathode side of the membrane will be depleted of ions. Diffusion of ions from the bulk will contribute to the transport and try to equalize the ion concentration. If, however, the current density exceeds a certain threshold the slow diffusion current cannot bring in new ions fast enough. The consequence is that the ion concentration at the membrane surface is zero. This threshold is called the limiting current density i_{lim} . An expression for the limiting current density i_{lim} can be derived from an assumption that there exists a diffusion boundary layer of thickness ℓ :

$$i_{\text{lim}} = z_- \left(1 + \frac{z_-}{z_+} \right) F D_- \frac{c^l}{\ell}. \quad (2.5)$$

Here, z_- and z_+ are the charge coefficients of the anion and cation species, respectively, D_- is the diffusion coefficient of the anions, F is the Faraday constant, and c^l is the concentration of the anions in the liquid phase.

If the current density i is increased beyond i_{lim} , dissociation of water will happen on the surface of the membrane facing the frit. Experimentally this can be observed by a plateau in the current-voltage characteristic [27]. The dissociation of water will increase the hydronium ion concentration in the frit and lower the pH, which in turn affects the stability negatively. Therefore, in order to increase the limiting current the diffusion length ℓ must be decreased. This can be realized by having a very thin spacer between the membrane and the frit. This spacer of width 90 μm is denoted δ in Fig. 2.2. The spacer layer is designed such that the flow entering the frit has to pass over the membrane at the same time. The induced convection adds to the transport of ions and hence increases the limiting current i_{lim} .

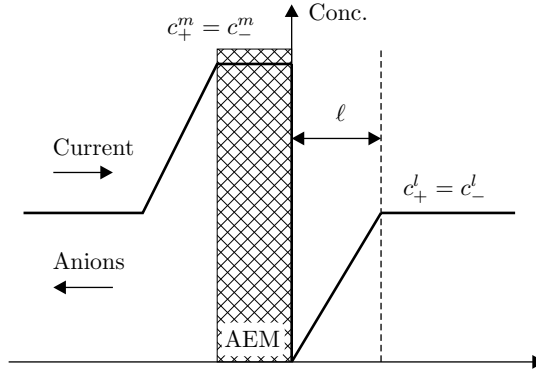


Figure 2.3: Schematic figure of the concentration of ions in the vicinity of the anion exchange membrane (AEM). The membrane phase has a much higher concentration of ions $c_{\pm}^m \approx 1$ M compared to the bulk solution $c_{\pm}^l \approx 10$ mM. Only the anions are mobile in membrane phase. In the presence of a current this imbalance in concentration and hence conductivity will lower the ionic concentration on the cathode side of the AEM. Convection in the bulk ensures a constant concentration at a distance ℓ from the membrane. In the depicted situation the current equals the limiting current density $i = i_{\text{lim}}$.

The boundary diffusion layer is associated with a large electrical resistance because of the low ionic concentrations. The consequence is that the electric current I is slightly dependent on the flow condition $Q(\Delta p)$ at a fixed voltage ΔV . A more in-depth computational study of this diffusion-convection problem is, however, beyond the scope of this work.

Membrane support

The anion exchange membrane is relatively thin, about $140 \mu\text{m}$, and must therefore be mechanically supported. The support structure β consists of a 5 by 5 matrix of 1 mm deep through-holes. The array of holes allows the electrolyte in the reservoir to be in contact with the membrane without allowing the membrane to deflect considerably. Keeping the compliance of the pump to a minimum in this way is important in relation to the response time of the pump. A typical response time is 1 minute measured from the change in backpressure Δp to the time where the flow rate Q is stabilized again. Together with the back plates α the membrane supports form the reservoirs. Each reservoir contains $V_{\text{res}} = 75 \mu\text{L}$ of buffer. Bubbles are expected in the reservoirs due to electrolysis, and they can accumulate in the through-holes of the membrane support mesh. If this happens the current and hence the pumping will decrease. An additional hydrophilic fiber mesh was therefore inserted between the electrode and the membrane support mesh in order to prevent this from happening.

2.2.4 Fabrication

All layers have been fabricated from a polymer substrate by laser ablation [28, 29], with a 65 W CO_2 laser from Synrad Inc. (Mukilteo, WA, USA). The α , β and ϵ layers are made

in 1.5-2 mm thick polymethylmethacrylate from Nordisk Plast (Auning, Denmark). The material is chosen because of its ideal properties for laser ablation. The gaskets and spacer layers δ were made in 90 μm thick thermoplastic elastomer from Kraiburg Gummiwerke (Waldkraiburg, Germany).

The layers α and β are bonded together thermally. The rest of the layers are pressed against each other by nuts and bolts; note that the holes for the bolts are not shown in Fig. 2.2. This construction allows for rapid interchange of components. The alignment is accurate within 300 μm . External tubing was mounted in layers α and β by making two threaded holes. The tubing was then screwed in and fixed with a small amount of epoxy. This fixture was proven to be tight at pressures in excess of 7 bar.

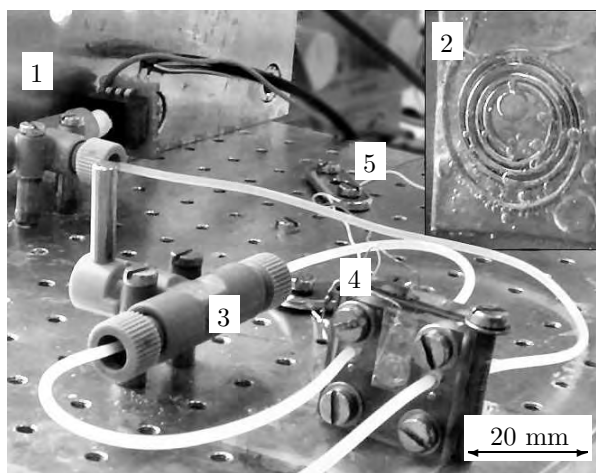


Figure 2.4: Picture of the EO pump and the part of the fluidic test setup illustrated in Fig. 2.5 within the dashed box. (1) Pressure sensor embedded in a tee junction. (2) An inset showing a magnified view of the electrode chamber of the EO pump. A hydrophilic fiber mesh (not visible) has been inserted between the spiral shaped Pt electrode and the membrane support mesh in order to prevent the visible bubbles from blocking the current. (3) External bypass valve. (4) The assembled EO pump measures $20 \times 20 \times 10 \text{ mm}^3$. (5) The power leads for the pump.

In the experiments described here a pure silica frit from Advanced Glass and Ceramics (Holden, MA, USA) with a nominal pore size of 200 nm and dimensions $5 \times 5 \times 2 \text{ mm}^3$ was used. The frit was bonded to a holder ϵ by use of epoxy.

The ion exchange membrane was purchased from Fuma-Tech (Vaihingen an der Enz, Germany). The membrane is quite thin, about 140 μm which reduces problems with swelling. This particular membrane must be hydrated at all times. If the membrane is dehydrated it may form tiny stress cracks causing leaks. Dehydration is prevented by sealing the reservoirs when the pump is inactive.

All the experiments have been performed with borate buffer only. The concentration of the borate buffer is measured in terms of the molar concentration of $\text{Na}_2\text{B}_4\text{O}_7$. The buffer has a $\text{pH} = 9.2$.

2.2.5 Measurements

The focus of the experimental work is the long-term performance of the pump under realistic working conditions. The setup could be operated without simultaneously having to manipulate the pump or the fittings. This is a clear advantage when investigating reproducibility.

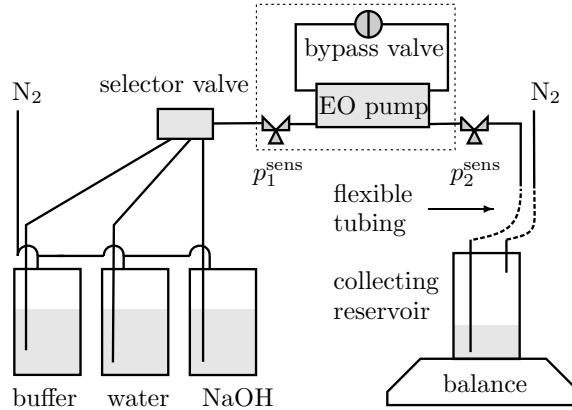


Figure 2.5: Schematic diagram of the experimental setup. A selector valve is used for selecting the solution that goes into the EO pump. Pressurized N_2 is used for driving the solutions when priming the pump. During measurements this external pressure is used for setting the backpressure on the pump. Flexible tubing is used for connecting the balance reservoir in order to minimize the forces from the tubing. Vacuum could be applied to the collecting reservoir in order to empty it without disturbing the flexible tubing. The components within the dashed box are depicted in Fig. 2.4.

Fluidic setup

Valves and fittings (Upchurch Scientific, Oak Harbor, WA, USA) were mounted on a custom made table with 1/2" spaced threaded holes, see Fig. 2.4. Flow rates Q were measured by collecting liquid in a 25 mL reservoir placed on a balance with 0.1 mg precision (Sartorius CP224S, Goettingen, Germany). The change in mass of the reservoir could then be translated into a flow rate by dividing with the density of the liquid. The reservoir pressure (backpressure) was controlled by a N_2 source. The backpressure $\Delta p = p_2^{\text{sens}} - p_1^{\text{sens}}$ was measured by two 0-10 bar Honeywell pressure sensors (40PC150G1A, Freeport, IL, USA) placed upstream and downstream of the pump, see Fig. 2.5. Suspended flexible tubing was used to connect the collecting reservoir in order to minimize the transfer of forces from the tubing to the balance. After placing the reservoir on the balance it would take 30 minutes before the flexible tubing and hence the balance had settled. The preferred tubing material is polyvinylchloride because of its water impermeability. Silicone tubing is not suitable because the water content of the buffer can evaporate and leave large crystals that can block the tubing. In the remainder of the fluidic setup teflon tubing with an inner diameter of 0.5 mm was used giving negligible pressure losses while maintaining a small system volume.

During the measurements six variables were sampled at 1 Hz into a data file using LABVIEW with a 16-bit data acquisition card (National instruments, Austin, TX, USA). The variables are voltage ΔV , current I , upstream pressure p_1^{sens} , downstream pressure p_2^{sens} , mass of reservoir m , and elapsed time t . Before and after the experiments the pH levels in the reservoirs were measured by four color pH indicators.

Priming of the pump

In order to test the pump in a reproducible manner the pump and external tubing must be free of air bubbles. Bubbles can be removed by flushing the system. In Fig. 2.6 a flow diagram of the flushing system is shown.

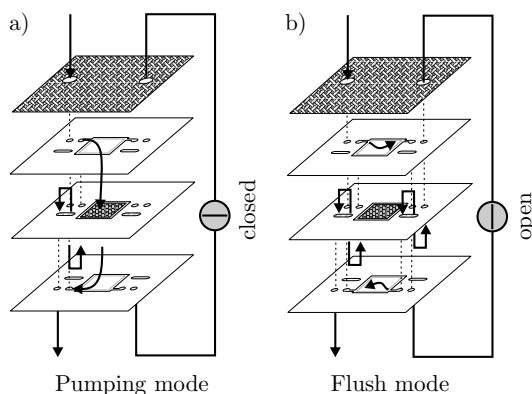


Figure 2.6: Flow diagram of the two modes of the flush system. (a) Pumping mode: the external bypass valve is closed. Hence the electrolyte can only pass through the frit. (b) Flushing mode: the external bypass valve is open. In this mode the flow can bypass the frit allowing for fast interchange of fluid within the pump. Note that the flow is directed through the frit holder ϵ and back. This flow routing eliminates problems with leakage from the inner loop δ - ϵ - δ to the electrode reservoirs α - β .

A flushing system is required because of the very large hydraulic resistance of the frit, about $200 \text{ bar}/(\mu\text{L}/\text{s})$. In the flushing mode the flow can bypass the frit which reduces the hydraulic resistance by a factor 10^3 . In the flushing mode it is hence possible to prime the pump and remove bubbles from the system. Once all bubbles have been removed the conditioning of the frit may begin. The purpose of the conditioning is to ensure that the surface charge, i.e., the EO mobility, is the same within a series of experiments. The conditioning is performed by flushing three different liquids through the frit. First a strong alkaline solution 0.1 M NaOH is used to regenerate the surface charge. Then deionized water is used to remove the alkaline solution and finally the frit is flushed with the buffer, $\text{Na}_2\text{B}_4\text{O}_7$.

The internal volume of the system is $70 \mu\text{L}$ from the selector valve to the EO pump, see Fig. 2.5. Hence, an intermediate flush of $400 \mu\text{L}$ or more is applied with the bypass valve open after a change in the selector valve's position. This is done to make sure that the electrolyte in the tubing has been replaced before the bypass valve is changed into pumping mode.

The maximum pressure that can be applied safely to the frit compartment is about 2 bar. At that pressure the flow rate is $Q = 2 \text{ bar} / (200 \text{ bar}/[\mu\text{L}/\text{s}]) = 10 \text{ nL}/\text{s}$. The volume of the frit is approximately $\mathcal{V}_e = \mathcal{V} \times \psi = 15 \mu\text{L}$, where $\mathcal{V} = 5 \times 5 \times 2 \text{ mm}^3$ and $\psi = 0.3$. It therefore takes roughly half an hour to flush one void volume \mathcal{V}_e of the frit. Optimally, one would like to flush the frit void volume several times. However, in order to save time the frit void volume is only flushed a little more than one time with each of the three solutions. Once the flushing volume exceeds the frit void volume no further dependence of flushing volumes was observed in the experiments. The exact flushing volumes from each experiment are listed in Table 2.1.

Measurement protocol

A protocol for the execution of the measurement was established in order to make each Q - p pump characteristic comparable. After priming, the pump would be operated for 1 hour with no backpressure, $\Delta p = 0$. Then the flow rate was measured at ten different backpressures, see Fig. 2.7. Each backpressure level was kept constant over a period of 6 min. During the first 3 min. the backpressure is set and the system allowed to adjust accordingly. The next 3 min. are used for the actual measurement. The time span of a measurement is indicated in Fig. 2.7 with vertical dashed (start) and solid (stop) lines. The thick solid horizontal lines indicate the calculated average in each measurement.

Conc. mM	No.	p_m/Q_m $\frac{\text{bar}}{\mu\text{L}/\text{s}}$	R_{hyd} $\frac{\text{bar}}{\mu\text{L}/\text{s}}$	p_m $\frac{\text{bar}}{\text{mA}}$	Q_m $\frac{\mu\text{L}}{\text{minmA}}$	pH A/C	preflush μL
1	11	59	138	4.9	4.9	3/11	47/85/62
1	12	74	139	6.6	5.3	3/11	42/63/92
1	13	92	134	7.9	5.1	-	25/34/85
1	14	53	135	5.3	5.9	-	32/32/33
5	1	108	192	9.6	5.3	-	18/18/22
5	2	123	195	11.6	5.7	6/12	21/22/47
5	3	102	186	10.2	6.0	-	22/36/24
20	7	67	157	7.2	6.5	3/13	28/20/29
20	8	68	152	5.9	5.3	2/13	34/52/40
20	9	78	151	8.3	6.4	2/13	17/27/41
20	10	75	144	8.0	6.4	5/13	36/54/90
100	4	46	-	1.9	2.5	-	48/-/193
100	5	53	-	1.7	1.9	5/13	44/-/46
100	6	61	153	1.8	1.8	-	33/-/46

Table 2.1: An overview of the Q - p characteristics. The data is divided by concentration into four series with $c = 1, 5, 20, 100$ mM. The number (No.) is used for reference in this paper. The hydraulic resistance of the frit was measured during the priming, see Sec. 2.2.5. p_m and Q_m is the maximum backpressure and flow rate, respectively. The pH values in the (A)node and (C)athode chamber are measured after approximately 2 hours of pumping. The preflush sequence is 1 M NaOH/deionized water/buffer. The applied voltage is $\Delta V = 30 \text{ V}$ in all of the experiments.

The backpressure is set by increasing or decreasing the amount of compressed air in the collecting reservoir. Once the desired pressure level has been reached the air valve is closed. In some of the initial measurements the backpressure was not entirely constant due to air leaks in the collecting reservoir. This constitutes a source of error in the flow rate measurements because the loss of air pressure is associated with the mass of the reservoir. To correct for this error the mass of the compressed air is included in the flow rate calculations. This is also why the calculated average sometimes is slightly above the flow rate markings.

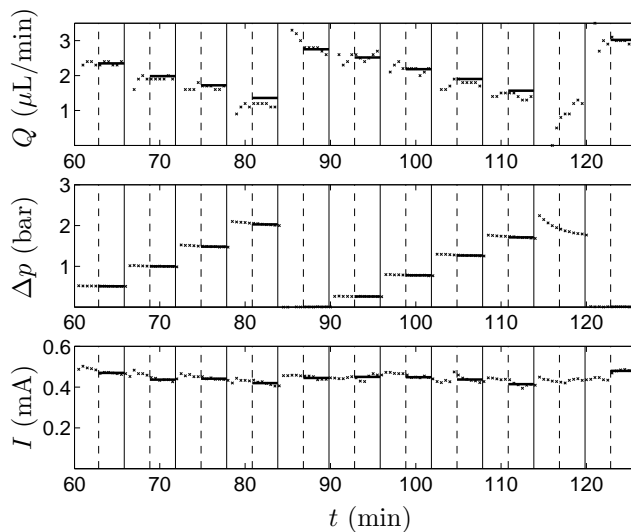


Figure 2.7: Flow rate Q , backpressure Δp and current I as function of time for experiment No. 3 in Table 2.1. The backpressure is increased in four steps. Then the pressure is released to check that the pump recovers its baseline. This procedure is then repeated, now with five steps in Δp . In each measurement there is a black horizontal line indicating the value transferred to the Q - p diagram. If a measurement for some reason is invalid there is no line. Flow rate measurements are based on a sliding average of width 1 min.

The standard protocol was that the backpressure was gradually increased. Once the backpressure reached the maximum testing pressure of around 3 bar the pressure was released in order to check that the pump recovered its free flow rate Q_m . This procedure was then repeated one more time. In each measurement there is a black horizontal line indicating the value transferred to the Q - p diagram. If a measurement for some reason is invalid there is no line.

The minimum flow rate is of the order $Q = 1 \mu\text{L}/\text{min}$. This corresponds to collecting 1 mg/min of liquid which should be compared with the minimum measurable mass of 0.1 mg. A flow rate measurement should be based on collecting at least ten times the minimum measurable mass. In this case this requirement limits the temporal resolution of the flow rate measurements to 1 min.

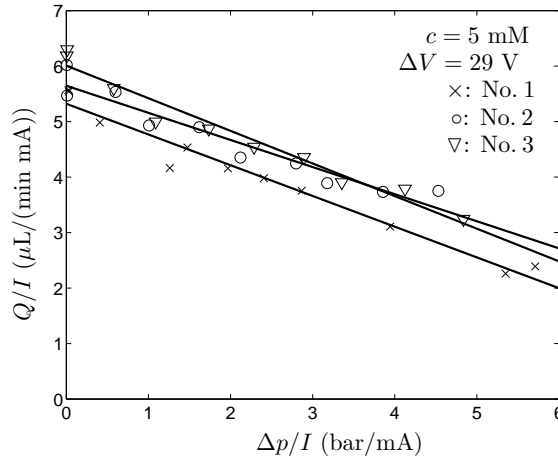


Figure 2.8: Experimental data of flow rate Q vs. backpressure Δp . The current in the experiments were approximately $I = 0.5$ mA, see Fig. 2.7. The performance was therefore $Q_m = 3$ $\mu\text{L}/\text{min}$ and an extrapolated $\Delta p_m = 5$ bar. Experimental parameters can be found in Table 2.1.

2.2.6 Results

Because it takes about six hours to make one Q - p characteristic each characteristic was made on separate days. The pump remained unchanged in all of the experiments. In Table 2.1 the complete list of experiments is shown. The experiments are labelled chronologically from 1 to 14. The bubbles in the reservoirs can induce some fluctuations in the current (electrical resistance) and hereby also in the flow rate Q . In the following this effect is accounted for by monitoring the flow rate and the pressure relative to the current instead of the voltage. Re-scaling the flow rate and backpressure with the current makes the data more reproducible and facilitates comparison with other EO pumps.

Pressure characteristics

In Fig. 2.8 three pump characteristics are shown. Each characteristic consists of about ten sets of corresponding flow rates and backpressures as described in Sec. 2.2.5. A linear fit is added to each Q - p characteristic to guide the eye. The three different realizations do collapse onto each other reasonably well. Experiment No. 1 falls slightly under No. 2 and No. 3 but has a similar slope. The average backpressure and flow rate are $\Delta p_m/I = 10.5$ bar/mA and $Q_m/I = 5.7$ $\mu\text{L}/(\text{min mA})$, respectively. The variations are less than 10% for the backpressures and 6% for the flow rates. The maximum available backpressure is an extrapolated value based on the Q - p measurements. The uncertainty on Δp_m is therefore larger than on Q_m .

The four series of Q - p characteristics with different buffer concentrations are shown in Fig. 2.9. The variation within the same series, i.e., same concentration, gives us information about the reproducibility. Overall, the $c = 5$ mM case appears to give the best results regarding Q_m/I , $\Delta p_m/I$ and reproducibility.

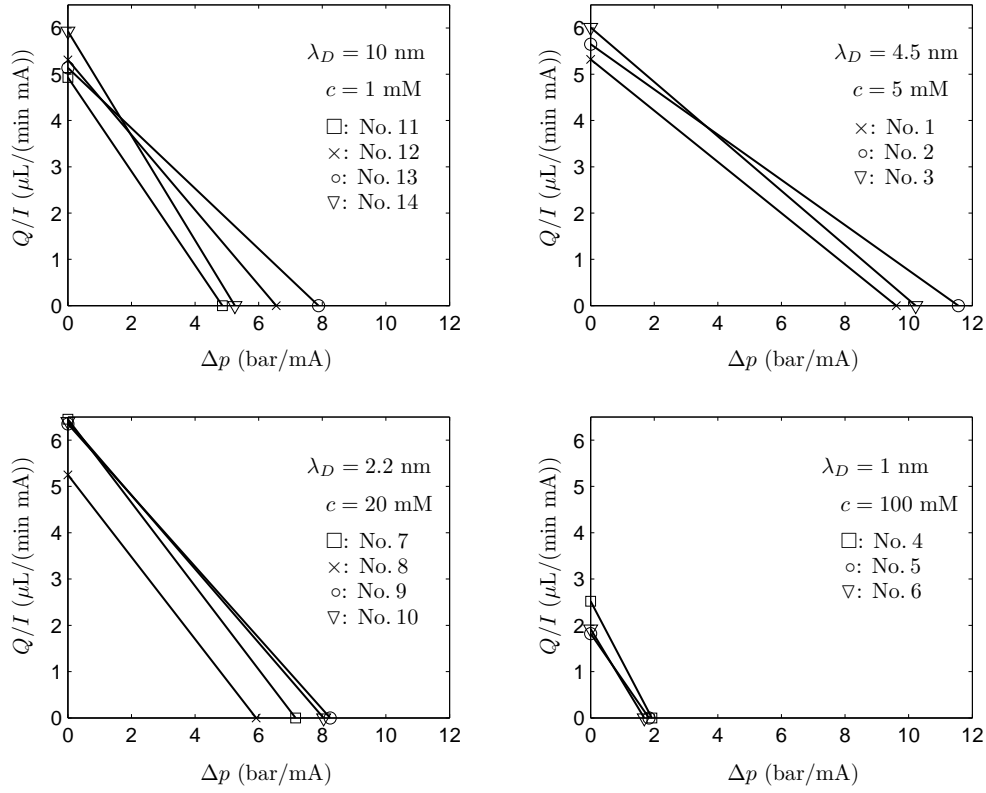


Figure 2.9: Q - p characteristics from all 14 experiments displayed for comparison. Note that the axis dimensions in the four figures are the same. The lines are extrapolated best fits from the experimental data.

Efficiency and diffusion layer

The efficiency η of a pump is defined as the hydraulic power $Q\Delta p$ divided by the electrical power consumption $I\Delta V$.

$$\eta = \frac{Q\Delta p}{I\Delta V}. \quad (2.6)$$

By inserting Eq. (2.4) in Eq. (2.6) and differentiating, it is found that the maximum hydraulic power is obtained with $\Delta p = 0.5 \Delta p_m$ and $Q = 0.5 Q_m$. The maximum efficiency is hence $\eta_m = 0.25 Q_m \Delta p_m / (I\Delta V)$.

In all experiments the current is initially very high and then decreases rapidly on a time scale of $t = 5 \text{ s}$, Fig. 2.10. The time scale is believed to be controlled by the diffusion layer width between the AEM and the frit. A simple estimate yields, $L = \sqrt{D t} = 105 \mu\text{m}$ which compares well with the thickness of the $90 \mu\text{m}$ spacer layer. An additional investigation showed that this time scale is independent on the type of frit used.

The large drop in the current indicates that the main potential drop lies across the diffusion layer adjacent to the ion exchange membranes. As a consequence the efficiency

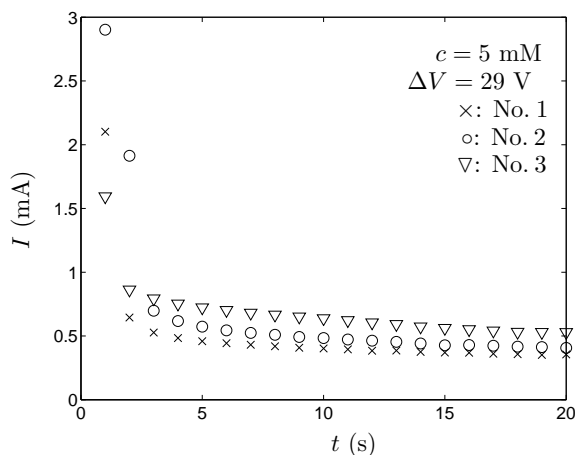


Figure 2.10: Experimental data of current I vs. time t . The pump is turned on at $t = 0$ s. The current decreases between 50-80% over the first 20 seconds of operation. Experimental parameters can be found in Table 2.1.

of the pump is low, $\eta = 0.04\%$ for $c = 5$ mM, compared to other reported EO pump efficiencies: 0.05-0.3% in Ref. [25], 1-3% in Ref. [9], and 5.6% in Ref. [22]. The conclusion is that the anion exchange membranes contribute to the stability but consume a considerable amount of energy. In this work stability was given a higher priority than efficiency. In our opinion stability issues have not been given proper attention in the literature. However, these issues are in fact very important from a practical point of view.

Flow rate and electric current

The flow rate Q_m is proportional to the electric current I in the free flow setup, see Fig. 2.11. This is not a surprising result, in fact the current is a much more direct handle on the flow rate than the voltage. Bubbles and polarization effects make it more difficult to monitor the effective voltage than the current. In applications it would therefore be recommended to regulate the pump by current instead of by voltage.

The electrical resistance of the diffusion layer is dependent on the flow rate Q because of the spacer layer, see Sec. 2.2.3. As a consequence the current I is also dependent on the flow rate $Q(\Delta p)$ for a fixed voltage ΔV , see Fig. 2.12. The membrane is not completely fixed between the membrane support and the spacer. The membrane can buckle due to swelling and the position can be shifted due to pressure changes. Changes in the position of the membrane can change the flow pattern over the membrane and hereby change the electrical resistance of the diffusion layer. It was observed that the I - Q curves for fixed voltage ΔV varied considerably, Fig. 2.12. A better control of the gap between the membrane and the frit is required in order to improve reproducibility.

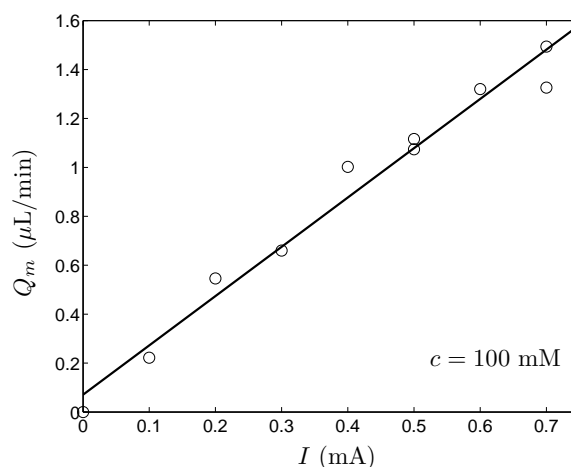


Figure 2.11: Experimental data of the free flow rate Q_m vs. current I . The current is held fixed at $I = 0.1, 0.2, 0.3, 0.4, 0.5, 0.6, 0.7$ mA, respectively by regulating the voltage. The flow rate is proportional with the current as expected. The slope $Q_m/I = 2.1 \mu\text{L}/(\text{min mA})$ is similar to what is observed in experiments No. 4-6.

Limiting current

The limiting current density may be calculated on basis of Eq. (2.5). Using the values $\ell = 90 \mu\text{m}$, $D = 2 \times 10^{-9} \text{m}^2/\text{s}$, $z_- = z_+ = 1$, $c_-^l = 2c$ we obtain $i_{\text{lim}} = 8.6, 43, 172, 858 \text{ A m}^{-2}$ for $c = 1, 5, 20, 100 \text{ mM}$, respectively. By multiplying the current density with the area of the membrane $A = 5 \times 5 \text{ mm}^2$ we obtain $I_{\text{lim}} = 0.21, 1.1, 4.3, 21 \text{ mA}$. Typical currents in the experiments were $I = 0.2, 0.5, 0.8, 2 \text{ mA}$ for $c = 1, 5, 20, 100 \text{ mM}$, respectively. Thus, in all cases the EO pump was operated below the limiting current density. If, however, the electrolyte within the pump is close to being stagnant the diffusion layer may extend into the frit and thereby lower the limiting current.

Buffer depletion

Due to electrode reactions the pH value in the anode and cathode reservoir will tend to decrease and increase, respectively. Initially, the buffer ensures a constant pH = 9.2, but after a while the finite reservoir volume \mathcal{V}_{res} and electrode reactions cause the buffer to deplete. A rough estimate on the depletion time t_{dep} is given as

$$t_{\text{dep}} = \frac{c\mathcal{V}_{\text{res}}F}{I}. \quad (2.7)$$

Here, F is the Faradaic constant, $\mathcal{V}_{\text{res}} = 75 \mu\text{L}$ the reservoir volume, $I = 0.5 \text{ mA}$ the electric current and $c = 5 \text{ mM}$ the buffer concentration. With these values the depletion time is $t_{\text{dep}} = 72 \text{ s}$. The pump is operated over a period of two hours. Hence, we conclude that the initial amount of ions in the reservoir is very small compared to the total molar charge exchange over time. The pH values in the electrode reservoirs are measured after

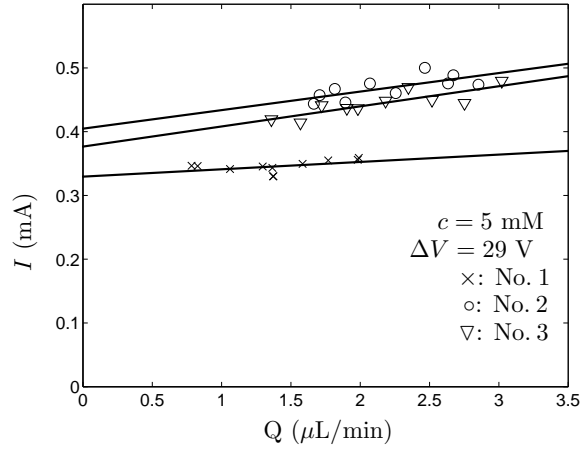


Figure 2.12: Experimental data of the current I vs. flow rate Q . The flow rate Q is exclusively regulated by the backpressure Δp . Experimental parameters can be found in Table 2.1.

the experiment, see Table 2.1. Typical values are $\text{pH} = 3$ and $\text{pH} = 13$ in the anode and cathode reservoir, respectively. The conclusion is that the pump works fine with a depleted buffer due to the anion exchange membranes. This stands in contrast to capillary based EO pumps that require large reservoirs and small currents in order to obtain a stable pH and a reasonable lifespan.

Estimated pore size

To be able to choose a proper buffer concentration, it is important to obtain a good estimate on the pore size of the frit. Three different measurement techniques were applied. Common for the techniques is that they only give an average pore size.

The first method is based on measuring the hydraulic resistance by collecting corresponding values of flow rate and pressure drop, and then use the parallel-capillary model of Sec. 2.2.2.

The second method is based on the values of Q_m and Δp_m obtained by operating the pump. If Eqs. (2.1) and (2.2) are rearranged we obtain

$$a = \sqrt{\frac{8 Q_m L \mu}{\Delta p_m \psi A}}. \quad (2.8)$$

The third method is to use a scanning electron microscope (SEM) to visualize the surface of the frit. The frit is covered by a 10 nm layer of gold. Unfortunately the pores are of comparable size which could be the reason why the image, see Fig. 2.13, is not perfectly resolved.

We would also like to remark that all of the measured pore sizes are very different than the one stated by the manufacturer. It was not possible to get information about how they had measured the pore size. The results from the three different methods are

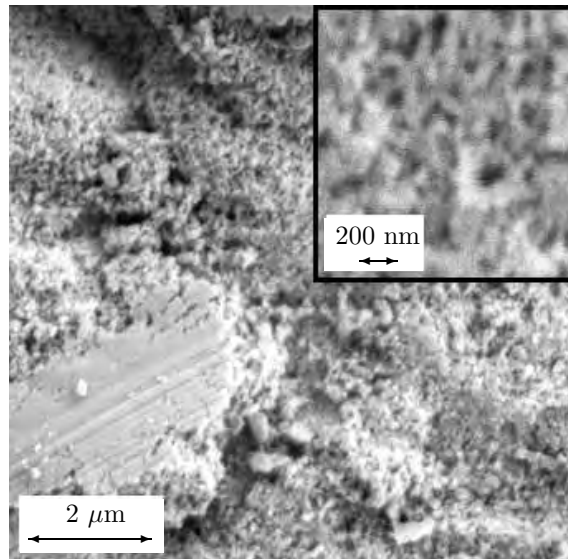


Figure 2.13: SEM picture of the silicate frit with 200 nm nominal pore size. The dark areas are the pores. Marks from tooling can be seen in the lower left corner. A magnification shows that the pores appear to be considerably smaller than the nominal pore size of 200 nm. A typical opening is estimated to be 40 nm.

method	diameter
hydraulic resistance	24 ± 2 nm
$\Delta p_m / Q_m$	34 ± 8 nm
SEM pictures	40 ± 20 nm

Table 2.2: Average diameter of the pores in the frit measured using different methods. The manufacturer states that the nominal pore size is 200 nm.

summarized in Table 2.2. The pore sizes are not as uniform as expected. The hydraulic resistance method probably underestimates the pore size due to the electroviscous effects. For a more detailed discussion see Ref. [30]. The most accurate method to estimate the pore size seems to be based on the $\Delta p_m / Q_m$ ratio.

A complication to the pore size discussion is that the hydraulic resistance R_{hyd} appears to be decreasing over time. If we look at Table 2.1 we see that R_{hyd} decreases by roughly 30% after 14 experiments. This could be due to structural damage to the frit caused by the treatment with sodium hydroxide before each experiment.

2.2.7 Conclusion

A stable stand-alone EO micropump has been developed and successfully tested. The design is highly versatile and can be modified to meet most flow requirements in microfluidic applications. Inherent disadvantages of continuously operated DC electroosmotic pumps

are the dependence on the electrolyte and development of electrolytic gases.

The pump has been tested with concentrations of borate buffer (pH = 9.2) in the range $c = 1\text{-}100$ mM. The optimal concentrations were 5 and 20 mM. The 20 mM buffer gave the highest flow rate and backpressure per volt, while the 5 mM buffer gave the highest efficiency $\eta = 0.04\%$.

The pump has been tested at realistic operating conditions over several weeks and the day-to-day reproducibility is within 6% on the flow rates Q_m for $c = 5$ mM. Even better reproducibility has been reported for capillary based EO pumps [18]. One of the reasons for this is that it is more difficult to condition the surface of a nanoporous frit. The pump performance does not degrade over the time of the measurement. So the variation in the flow rate Q_m must come from the flushing sequence that is supposed to condition the frit and membranes the same way each time. A more uniform ensemble of nanochannels would be advantageous as well.

The presented inline EO pump is simple and inexpensive in its construction and delivers a precise and stable flow. It is robust against particles and bubbles and is capable of delivering $Q_m = 6 \mu\text{L}/\text{min}$ and $\Delta p_m = 4.5$ bar at a low voltage $\Delta V = 30$ V. The buffer in the electrode chambers is depleted after a few minutes. However, the anion exchange membranes allow the EO pump to work even with a depleted buffer. In the scope of this work the tests have been limited to two hours. If the pump is operated for more than two hours the reservoirs need a refill because of evaporation and generation of electrolytic gases. A more enclosed reservoir design would extend the operation time but for true continuous DC operation the electrolytic gases must be recombined. A system capable of recombining the gases in order to avoid this problem has been reported in Ref. [25].

Typical applications are fluid propulsion on lab-on-a-chip systems. For compatible liquids the pump may be used for any application with appropriate flow rate and pressure requirements. For a working liquid that cannot be used as the pumping buffer, the pump may instead be applied as an actuator on the working liquid. The layered structure of the system allows for easy connection with other components. Further work on the pump involves integration with a valve and separator system making the pump independent of the working liquid.

We would like to acknowledge Torben Jacobsen for helpful discussions on electrochemistry and Maria Dimaki for help with the SEM images. This work is partly supported by the Danish Technical Research Council, μTAS Frame Program Grant No. 26-00-0220.

_____ end of paper _____

Chapter 3

Additional material for the DC EO pump

Many details and additional work were not included in the published paper on the DC EO pump. In the following this material is presented. Appendix B holds specific information about the experimental software and hardware used in the project.

3.1 The frit

The core of any frit-based EO pump is a block of porous material, denoted the frit. It is here that the pressure or momentum is generated in the pump. Two different frit materials have been tested, i.e., borosilicate and pure silica. These materials are suitable because their compatibility with electroosmosis is well documented. Furthermore, the materials are commercially available in rods, plates and discs with various pore sizes. Traditionally, the frits are used as filters in various applications. The data for the frits are shown in Table 3.1. The borosilicate frits were purchased from Robu Glassfilter, Hattert, Germany, whereas the pure silicate frits was purchased from Advanced Glass and Ceramics, Holden, MA, USA. A glass specialist, Euro-Glas, Karlslunde, Denmark, then shaped the frits to custom measurements and also fused (melted) the rim of the frits in order to prevent uncontrolled flow patterns.

material	pore size μm	diameter mm	thickness mm	porosity percent
borosilicate	10-16	10	3	26
borosilicate	1-1.6	5-10	1-3	26
silica 99.99%	0.20	5-10	1-2	31
silica 99%	0.004	5-10	3	-

Table 3.1: Properties of available frits. Borosilicate consists of 80.6% SiO_2 (silica), 12.6% B_2O_3 , 4.2% Na_2O_3 , 2.2% Al_2O_3 and traces of Fe_2O_3 , CaO , MgO and Cl .

3.1.1 Surface preparation

The electroosmotic mobility α_{eo} is very dependent on the surface charge. The surface of the frit is easily contaminated so a flush with a strong base such as 0.1 M NaOH can help resetting the surface charge. At one time a 6-fold increase in the EO flow was seen after such a flush. In capillary electrophoresis it is standard protocol to flush, 1× base, 2× DI water, 2× buffer, through the separation column to ensure reproducible EO flow. This flushing protocol was adopted for the DC EO pump experiments.

3.1.2 Pore size

The pore size of the frit can be difficult to estimate on basis of the manufacturers information. Usually pore sizes are used to determine the size of particles that are filtered by the frit. This is, however, another measure because particles tend to get stuck even when they are smaller than the channel. Commercially available nominal pore sizes range from $2a = 4 - 200$ nm in silica and from $2a = 1 \mu\text{m}$ and up in borosilicate.

A scanning electron microscope (SEM) can be used to visualize the pores. A thin layer of 40 Å gold is sputtered onto the surface to prevent charging during the scanning. The gold layer does not disturb the images of the frits with 200 nm and 1 μm nominal pore size, shown in Figs. 2.13 and 3.1, respectively. The 4 nm pores were, however, too small to be observed in the SEM.

The pore size may also be estimated by measuring the hydraulic resistance of the frit. However, in the nanoporous case streaming potential will have an influence on the flow. Viscous drag on the charged Debye layers will induce a potential balancing the drag force. The liquid in the Debye layers will consequently be stationary. The effect is that the hydraulic resistance will be larger than predicted by simple geometrical considerations and must therefore be compensated, see Ref. [31].

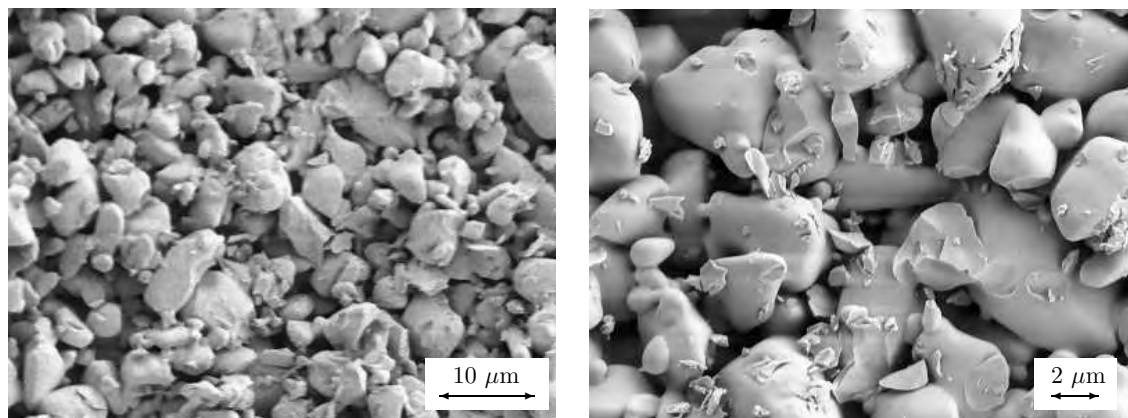


Figure 3.1: SEM pictures with different magnification of the borosilicate frit with 1-1.6 μm nominal pore size. The pore size appears to be in that range although the pore size seems very nonuniform. Courtesy of Maria Dimaki.

3.1.3 The frit mount

The frit is mounted in a polymer layer by use of epoxy, see Fig. 3.2(a). The rim of the frit is fused in order to prevent entrainment of epoxy by capillary forces during mounting. The DC EO pump version of the flow system in the inner loop can be seen in Fig. 3.2(b). In later versions the frit layer ϵ would consist of two layers in order to avoid the use of the gasket defined channels in the δ layers.

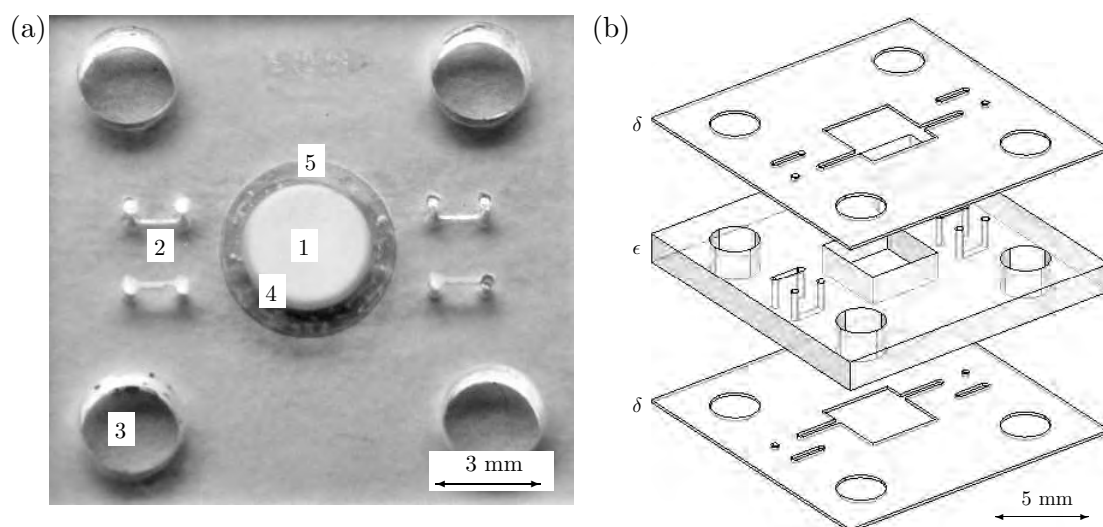


Figure 3.2: (a) Picture of the frit layer ϵ , ver. F4. (1) The frit, in this case a microporous frit from Robu. (2) Fluidic channels and through holes. (3) 3 mm dia. holes for the compression bolts. (4) Sealed rim on the frit. The glass rim is fused by a high temperature flame. (5) The frit is attached to the polymer substrate by epoxy. The epoxy is filled into a syringe and applied rapidly into the groove between the frit and the polymer substrate. (b) 3D visualization of the inner loop δ - ϵ - δ , refer also to Fig. 2.2.

3.2 Ion exchange membranes

In the DC EO pump the ion exchange membrane served two purposes: (1) To establish electrical contact between two reservoirs without allowing any considerable flow between them. (2) To ensure a stable EO flow through a high pH environment in the inner loop of the pump.

In general there are two different types of ion exchange membranes; cation exchange membranes (CEM) and anion exchange membranes (AEM). The CEM only allows cations, i.e. positive ions, to pass whereas the AEM only allows anions, i.e. negative ions, to pass. An ion exchange membrane suited for an electroosmotic pump should possess following three qualities: (1) Low electrical resistance, (2) high selectivity against H^+ and (3) high mechanical strength.

3.2.1 Selectivity and strength

A high selectivity against H^+ is important because the pH value is a critical factor in electroosmotic flow. In practice very mobile ions such as H^+ may leak through an AEM. Regarding the leakage of anion exchange membranes a lot of literature has been published, e.g., in the *Journal of Membrane Science*. In fact, the proton transport is not related to mass transport and Donnan exclusion cannot be fully applied. Proton diffusion according to the Grotthus mechanism, where protons are exchanged between water molecules, occurs in the hydration sphere of anion exchange groups. Hydrophobic anion exchange membranes with little water have a better selectivity. Furthermore, weak anion exchange groups of amines, imines etc. are protonated and the 'hopping' mechanism is observed. This is especially true for imidazole type anion exchange membranes, Ref. [32].

Mechanical strength is important since the membrane has to withstand the high pressures within the pump. A support structure is therefore needed. In the DC EO pump a polymer mesh was used whereas in the AC EO pump a large pore frit was used, see Fig. 6.4(a). The following types of ion exchange membranes have been tested, see Table 3.2.

manufacturer type	type	transport number	thickness μm	resistivity $\Omega \text{ cm}^2$	stability pH
Ameridia	AEM AMH	0.98	-	12	-
Fumatech	AEM FT-FAB	> 0.9	130-160	< 9	0-14
Fumatech	AEM FT-AM-T	0.95	475	< 2.5	2-8
Fumatech	AEM FAD	> 0.87	100	0.82	-
Fumatech	AEM DF 120 I	> 0.9	290	< 1.8	0-14
Fumatech	AEM FAB	> 0.99	30	0.44	0-14
DuPont	CEM Nafion	-	50	-	-

Table 3.2: Most of the membranes are anion exchange membranes (AEM). Only one is a cation exchange membrane (CEM). For Fumatech membranes the resistivities are measured in 0.5 M NaCl at 298 K. Selectivity/transport number is determined from the membrane potential in a concentration cell 0.1/0.5 M KCl at 298 K.

3.2.2 Handling of the membranes

Fumatech FAB's are specially designed to have an excellent permselectivity against H^+ . They are developed from a polymer showing good chemical and mechanical stability. This membrane is good choice due to its thin nature and wide pH range. The FT-FAB was used in the DC experiments while the FAB was used in the AC actuator. The latter membrane excels itself by having a very low electrical resistance.

Fumatech FT-AM-T and DF 120 are very mechanically stable with a minimum of wrinkling. The pH range should be applicable for most EO pumping purposes but the membrane thickness increases the electrical resistance and makes swelling a big problem.

The Fumatech FAD is thin but swells up to 30% in size when wet compared to dry making the integration impossible. The membranes are cut when they are dry.

The membranes are to be stored in a saline 3 – 5% solution or similar pH neutral solution. Dehydration should be avoided because the membranes may form crystals, change properties or start to leak. These phenomena have, however, not been observed with the Fumatech FT-FAB. One may also consider to add a biocide such as 100 ppm NaN_3 in order to prevent organic material from fouling the membranes.

3.2.3 Reverse osmosis

Reverse osmosis is pressure driven flow through ion exchange membranes. During the testing of the EO pump the ion exchange membranes were exposed to pressure differences on the order $\Delta p \approx 1$ bar. A typical reverse osmosis coefficient for an ion exchange membrane is $10^{-4} \text{ m}^3 \text{ h}^{-1} \text{ m}^{-2} \text{ bar}^{-1}$, [27], yielding a flow rate of $Q_{\text{mem}} \approx 0.04 \text{ } \mu\text{L} (\text{min bar})^{-1}$ for a 25 mm^2 membrane at 1 bar. This pressure driven membrane flow Q_{mem} is very small compared to the realized flow rates $Q = 1 - 10 \text{ } \mu\text{L min}^{-1}$.

3.3 Limiting current density

The concept of limiting current density is highly relevant for EO pumps with ion exchange membranes. The phenomenon is related to the use of ion exchange membranes in dilute solutions. The membrane phase has typically a much higher conductivity due to the high concentration of mobile counter ions. Hence the ions in the liquid phase cannot transport the same amount of current by electromigration alone. The region adjacent to the ion exchange membrane will therefore be depleted of ions until the concentration is so low that diffusion balances the transport. The current density where the ion concentration at the membrane surface is zero is denoted the limiting current density.

3.3.1 Limiting current theory

We wish to obtain an expression for the limiting current density. Consider a solution with two species consisting of positive (cations) and negative (anions) ions with valence z_+ and z_- respectively. An anion exchange membrane (AEM) is placed in the solution and an external potential is applied. The molar fluxes are j_- and j_+ for anions and cations respectively,

$$j_i = -D_i \frac{dc_i}{dx} - D_i \frac{z_i F}{RT} c_i \frac{d\phi}{dx}. \quad (3.1)$$

The transport of cations in steady-state must be zero because of the AEM,

$$j_+ = 0, \quad (3.2)$$

$$0 = -D_+ \frac{dc_+}{dx} - D_+ \frac{z_+ F}{RT} c_+ \frac{d\phi}{dx}, \quad (3.3)$$

$$\frac{d\phi}{dx} = -\frac{RT}{z_+ F} \frac{1}{c_+} \frac{dc_+}{dx}. \quad (3.4)$$

Equation (3.4) can be used in conjunction with the charge neutrality $z_+c_+ = -z_-c_-$ which also applies for the derivative,

$$j_- = -D_- \left(\frac{dc_-}{dx} - \frac{z_- F}{RT} c_- \frac{d\phi}{dx} \right) \quad (3.5)$$

$$j_- = -D_- \frac{dc_-}{dx} \left(1 - \frac{z_-}{z_+} \right) \quad (3.6)$$

The concentration gradient may be estimated using a simple boundary layer model,

$$\frac{dc_-}{dx} = \frac{c_-^l - c_-^m}{\ell}, \quad (3.7)$$

where c_-^l is the anion concentration far away from the membrane surface c_-^m . The thickness of the boundary layer is denoted ℓ . The current density, i is the sum of the molar fluxes times the charge per mol,

$$i = F \sum_k z_k j_k. \quad (3.8)$$

In the case of limiting current the concentration drops to zero near the surface of the AEM, $c_-^m = 0$. Since $j_+ = 0$, Eq. (3.8) combined with Eqs. (3.6) and (3.7) yield

$$i_{\text{lim}} = |z_-| \left(1 + \frac{|z_-|}{|z_+|} \right) F D_- \frac{c_-^l}{\ell}, \quad (3.9)$$

where z_- and z_+ are the charge coefficients of the anion and cation species, ℓ is the diffusion boundary layer thickness, D_- is the diffusion coefficient of the anions, F is the Faraday constant, and c_-^l is the concentration of the buffer.

If the current density i is increased beyond the limiting current density i_{lim} , dissociation of water will happen on the frit side of the membrane surface, see Fig. 2.3. The consequence is an increased concentration of hydronium ions close to the frit. Since this is not a desirable situation the limiting current must be increased. The only two controllable parameters in Eq. (3.9) are the concentration c_-^l and diffusion boundary layer thickness ℓ . Increasing the concentration will, however, not lower the i/i_{lim} ratio and hence not help. The remaining option is to reduce ℓ . This can be done by flushing the membrane surface as described in Sec. 2.2.3. Prior to the final DC EO pump design some experiments were devised in order to test if the effect of limiting current was observable. This is the topic of the next section.

3.3.2 Boundary layer experiments

In order to prove that the concept of limiting current density i_{lim} is involved in the EO pump we designed an experiment using cyclic voltammetry.

Two current-voltage curves were recorded. One with the pump at rest and one where the pump was subjected to vibrations. If the two curves differ this is a clear indication of mass transport, i.e., limiting current phenomena. A test cell was constructed, see Fig. 3.3.

The working electrodes are two platinum (Pt) electrodes because Pt is an inert metal and therefore does not react with the electrolyte. The two reference electrodes are made of wires of silver (Ag) covered with silver chloride (AgCl) on the surface.

The reference electrodes are used because we want to measure the potential in the solution. The redox system on the reference electrodes gives a well defined electrode potential. The reference electrodes should be placed close to the working electrodes but not so close that the current field is disturbed.

We assume that the concentrations in the reservoirs are the same so this will give no contribution to the single electrode potential according to the Nernst equation.

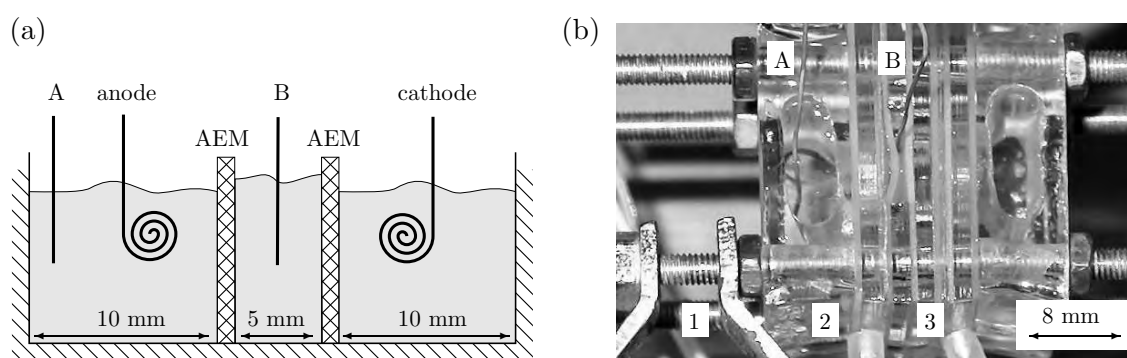


Figure 3.3: (a) Schematic of the experimental setup. The cross sectional area of the exposed membrane is $A = \frac{\pi}{4} D^2 = 0.79 \text{ cm}^2$. In the experiment a $c_- = 10 \text{ mM NaCl}$ solution was used. Note: The waves on the aqueous phase are drawn to indicate a liquid. (b) Picture of the experimental setup. The casing is made of polymer plates tightened together by 3 mm bolts. The AEM's are fixed in between the layers with silicone gaskets. (1) One of the four bolts is attached to a vibrator. The vibration frequency is 50 Hz with an amplitude of 1 mm. (2) Connection to the Pt anode. (3) Connection to the Pt cathode. (A) and (B) AgCl reference 1 and 2 respectively.

In Fig. 3.4 we see that the two curves show the same initial slope. The inverse of the slope is the ohmic resistance of the system. When the current density reaches $i_{\text{lim}} = 1.3 \text{ mA cm}^{-2}$, the two curves separate. The plateau arises because the anion concentration is zero near the membrane surface and in order to increase the current further water must dissociate. In the later process a small potential barrier is involved and hence the current becomes stagnant for a while. The experiments proved that mass transport can affect the electrical resistance of an ion exchange membrane.

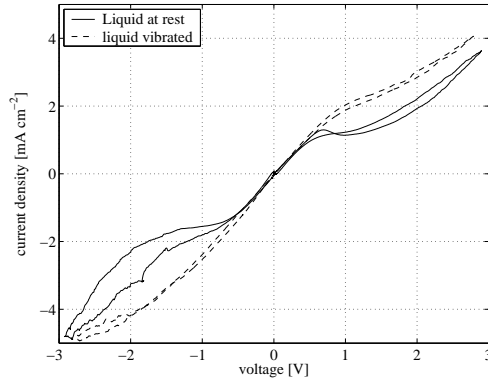


Figure 3.4: Plotting the current density as function of potential difference $V_A - V_B$ across the AEM. The applied voltage is swept from -5 V to 5 V starting at 0 V and the sweep rate is 20 mV/s. Area of membrane: $A = 0.79$ cm², buffer concentration: $c = 10$ mM, limiting current: 1.3 mA cm⁻², anion diffusion constant: $D_- = 2.0 \times 10^{-9}$ m² s⁻¹. Thickness of diffusion boundary layer $\ell = 303$ μ m which is very thick because the fluid is stagnant.

3.4 Sealing and fluidic connections

The polymer based EO pumps consist of modules adjoined by mechanical force. The modular construction allows for easy interchange of components which is beneficial in the development process. A good sealing is achieved by sandwiching a soft material, e.g. thermoplastic elastomer, between a hard material, e.g. PMMA. The spacing between the compression points, i.e., nuts and bolts, are 12.7 mm. With that spacing the thickness of the last PMMA layer must be more than 3 mm to give the necessary overall compression, i.e. leakproof to more than 2 bar. The channels made in the spacer layer δ reduce the compression between the β and ζ layers, see Fig. 3.5. This can lead to leakage from the through holes to the open reservoirs. The problem was solved by redirecting the flow to the backside of the frit. The problem was solved by redirecting the flow to the backside of the frit.

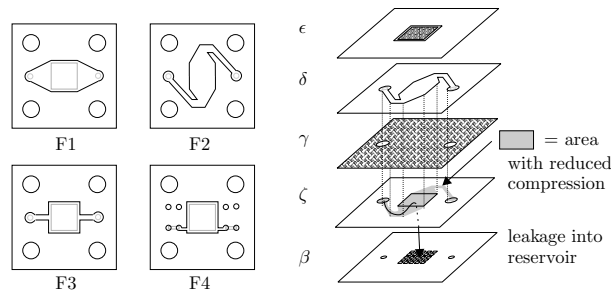


Figure 3.5: Different versions of the feed system. The first three versions F1-F3 all have problems with leakage due to lack of compression between layer γ and ζ . This problem was finally solved in version F4 by redirecting the flow to the backside of the frit, see also Fig. 3.2(b). In this way the rigid PMMA layer ζ will ensure a uniform compression and be leakproof to more than 2 bar.

The tubing is mounted perpendicular to the α layers. A very robust permanent interconnection without the need for expensive fittings was developed, see Fig. 3.6. The depth of the hole should be at least 2 mm and preferably 3 mm. Otherwise the fitting will be fragile to wiggling of the tube. The threads helps the epoxy to physically lock the assembly. If the fitting hole has to bond against another plate the thread should be made prior to bonding since it is very difficult to make a bottom thread without destroying the bonding.

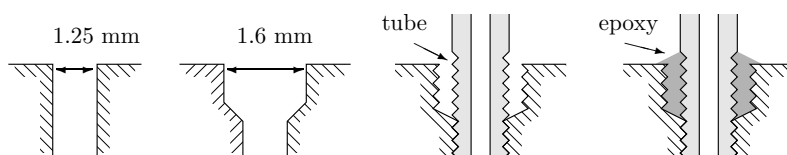


Figure 3.6: Mounting a tube perpendicular to the plane. First two holes are drilled. Then a 1.6 and 2.0 mm threading is made. The teflon tube, which is softer than PMMA, can be screwed into place without any thread. Finally, epoxy is applied for sealing purposes. The junction has been successfully tested leakproof to more than 7 bar.

3.5 Buffer conductivity and pH

Electroosmotic flow has the highest mobility at high pH values, see Fig. 3.8(a). Therefore an alkaline buffer such as borax is suited for EO pumping. A low buffer concentration is preferable because it give a high mobility and efficiency, see Fig. 3.8(b). However, if it is too low there may be problems with Debye layer overlap and day-to-day reproducibility. The properties of the used concentrations are shown in Table 3.3.

concentration mM	pH	temperature °C	conductivity ($\Omega \text{ m}$) ⁻¹
1	9.04	23.7	1.59×10^{-2}
5	9.08	23.8	7.23×10^{-2}
20	9.12	23.9	2.58×10^{-1}
100	9.35	23.9	9.98×10^{-1}

Table 3.3: Values of the borax buffer ($\text{Na}_2\text{B}_4\text{O}_7$) conductivity at different ionic concentrations. Measured with a Radiometer CMD210 conductivity meter.

In crystalline form the molecular formula is $\text{Na}_2\text{B}_4\text{O}_7 \cdot 10 \text{H}_2\text{O}$. The crystal is organized as $\text{Na}_2\text{O} + 2(\text{B}_2\text{O}_3)$. The buffer dissociates as boric acid and its conjugate base. $\text{Na}_2\text{B}_4\text{O}_7 + 7 \text{H}_2\text{O} \rightarrow 2 \text{H}_3\text{BO}_3 + 2 \text{B}(\text{OH})_4^- + 2 \text{Na}^+$. Boric acid is a divalent acid: $\text{H}_3\text{BO}_3 + \text{H}_2\text{O}$

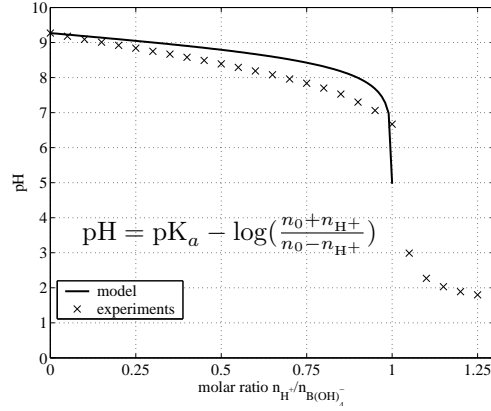


Figure 3.7: Titration of borax buffer; model and experiments. One mole of $\text{Na}_2\text{B}_4\text{O}_7$ buffer can absorb two moles of H^+ before the pH value changes considerably. The reason is that one mole of borax gives two moles of boric acid. The pH was adjusted with HCl.

$\rightleftharpoons \text{H}_2\text{BO}_3^- + \text{H}_3\text{O}^+$ with $\text{pK}_a = 9.27$ and $\text{H}_2\text{BO}_3^- + \text{H}_2\text{O} \rightleftharpoons \text{HBO}_3^{2-} + \text{H}_3\text{O}^+$ with $\text{pK}_a > 14$. The latter pK_a value is so high that the reaction is irrelevant to our case.

It is possible to calculate the exact pH if the reaction scheme is known. In this case we assume full conversion according the reaction scheme. The agreement between theory and experiments is reasonable, Fig. 3.7. Especially the point of pH change is very well resolved by the pH model.

The pH and concentration are the two main parameters for the buffer. A borax buffer with pH = 9.2 was used in all experiments. The concentration can be varied in order to adjust the Debye length. EO mobility measurements from Ref. [18] in silica capillaries are shown in Fig. 3.8(b). From this figure it can be seen that is it far from optimal to use concentrations higher than $c = 1$ mM.

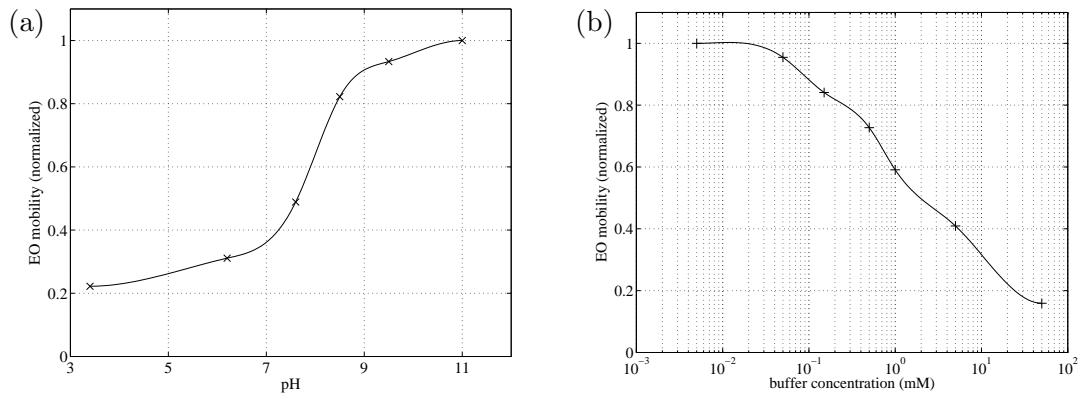


Figure 3.8: Dimensionless EO mobility in a silica capillary, [18]. (a) EO mobility α_{eo} dependence on pH. The pH of a 0.5 mM borax solution was modified by the addition of NaOH or HCl. (b) EO mobility α_{eo} dependence on borax electrolyte concentration c .

3.5.1 Ion transport

The ion transport is closely related to the EO pumping mechanism. The choice of ion exchange membranes has a large influence on the ion transport. It is quite difficult to obtain any information about specific ion concentrations within the pump. The following schemes therefore only represent my working hypothesis of the ion transport.

There are three transport processes involved: diffusion, convection and electromigration. In the following we assume that the pump is in a stationary state, hence no ions can accumulate anywhere. Table 3.4 shows the possible electrode reactions depending on the pH of the environment.

electrode	reaction	pH change
anode (pH > 7):	$4 \text{ OH}^- - 4e^- \rightarrow \text{O}_2 + 2\text{H}_2\text{O}$	↓
anode (pH < 7):	$2 \text{ H}_2\text{O} - 4e^- \rightarrow \text{O}_2 + 4\text{H}^+$	↓
cathode: (pH > 7)	$4 \text{ H}_2\text{O} + 4e^- \rightarrow 2\text{H}_2 + 4\text{OH}^-$	↑
cathode: (pH < 7)	$4 \text{ H}^+ + 4e^- \rightarrow 2\text{H}_2$	↑

Table 3.4: Redox reactions taking place at the anode and cathode. In total the pH is unchanged. The cathode forms twice as much gas as the anode. Both observations agrees well with experiments.

In the EO pump literature both cation and anion exchange membranes have been used. The diagrams in Fig. 3.9 display the differences in the ion transport. Hence, two cases have been investigated. A configuration with two cation exchange membranes (CEM) and two anion exchange membranes (AEM). The CEM configuration is believed to be less stable because it introduces hydronium ions H^+ into the frit environment (B-D). Depending on the magnitude of buffer inflow to the frit this mechanism could render the EO pump unstable. Imagine that the pump is stalled for a while, the subsequent lowering of the pH close to the frit will decrease the EO flow. Once the pump is released from the stall condition it may not recover its original flow rate due to the decrease in surface charge.

The AEM configuration is much better in this regard because the current is transported by hydroxide ions (OH^-). These suggested mechanisms are, however, somewhat speculative since it is not possible to measure any concentrations or pH levels in the region (B-D). The AEM configuration has been tested by far the most. The liquid draining of the cathode and filling of the anode chamber have also been observed experimentally. Due to the electric field there must be a gradient in concentration of cations from B (high) to D (low). In a stationary state the diffusion must balance the electromigration of the cations. A few additional comments to the ion transport are made in Chap. 9.

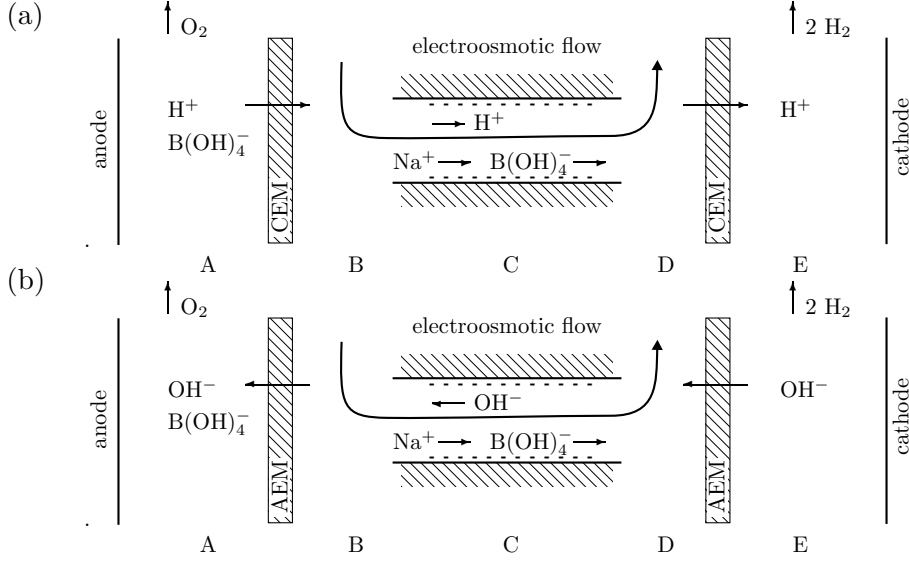


Figure 3.9: (a) Pumping configuration with cation exchange membranes (CEM). The disadvantage of the configuration is that the current will be transported by hydronium ions and hereby lowering the pH in region (A-D). (b) Configuration with anion exchange membranes (AEM). In this case the current will be transported by hydroxide ions ensuring a high pH in region (B-E).

3.6 Theoretical flow characteristics

In this section two different models for the EO flow characteristics are presented. The first flow model in Sec. 3.6.1 is based on the Debye-Hückel approximation. The approximation is that $\frac{z_i \phi}{kT} < 1$ is small so that $\exp(\frac{z_i \phi}{kT}) \approx 1 - \frac{z_i \phi}{kT}$ can be linearized. The approximation is only accurate for relatively small ζ -potentials because $kT/e = 25.7$ mV at room temperature.

In the second model we investigate the relation between EO flow and electrical current. The found relation can be used to predict the difference between operating the pump at a constant voltage or a constant current. This model does not invoke the Debye-Hückel approximation but solves the nonlinear boundary value problem numerically.

3.6.1 Debye layer overlap

The Eqs. (2.1) to (2.4) states that the flow rate Q_m and pressure Δp_m depends on the Debye layer overlap. In Fig. 3.10 the equations are plotted. The Debye-Hückel approximation will be accurate for mobilities, $\alpha_{eo} < 3 \times 10^{-8} \text{ m}^2 (\text{V s})^{-1}$.

We note that a $\lambda_D/a = 1$ ratio decreases the flow rate by a factor 10. In terms of performance it may therefore be beneficial to use a more concentrated buffer even though it lowers the mobility according to Fig. 3.8(b). For each channel size there is an optimum buffer concentration.

The maximum achievable pressure is $\Delta p_m / \Delta V = 1 \text{ bar V}^{-1}$ for $\alpha_{eo} = 1 \times 10^{-8} \text{ m}^2 (\text{V s})^{-1}$ and $\lambda_D = 10 \text{ nm}$. In the Debye-Hückel limit the maximum EO pressure per volt $\Delta p_m / \Delta V \propto \alpha_{eo} \lambda_D^{-2}$.

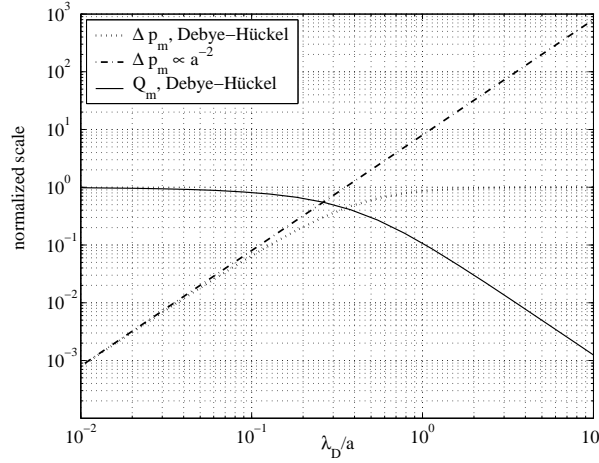


Figure 3.10: Theoretical model of the flow rate and pressure in a porous frit with pore size a . The Debye layers begin to overlap at $\lambda_D/a \approx 0.1$. As a result the flow rate starts to decrease. The pressure capacity increases slowly until $a/\lambda_D \approx 1$ where it becomes stable. In absolute values: $\Delta p_m/\Delta V = 1 \text{ bar V}^{-1}$ for $\alpha_{eo} = 1 \times 10^{-8} \text{ m}^2 (\text{V s})^{-1}$ and $\lambda_D = 10 \text{ nm}$.

3.6.2 Relation between flow and electrical current

The following section is based on the paper *Nanofluidic components for electrokinetic micropumps* by A. Brask, Jörg P. Kutter and H. Bruus, [11].

Consider a cylindrical channel in (r, θ, z) -coordinates of radius a filled with some buffer liquid with viscosity μ and dielectric constant ϵ . Ions of symmetric valence Z are present in concentrations $c_+(r)$ and $c_-(r)$. Chemical charge-transfer processes at the wall spawn an electric potential ζ , the so-called zeta potential, adjacent to the walls and lead to a potential $\phi(r)$ in the liquid. Given the boundary conditions $\phi(a) = \zeta$ and $\phi'(0) = 0$ we find $\phi(r)$ and $c_{\pm}(r)$ by standard numerical methods as self-consistent solutions to the Poisson-Boltzmann equation.

For a given electric field E_z and pressure gradient $\nabla_z p$ imposed in the z direction the velocity field $u(r)$ is found by solving the Navier-Stokes equation. When $E_z = 0$, it is the Poiseuille flow $u_p(r, \nabla_z p) = -\nabla_z p (a^2 - r^2)/4\mu$ and, when $\nabla_z p = 0$, it is the Helmholtz-Smoluchowski flow $u_{eo}(r, E_z) = \alpha_{eo}(1 - \phi(r)/\zeta) E_z$, where $\alpha_{eo} = -\epsilon\zeta/\mu$ is the electroosmotic mobility. By integration the flow rate Q is found to be

$$Q(E_z, \nabla_z p) = \int_0^a 2\pi r \left[u_{eo}(r, E_z) + u_p(r, \nabla_z p) \right] dr. \quad (3.10)$$

The electric current density in the channel is a sum of the ordinary ionic electromigration and, because of charge imbalance, the convection of ions. The current I is found by

integration of this current density,

$$\begin{aligned}
I(E_z, \nabla_z p) = FZ \int_0^a 2\pi r \left\{ [c_+(r) + c_-(r)] \alpha_{ep} E_z + \right. \\
\left. [c_+(r) - c_-(r)] u_{eo}(r, E_z) \right\} dr + \\
FZ \int_0^a 2\pi r \left\{ [c_+(r) - c_-(r)] u_p(r, \nabla_z p) \right\} dr. \tag{3.11}
\end{aligned}$$

Recalling that $u_{eo} \propto E_z$ and $u_p \propto \nabla_z p$, Eqs. (3.10) and (3.11) can be written as linear functions of E_z and $\nabla_z p$. By introducing the constants β_E , β_p , γ_E , and γ_p we find,

$$Q(E_z, \nabla_z p) = \gamma_E E_z - \gamma_p \nabla_z p, \tag{3.12}$$

$$I(E_z, \nabla_z p) = \beta_E E_z - \beta_p \nabla_z p. \tag{3.13}$$

We base our flow regulator theory on these linear equations. Let E_z^0 be a reference field, and calculate for $\nabla_z p = 0$ the corresponding current $I^0 \equiv \beta_E E_z^0$ and flow rate $Q^0 \equiv \gamma_E E_z^0$. For fixed E_z^0 an applied backpressure $\nabla_z p$ will reduce Q from Q^0 linearly with slope $-\gamma_p$,

$$Q(E_z^0, p) = Q^0 - \gamma_p \nabla_z p. \tag{3.14}$$

From this we find the so-called electroosmotic pressure $\nabla_z p_{eo}^0 = Q^0/\gamma_p$, which is the backpressure gradient that makes the flow rate zero, $Q(E_z^0, \nabla_z p_{eo}^0) = 0$.

Now we allow for changes in E_z . In particular we define E_z^p as the field that for a given backpressure gradient $\nabla_z p$ maintains the current at the original value I^0 , i.e., $I(E_z^p, \nabla_z p) = I(E_z^0, 0)$, which can be solved to yield

$$E_z^p = E_z^0 + \frac{\beta_p}{\beta_E} \nabla_z p. \tag{3.15}$$

Upon insertion of E_z^p and into Eq. (3.12) we obtain a new linear function for Q ,

$$Q(E_z^p, p) = Q_0 - \Gamma_p \nabla_z p, \quad \text{where } \Gamma_p = \gamma_p - \frac{\beta_p}{\beta_E} \gamma_E. \tag{3.16}$$

Thus by applying a simple current feedback that keeps the electric current I constant by changing E_z , the Q - p slope can be reduced from γ_p to Γ_p , thereby keeping the backpressure-induced loss in the flow rate Q to a minimum. The new slope Γ_p also changes the backpressure capacity,

$$\nabla_z p_{eo}^p = \nabla_z p_{eo}^0 (\Gamma_p/\gamma_p)^{-1}. \tag{3.17}$$

Note that, regardless of this change in backpressure capacity the pump efficiency measured as $\nabla_z p/E_z$ remains unchanged. Figs. 3.11(a-b) shows Γ_p/γ_p as a function of the Debye length λ_D and the mobilities α_{eo} and α_{ep} respectively. Perfect flow control corresponds to $\Gamma_p = 0$ equivalent of infinite backpressure capacity. The lowest calculated value of $\Gamma_p \approx 0.5$, based on realistic values for α_{ep}/α_{eo} , promises a two-fold increase in the backpressure from the regulation alone.

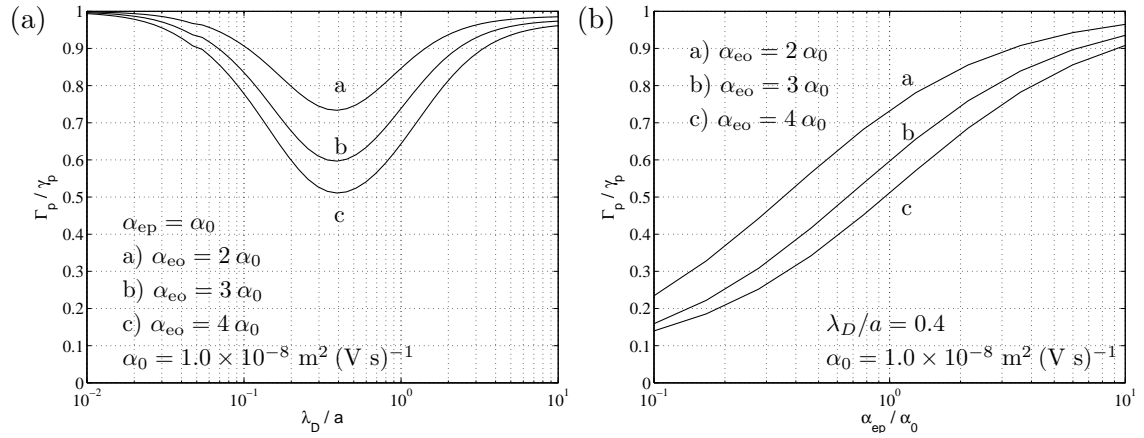


Figure 3.11: (a) The slope $\Gamma_p = dQ/d\nabla_z p$ as a function of λ_D/a and α_{eo} . The mobilities are given in units of $\alpha_0 = 10^{-8} \text{ m}^2/(\text{V s})$. (b) Γ_p as a function of α_{ep} for $\lambda_D/a \approx 0.4$, which is the value in diagram (a) that minimizes Γ_p .

Chapter 4

Microvalves overview

A check valve allows fluid flow in one direction and stops, or checks, fluid flow in the opposite direction. In this chapter we describe different check valve principles that are suitable as rectifying valves in an AC electroosmotic pump, see Chaps. 5, 6 and 7. Three different types of passive check valves have been developed: (1) A mobile polymer plug valve, (2) a membrane slit valve and (3) a foam valve. All valves are designed to be used in a micropump with an EO actuator. The structure of the chapter is the following; in Sec. 4.1 some of the important valve parameters are outlined. Then follows a description of commercially available minivalves. And finally, we describe the three valve concepts that have been developed and characterized.

4.1 Valve parameters

In macroscopic fluid dynamics the concept of dynamic and static pressure is often useful. Static pressure is the pressure when fluid is at rest. Dynamic pressure is the pressure when the fluid is in motion, $p_{\text{dyn}} = p_{\text{sta}} + \frac{1}{2}\rho u^2$, where ρ and u is the density and velocity of the fluid respectively. In macroscopic valves, e.g., flap valves this pressure difference can be used for actuation. The same principle does not work in the low Reynolds number regime. Due to lack of inertia forces the valve is not affected by the flow direction in the same way. As a consequence a microvalve should be closed by default to avoid leakage. This is termed pre-loading.

The EO pumps in consideration can supply flow rates and pressures of the order $Q_m = 1 - 10 \mu\text{L min}^{-1}$ and $\Delta p_m = 1 - 10 \text{ bar}$. Typical stroke volumes are of the order $V_{\text{stroke}} = 1 - 5 \mu\text{L}$. A suitable check valve should be designed accordingly. There are some important parameters we shall use to characterize our check valve.

4.1.1 Flow resistance and diodicity

Typically one is interested in a low flow resistance in the forward direction R_{open} and a high or infinite resistance in the other direction R_{closed} . The ratio between the hydraulic resistances in backward and forward direction is termed the diodicity, $R_{\text{closed}}/R_{\text{open}}$. A good rectifying valve has a large diodicity.

4.1.2 Internal volume

The internal volume is the total fluid filled volume of a fluidic component, e.g. a valve. The internal volume may be divided into a swept volume and a dead volume $\mathcal{V}_{\text{int}} = \mathcal{V}_{\text{swept}} + \mathcal{V}_{\text{dead}}$. The dead volume is the volume of stagnant liquid when the valve is open. The swept volume is the remaining volume, see Fig. 4.1. The swept volume is closely related to the flow resistance of the valve. If the valve is used for different types of liquids a large dead volume can increase the necessary flushing time to avoid cross contamination. Dead volume can also trap bubbles and thereby add compliance to the system. The conclusion is therefore that it is always a good idea to minimize the dead volume.

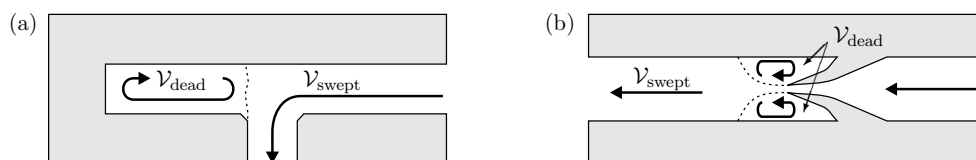


Figure 4.1: (a) Flow through a component with a dead end. The internal volume is the sum of swept and dead volume, $\mathcal{V}_{\text{int}} = \mathcal{V}_{\text{swept}} + \mathcal{V}_{\text{dead}}$. (b) Downstream of obstacles, e.g. a duckbill valve, recirculating flow regions usually occur even in low Reynolds flow. These regions are also considered to be dead volume.

4.1.3 Opening pressure

Pre-loaded valves are "normally closed". A normally open valve will have some small amount of leakage when pressure is applied in the reverse direction, until enough pressure is applied to urge the valve to shut. A normally closed valve does not require reverse pressure to seal. Pre-loaded valves will require some pressure, i.e. the opening pressure, in the forward flow direction to obtain the onset of flow.

4.1.4 Valve history

The behavior of the valve can be dependent on the valve history. If the valve has been holding of unusual high pressures the plug or membrane can be jammed against the valve seat. This can cause the subsequent opening pressure to be higher than normal. This effect is usually not desirable because it is uncontrollable.

4.1.5 Robustness

Finally, the robustness of the valve is of great practical importance. A microvalve is inherently exposed to collecting particles and bubbles from the flow. A robust valve should have a high particle tolerance. But in general filters or clean solutions should be used for reliable valve operation. The particle tolerance is an important parameter for a microvalve.

4.2 Duckbill and umbrella valves

Duckbill and umbrella valves are typically made of thermoplastic elastomer by injection moulding. These devices are commercially available in sizes above 2 mm. The principle is well suited to microfluidics since both valve types can be pre-loaded, see Fig. 4.2.

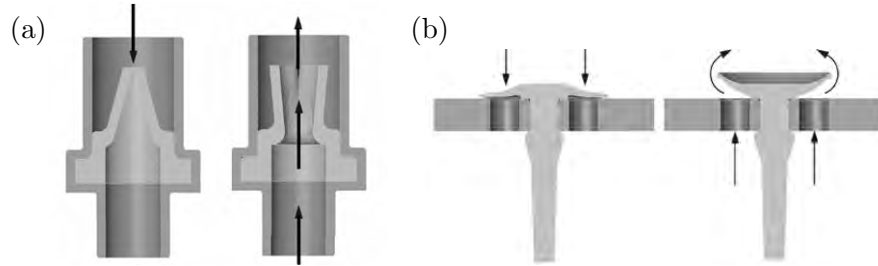


Figure 4.2: (a) Duckbill valves have a small or none pre-load built in its design. Static pressure differences opens and closes the valve. (b) Umbrella valves have a larger amount of pre-load built in its design. It can be controlled by the geometry of the cap. Static pressure differences opens and closes the valve. These valves are typically larger than the duckbill design. Courtesy of Minivalve International, [33].

Different types of duckbill and umbrella valve were investigated in preliminary tests. The smallest duckbill valve available was 2 mm in diameter. Including the valve mount the internal volume would be approximately $\mathcal{V}_{\text{int}} = 10 \mu\text{L}$ where more than half of that volume would be dead volume. Furthermore it was found that the duckbill valve is extremely susceptible to collecting particles and as a consequence likely to leak at low flow rates. The smallest umbrella valve was 6 mm in diameter and hence too large.

Both valve types have a considerable amount of compliance due to their flexible nature $K = 1 - 10 \mu\text{L bar}^{-1}$. The conclusion was that the commercially available minivalves could not fulfill the requirements for an EO actuated micropump.

4.3 Foam valve

The foam valve is similar in concept to a spring-loaded valve. Instead of using a spring a block of polymer foam is used to exert a uniform pressure on the part of the membrane that seals the valve, see Fig. 4.3. The foam can either be porous or nonporous. A working prototype was constructed but not fully characterized. The pre-load of the valve is governed by the compression ratio and the modulus of elasticity (Young's modulus) of the foam.

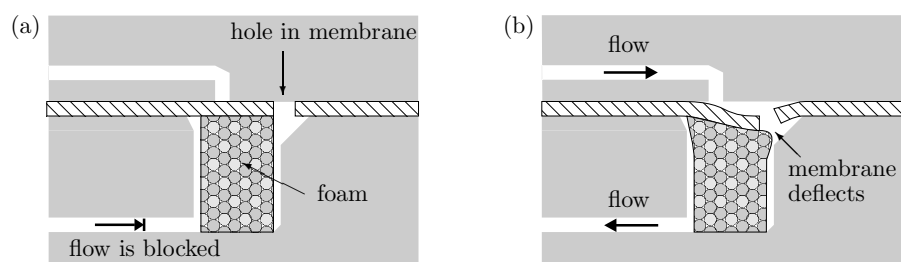


Figure 4.3: Schematics of the foam valve. (a) In the closed mode the foam presses the membrane against the valve seat and hereby prevents any leakage. (b) In the open mode the membrane is deflected and flow may pass through the membrane hole.

A valve with porous foam will have a larger internal volume than a valve with nonporous foam. However, a nonporous foam will often have a very high Young's modulus causing a prohibiting large opening pressure. The polymer foam should also be compatible with the bonding temperature of $T_b = 109\text{ }^\circ\text{C}$ in order to avoid plastic deformations. The TPE membrane bonded very well to the PMMA substrates. Hence after bonding the valve required a high initial opening pressure $\approx 1\text{ bar}$ in order to release the membrane from the valve seat.

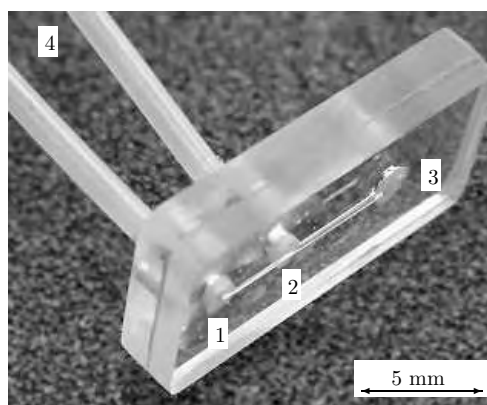


Figure 4.4: Picture of the foam valve. (1) Inlet, (2) outlet, (3) 1.5 mm bore cavity for the foam block and (4) external tubing attached to the devices using the method described in Fig. 3.6.

The PMMA substrates and membrane were structured using the CO₂ laser and subsequently bonded, refer Secs. 6.5.2 and 6.5.3. The block of foam was inserted manually before bonding. A working prototype is depicted in Fig. 4.4. The internal volume of the prototype is approximately $\mathcal{V}_{\text{int}} \approx 5 \mu\text{L}$. The compliance has not been measured but is estimated to be of the order $K \approx 1 \mu\text{L bar}^{-1}$.

4.4 Membrane slit valve

The membrane slit valve is used in macroscopic applications as a cheap and robust check valve. A 3D illustration of the valve concept can be seen in Fig. 4.5. The valve is depicted in the open mode where the membrane is deflected into the cavity. The stress in the membrane expands the slit and thus opens the valve. Traditionally, two perpendicular slits are made forming a cross. In this way the hydraulic resistance is lowered considerably compared to the single slit configuration.

However, it was found that the single slit configuration seals better than a cross slit configuration. In the case of a cross slit valve the flaps may get stuck after being deflected in the opening direction. In microfluidic applications is very important the the valve is default closed in order to prevent leakage.

It was not possible to find any literature about the membrane slit valve. Hence a material and geometry study was carried out. The testing was very successful and after a couple of months a working prototype was constructed. The flow characteristics of the check valve is given in Chaps. 5 and 6.

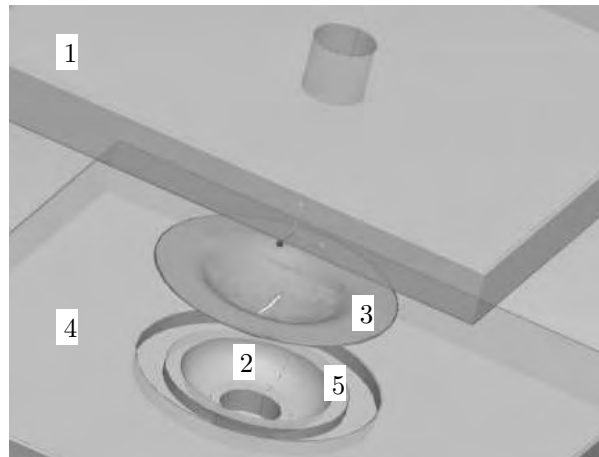


Figure 4.5: Illustration of the membrane slit valve. When the flow comes from (1) the top layer (3) the membrane deflects into (2) the cavity and the slit in the center of the membrane expands. In this configuration the valve is open. If the flow comes from (4) the bottom layer the membrane cannot deflect and the slit remain closed. (5) The protruding rim ensures that no radial flow can bypass the membrane. Courtesy of Detlef Snakenborg.

4.5 Mobile polymer plug valve

The mobile polymer plug valve concept was originally developed at Sandia National Laboratory in Livermore CA, USA, [34, 35, 36]. An illustration of the valve principle is shown in Fig. 4.6(a). Pictures of an open and a closed valve are shown in Figs. 4.6(b) and (c), respectively. The mobile plug is shifted in its position by differential pressures. In the open direction the flow can bypass the plug whereas in the closed direction the plug seals of the channel.

We simplified the valve fabrication method and developed a 4-valve rectifying system. My work with the mobile plug valves is described in Chap. 7.

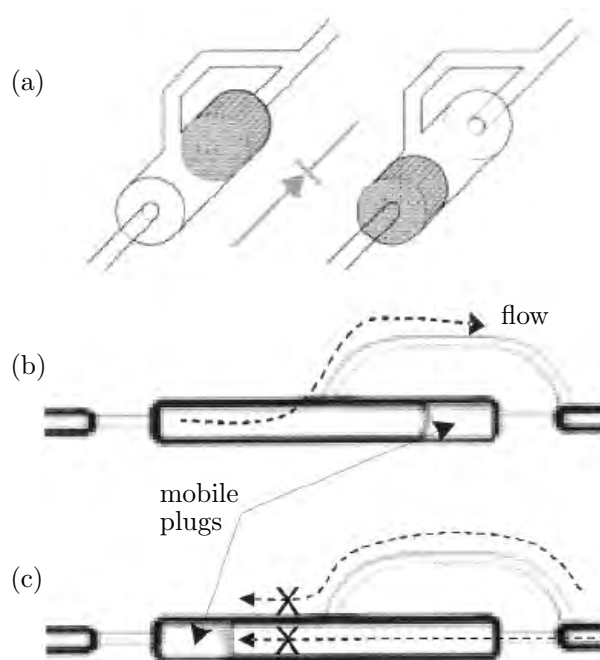


Figure 4.6: (a) Schematic of the mobile plug valve principle. (b) Flow direction is indicated by dashed lines. Flow from left to right bypasses the plug seated against the right stop. (c) Flow from right to left is prevented when the plug seats against the left stop, checking the flow. The channel diameters are approximately 100 and 25 μm . Courtesy of Hasselbrink *et al.*, [35].

Chapter 5

AC EO pump with membrane valves

5.1 Introduction

Although the DC EO pump from Chap. 2 was relatively stable there was still a room for improvements. The DC EO pump would render unstable in the case of stall conditions and due to the development of electrolytic gases it empties the electrode reservoirs over time. It was found that by using a special electrode material, such as palladium, the electrolytic gases could be eliminated when the pump was operated with alternating currents (AC). The disadvantage about AC operation is that the induced flow must be rectified by a system of valves. The initial experiments with bubble-free palladium electrodes and microvalves were made at University of Michigan. The bubble-free electrodes worked well but the mobile polymer plug valves were not reliable enough, see chap. 7. After returning from Michigan a different valve system was constructed and integrated with the existing DC EO pump described in chap. 2 but now with bubble-free electrodes. The work resulted in the following paper.

5.2 A. Brask *et al.*, Lab Chip, 2006, 6, 280-288

beginning of paper

AC electroosmotic pump with bubble-free palladium electrodes and rectifying polymer membrane valves

Anders Brask, Detlef Snakenborg, Jörg P. Kutter, and Henrik Bruus
*MIC – Department of Micro and Nanotechnology, DTU bldg. 345 east
Technical University of Denmark, DK-2800 Kongens Lyngby, Denmark*

We present the design, test and theoretical analysis of a novel micropump. The purpose is to make a pump with large flow rate ($\approx 10 \mu\text{L min}^{-1}$) and high pressure capacity ($\approx 1 \text{ bar}$) powered by a low voltage $\Delta V < 30 \text{ V}$. The pump is operated in AC mode with an electroosmotic actuator in connection with a four-way rectifying valve system. Individual valves are based on a flexible membrane with a slit. Bubble-free palladium electrodes are implemented in order to increase the range of applications and reduce maintenance.

5.2.1 Introduction

Electroosmotic (EO) actuators are suitable for microfluidic applications because they can produce high pressures and precise flow. The increased interest in studying and applying them is reflected in the recent review papers (and the references therein) by Stone, Stroock and Ajdari [1], Laser and Santiago [3], and Squires and Quake [37].

In EO actuators an electrolyte is pumped by applying an electric field to the Debye layer. This layer is formed by the ions in the electrolyte due to electric screening of the immobile charges on the walls of the liquid channels within the pump [5, 6]. High pressures ($\sim 1 \text{ kPa V}^{-1}$) and large flow rates ($\sim 1 \mu\text{L min}^{-1}\text{V}^{-1}\text{cm}^{-2}$) are achieved in these actuators by using capillaries or micro/nanoporous frits to form the pumping liquid channels [23, 21, 38, 9, 25].

An EO pump can be improved in several ways: the cascade-pump design lowers the driving voltage [20], the addition of zwitterionic additives enhances the pressure [22], and, as shown in our own recent work, carefully integrated ion exchange membranes increase the stability [10]. Nevertheless, an EO pump operated continuously in DC mode, as those mentioned above, suffers from inherent problems. Electrolysis generates gas bubbles, which must be removed or recombined from the system [25, 24]. Redox reactions at the electrodes will eventually change the pH, which is a problem because the EO flow depends on it. In the case of pump stall conditions $Q = 0$ the EO flow is recirculating within the pumping channels and thereby generating pressure. The pH change introduced at the electrodes will stop the EO flow after a while when the buffer is depleted.

To overcome these problems with the DC drive, various electrokinetic devices that run in AC mode have been tested: electrothermally induced fluid flow [39], surface-electrode driven EO flow [40], and travelling wave EO flow [41]. Common to these devices are that although the flow rates (measured in the unit $\mu\text{L min}^{-1}\text{V}^{-1}\text{cm}^{-2}$) are comparable to the above mentioned, their pressure capacities are low, typically only $1 - 10 \text{ Pa V}^{-1}$. The main application of these devices are manipulation of suspended particles.

In this paper we combine the high pressures and large flow rates (measured in $\mu\text{L min}^{-1}\text{V}^{-1}$) of the porous or frit-based DC EO pump with the advantage of bubble-free AC operation. This is achieved by mounting a novel rectifying valve system based on polymer membranes onto our recently developed DC EO pump [10]. As a second novelty, we suppress the generation of bubbles by employing palladium electrodes that can store and release hydrogen reversibly.

The paper is organized in the following way: in Sec. 5.2.2, we introduce the general

concept of the pump and its novel features. The EO actuator used in this context has been described in a previous paper [10], hence only a brief description of it is given in Sec. 5.2.3. The palladium electrodes are described in detail in Sec. 5.2.4, while the rectifying valve system is described in Sec. 5.2.5. Integration issues such as compliance are discussed in Sec. 5.2.6. The pumping results are presented in Sec. 5.2.7 and, finally, we give an outlook and draw conclusions in Secs. 5.2.8 and 5.2.9, respectively.

5.2.2 General concept

Operating a symmetric EO pump in AC does not give any net flow if no net current is drawn. The flow will only oscillate back and forth. Hence, we introduce a system of rectifying valves, see Fig. 5.1. When the valve system is coupled to the oscillating EO actuator a net rectified flow is generated. This system is very similar to existing piezo-actuated membrane pumps [3]. The main difference is the actuator type and the number of valves. Also note that depending on the stroke volume the pumped liquid may enter and exit the valve system without ever entering the EO actuator. In this way the AC EO pump is less dependent on the pumped liquid than conventional DC EO pumps and with a separator system it could be completely independent.

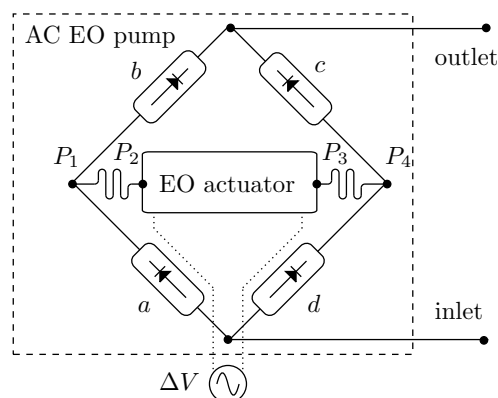


Figure 5.1: Diagram of the AC EO pump with four rectifying valves *a*, *b*, *c*, and *d*. The components and channels within the dashed box comprises the AC EO pump. The solid lines are fluid channels while the dotted lines are electrical wires. The four-way valve system ensures that both stroke directions generate flow in contrast to a two-way valve system where only one stroke direction generates flow. If the driving voltage is positive, the flow goes from the inlet through valve *a*, the EO actuator and valve *c* to the outlet. For negative voltage, the flow goes from the inlet through valve *d*, the EO actuator and valve *b* to the outlet. The black dots marked P_1 - P_4 are used to explain Fig. 5.4.

Another difference between a conventional membrane pump and this pump is that the force from the actuator is directly applied to the liquid without the use of a displacement chamber. The disadvantage of this is that the actuator liquid may get mixed with the pumped liquid. The main advantages, on the other hand, are a simple design and less compliance from, e.g., trapped bubbles.

5.2.3 EO actuator

The EO actuator design is based on the DC EO pump presented by Brask *et al.* [10]. The original frit-based EO pump features ion exchange membranes to separate the electrode reservoirs from the pumping loop. The present pump configuration is almost the same as described earlier and differs only in two areas. (1) The ion exchange membrane support has been improved in order to accommodate the low compliance requirements. (2) Platinum (Pt) electrodes have been replaced by bubble free palladium (Pd) electrodes allowing for a more encapsulated reservoir with less maintenance.

The essential parameters for an AC actuator are the stroke volume V_s and the pressure Δp capacity at a given current I and period T . Using the Q/I - $\Delta p/I$ data in Ref. [10] we find that the maximum flow rate and pressure capacity are $Q/I = 6 \mu\text{L min}^{-1} \text{ mA}^{-1}$ and $\Delta p/I = 7 \text{ bar mA}^{-1}$, respectively for a buffer concentration of $c = 20 \text{ mM}$.

In AC mode the current behaves in a highly nonlinear manner because of the depletion of the buffer close to the ion exchange membranes. For more information see Ref. [10]. We therefore base the performance estimates on an average value over a stroke period. At $\Delta V = 30 \text{ V}$ and $c = 20 \text{ mM}$ the current will be in the range $I = 1\text{--}5 \text{ mA}$, Fig. 5.13. Where $I = 1 \text{ mA}$ is the stationary current and $I = 5 \text{ mA}$ is immediately after the voltage switch. With a half period of $T/2 = 30 \text{ s}$ the average current will be approximately $I = 2 \text{ mA}$. This should give a stroke volume of $V_s = 6 \mu\text{L}$. With respect to the pressure capacity it is the current at the end of the stroke that matters. The pressure capacity of the actuator should be approximately $\Delta p = 10 \text{ bar}$.

5.2.4 Bubble-free electrodes

When drawing a current from an inert electrode material, e.g., platinum, in an aqueous solution electrolysis happens. Oxygen is formed at the anode and hydrogen at the cathode. These gases pose a problem for long-term operation since they need to be removed.

Some metals, in particular palladium (Pd), have a high permeability for hydrogen. Running the pump in AC mode will make each electrode work as an anode and a cathode for an equal amount of time. If the hydrogen generated during the cathodic half-cycle is stored in the palladium and removed during the anodic half-cycle, the electrodes will be bubble-free.

The aim of this section is to analyze the bubble formation mechanism and hereby predict the conditions for bubble-free operation.

The bubble formation model

Hydrogen is introduced to the Pd phase through cathodic processes in aqueous media. A maximum H/Pd ratio of 0.57 is reported in Ref. [42]. Using the values for density $\rho_{\text{Pd}} = 12.02 \times 10^3 \text{ kg m}^{-3}$ and molecular weight $M_{\text{Pd}} = 0.106 \text{ kg mol}^{-1}$ we can estimate the maximum concentration of hydrogen to be stored $c_{\text{H,max}} = 0.57c_{\text{Pd}} = 6.4 \times 10^4 \text{ mol m}^{-3}$.

The governing transport mechanism of hydrogen in palladium is diffusion represented by the diffusion constant D . We assume that there exists a critical surface concentration of H, c_{full} . If this ratio is exceeded bubbles will be formed. c_{full} does not equal $c_{\text{H,max}}$

because of energy barriers associated with the phase transition from the aqueous to the palladium phase.

There are two characteristic time scales in this problem. The first one is the diffusion time scale, T_{diff} . At approximately this time hydrogen will have reached the core of the electrode. The second time scale is the time it takes for the electrode to saturate, T_{sat} .

$$T_{\text{diff}} = \frac{a^2}{D} \quad (5.1)$$

$$T_{\text{sat}} = \pi a^2 L_{\text{Pd}} D c_{\text{H}} F I^{-1} \quad (5.2)$$

$$T_{\text{diff}}/T_{\text{sat}} = I(\pi L_{\text{Pd}} D c_{\text{H}} F)^{-1} \quad (5.3)$$

where a and L_{Pd} are the radius and the length of the electrode, respectively. If the ratio between diffusion time T_{diff} and filling time T_{sat} is higher than unity the surface will saturate much faster than the core. This regime is referred to as surface filling. In the case of a small ratio the concentration distribution is more uniform and both core and surface will saturate roughly at the same time. This regime is referred to as core filling.

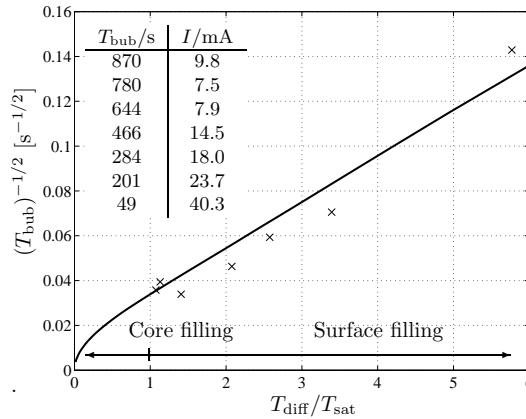


Figure 5.2: Experiments (\times) and simulation (solid line) of the bubble formation time $T_{\text{bub}}^{-1/2}$ vs. the ratio between diffusion time and filling time. The linear regime is denoted surface filling because the hydrogen does not reach the core before bubbles emerges ($c(r = a) > c_{\text{full}}$). In the core filling regime the diffusion is fast compared to the filling and the hydrogen is everywhere. Parameters: $D = 1.0 \times 10^{-11} \text{m}^2 \text{s}^{-1}$, $L_{\text{Pd}} = 40 \text{mm}$, $c_{\text{full}} = 4 \times 10^4 \text{mol m}^{-3}$.

Experiments

The bubble-free electrodes were tested in an open reservoir filled with 5 mM phosphate buffer at pH=6.5. Two spiral shaped palladium wires of length $L_{\text{Pd}} = 40 \text{mm}$ and diameter $2a = 0.25 \text{mm}$ were attached to mobile plates in a long slender reservoir, 2 cm wide, 3 cm deep, and 20 cm long. The hydrogen was removed from the Pd wire by running the wire as an anode. When it was empty (bubbles of O_2 started to form) the current would be reversed and the clock started. After the time T_{bub} bubbles of H_2 would start to form and the clock was stopped. The current was varied by changing the distance between the

electrodes in the range of 2 – 20 cm. A Pd electrode completely loaded with hydrogen would emit bubbles even after the current was stopped. The surface of the Pd would also darken and become more rough after some cycles. However, this did not seem to affect the performance over a time scale of a couple of weeks.

Results

The experimental and model data are plotted in Fig. 5.2. The parameters c_{full} and D in the numerical diffusion model are chosen in order to give the best fit with the experimental data.

Consider a Pd electrode from which a constant current I is drawn. First we need to determine the ratio between diffusion and filling time, Eq. (5.3).

$$T_{\text{bub}} = 5.7 \times 10^7 \frac{\text{A}^2 \text{s}}{\text{m}^4} i^{-2} \quad \text{for } T_{\text{diff}}/T_{\text{fill}} > 1 \quad (5.4)$$

$$T_{\text{bub}} = \frac{c_{\text{full}}}{c_{\text{H}}} T_{\text{fill}}, \quad \text{for } T_{\text{diff}}/T_{\text{fill}} < 1 \quad (5.5)$$

where $i = I/A$ is the current density. In the case of $I = 2$ mA, $L_{\text{Pd}} = 40$ mm, $a = 0.125$ mm, and $D = 1 \times 10^{-11} \text{m}^2 \text{s}^{-1}$ we get the ratio $T_{\text{diff}}/T_{\text{fill}} = 0.26$. This means that we are in the core filling regime, see Fig. 5.2, $T_{\text{bub}} = 3.8 \times 10^3$ s or roughly one hour. The stroke period of the pump is kept at a much smaller value than T_{bub} to ensure bubble-free operation.

5.2.5 Valve system

The purpose of the valve system is to rectify the pulsating flow. In order to do that the individual valves must fulfill some requirements. The actuator can supply flow rates in the order $1 - 10 \mu\text{L min}^{-1}$ and pressures in the range 1 – 10 bar. The valves should open at a low pressure ≈ 0.1 bar and be as tight as possible. The valve module is separated from the actuator module in order to increase the flexibility. In the following we present a simple but effective valve design based on a planar membrane with a slit. The chosen approach allows fast and easy fabrication using polymer materials.

Valve design

Membrane valves are suitable for microfluidic systems because the planar design is easy to integrate. Today membrane valves are commonly used in microfluidics as pressure actuated active valves [43, 44]. The presented valve is a passive membrane valve design inspired by commercially available miniature valves such as duckbill and umbrella valves [33].

The valve consists of a flexible membrane in which a slit or cross has been made. The membrane is placed between a rigid plane with an inlet hole on one side and a cavity with an outlet hole on the other side, see Fig. 5.3. The valve opens when the membrane is deflected into the cavity and hereby expands the slit or cross. The slit or cross is made

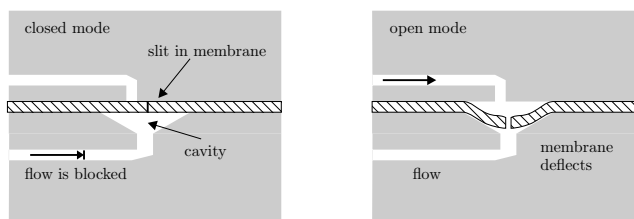


Figure 5.3: This passive membrane valve is pre-loaded because no material was removed when the slit was cut. Hence the slit is so narrow that fluid will not pass without a substantial pressure drop that will compress the slit even further. Note that the inlet is slightly offset to the slit in order to make the valve more tight.

with a sharp tool so that no material is removed. This is an important point because it means that the valve is pre-loaded, i.e., it takes a certain pressure to open the valve.

In microfluidics the lack of inertia forces requires that microvalves are pre-loaded, in order to prevent leakage. The amount of pre-loading is governed by the thickness and Young's modulus of the membrane and by the cavity diameter.

The hypothesis is that the valve will open when the ratio between membrane deflection and thickness reaches a certain threshold. It is, however, not easy to measure the deflection precisely. Instead we measure the pressure drop across the membrane and calculate the deflection. In Ref. [45] an analytical expression for the small deflection of a thin circular membrane with clamped edges is given as

$$u = \frac{3}{16} \frac{p a^4}{t^3 E} (1 - \nu^2), \quad (5.6)$$

where u is the center deflection, p is the pressure drop across the disc, a is the radius of the disc, ν is Poisson's ratio, E is Young's modulus, and t is the thickness of the disc. The analytical expression is only accurate if $u < t$ and $t \ll d$. For the given membrane geometries numerical simulations indicate that the error is less than 20%, Table 5.1.

d [mm]	3.5	2.6	2.4	2.0
u_{sim} [μm]	134	44.5	35.7	16.9
u_{an} [μm]	127	38.7	28.1	13.6
deviation [%]	4.9	13	15	20

Table 5.1: Calculations of the membrane deflection u . Two methods are used: 1D axisymmetric finite element simulations in Femlab 3.1 and the analytical approximation from Eq. (5.6). Parameters: $p/E = 10^{-3}$, $t = 220 \mu\text{m}$, $\nu = 0.48$. The solved equations are linear, so $u \propto p/E$ for small deflections.

Material properties

The governing material parameters for the membrane deflection are the thickness t , Poisson's ratio and Young's modulus E . Young's modulus was indirectly measured by the

gravitational deflection of a beam clamped at only one end.

$$E = \frac{3}{2} \rho g \frac{l^4}{ut^2} \text{ for } t \ll l, \text{ and } u < t, \quad (5.7)$$

where $\rho = m_{\text{beam}}/(Ltb)$ is the density, g the gravitational acceleration, u the deflection, l the length of the freely suspended part of the beam, and t the thickness of the beam. A stage could be adjusted in the vertical direction with micrometer precision. The stage would start in a low position and then be gradually raised until it made contact with the tip of the beam. In some cases the beam would be attracted to the stage by static electricity. In those cases the deflection would be recorded when the tip of the beam was aligned with the edge of a spacer of known thickness. Membrane samples were cut by laser into beams of length $L = 30$ mm, width $b = 6$ mm and mass m_{beam} . The thickness t was measured by a micrometer screw gauge.

Silicone and latex have been used as membrane materials from (Medical silicones, Denmark) and (Ansell Medical, Germany). The membrane material has to be compatible with the bonding temperature. It was our experience that the latex membranes sometimes would get sticky after bonding which could increase the initial opening pressure. The silicone membranes did not show any signs of change. Several different silicone compounds were tested with Young's modulus ranging from $E = 1.6 - 11$ MPa and thicknesses $t = 220 - 470$ μm . Poisson's ratio is assumed to be $\nu = 0.48$ which is a common value for an elastic medium such as latex or silicone. In this paper, we present only two membrane types, namely latex, $t = 220$ μm , $E = 1.2$ MPa, and silicone $t = 220$ μm , $E = 3.1$ MPa.

Valve fabrication

A valve system consists of five 1 mm thick polymethylmethacrylate layers. Channels are made by laser ablation [28, 29] with a 65 W CO₂ laser. After laser machining and assembly the layers are aligned using pinholes and bonded in an oven at 108 °C for 90 min.

The middle layer accommodates four circular membranes, see Fig. 5.4. The membranes are sealed by a circular protruding rim (not visible) along the perimeter so that no liquid can bypass the membrane radially.

Using a custom-made cut tool slits in the membranes are made in the center of the membrane. The tool consists of a stainless steel knife blade, a holder and a cut template, see Fig. 5.5. The length of the slit is determined by the length of the blade. The blade comes from a Stanley hobby knife and measures 8 mm in length and 0.5 mm in width (away from the edge). The blade was then thinned down to a length of 1.8 mm resulting in a 1.5 mm slit for a $t = 220$ μm thick membrane. For optimum durability the blade was rounded at the edges to prevent the slit from expanding over time. The knife holder is fitted into a drill press to ensure a perfect vertical alignment. The tool does not remove any material and the slit is therefore extremely thin (or nonexistent) when the membrane is relaxed.

The geometry of the valve allows the slit to expand when pressure is applied in the positive direction of the valve. On the other hand, the slit is compressed when the pressure is in the negative direction of the valve.

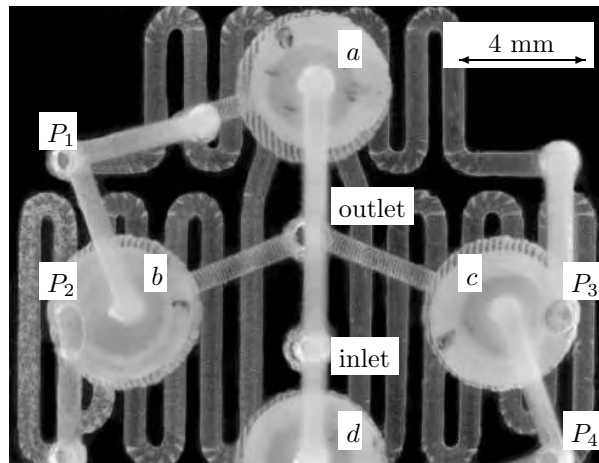


Figure 5.4: Picture of the valve system from above. The three dimensional system allows channels to cross in different levels. In the top level we have the access points P_2 and P_3 that connects to the EO actuator, see Fig. 5.1. In the bottom level we have the inlet and outlet of the pump. $a-d$ are the four circular rectifying membrane valves. When the flow enters a valve from above, it can pass through the slit in the membrane (not visible). Valve b and c are connected to the outlet and a and d to the inlet. In the bottom layer two meandering channels can be seen. They connect P_1 with P_2 and P_3 with P_4 , respectively. The functionality of this layer is described in Sec. 5.2.8.

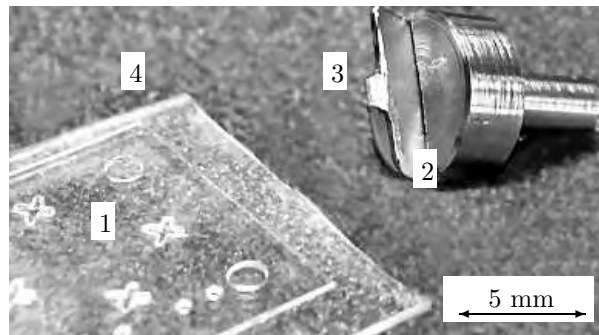


Figure 5.5: Tools for making precision cuts. (1) Template made in polymer by laser ablation. (2) Knife holder that fits into a drill press. (3) Blade thinned down to the appropriate length. (4) A soft cut plate is placed beneath the membrane to ensure that the cut tool penetrates the membrane.

Valve characterization

The Q - p characteristics of the valves were measured using an automated setup. During the measurements eight variables were sampled at 1 Hz into a data file using LabView with a 16-bit data acquisition card (National instruments, Austin, TX, USA). The variables are voltage ΔV , current I , upstream pressure p_1^{sens} , downstream pressure p_2^{sens} , mass m of liquid in the reservoir, valve state, pressure state and elapsed time. The valve and pressure state are used in the postprocessing of the data.

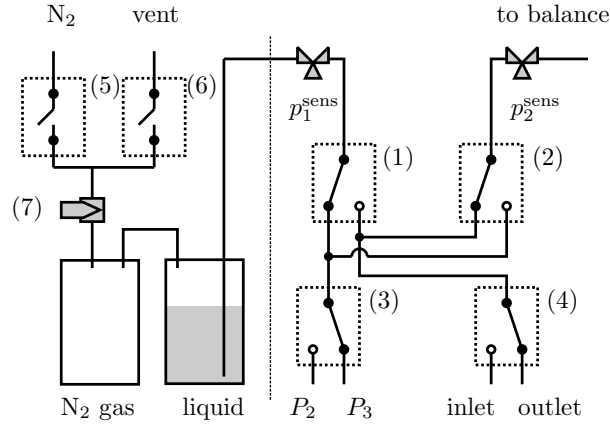


Figure 5.6: The flow can be diverted into the ports P_2 , P_3 , inlet, outlet by four 3-way valves (1-4). The position depicted is c open, $P_3 \rightarrow$ outlet. The flow is driven by pressurized liquid reservoirs. The N_2 pressure is controlled by two shut valves (5-6). The regulation speed can be adjusted by a needle valve with variable flow resistance (7).

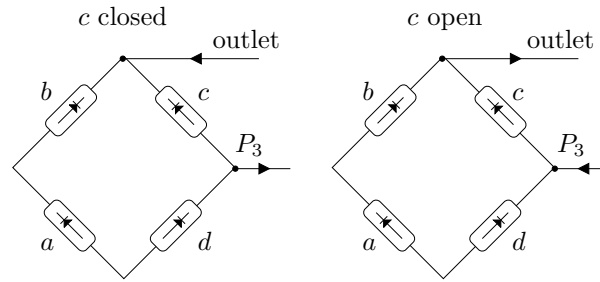


Figure 5.7: Examples of the two possible valve testing configurations for valve c . In the closed case the valve is tested in parallel to a combination of b closed, a closed and d open in series. In the open case open and close are interchanged. The meander is not included on this figure.

The flow switching and pressure regulation were programmed in LabView. A digitally controlled amplifier circuit was constructed to control the flow switching valves (1-4) and the pressure regulation valves (5-6). All electroactuated valves (1-6) are from Lee Company (Westbrook, CT, USA), see Fig. 5.6.

The pressure is increased when valve (5) is open and decreased when valve (6) is open. The valves are never open at the same time. The rate at which the pressure increases or decreases \dot{p} depends on the external N_2 pressure, the variable flow resistance (7) and the volume of the N_2 reservoir. The valve positions are only updated once per second so the pressure rate \dot{p} should be adjusted accordingly. If \dot{p} is too large the pressure will oscillate around the target pressure and if it is too small the regulation will be slow.

Each valve system has four individual valves denoted $a-d$, see Fig. 5.1. Each valve is tested in both directions at six different pressures $p_1^{\text{sens}} - p_2^{\text{sens}} = (0.05, 0.1, 0.15, 0.2, 0.25, 0.3)$ bar. This equals 48 measurements of Q and p for each valve chip.

The tests of the individual valves are not completely decoupled. When testing, e.g.,

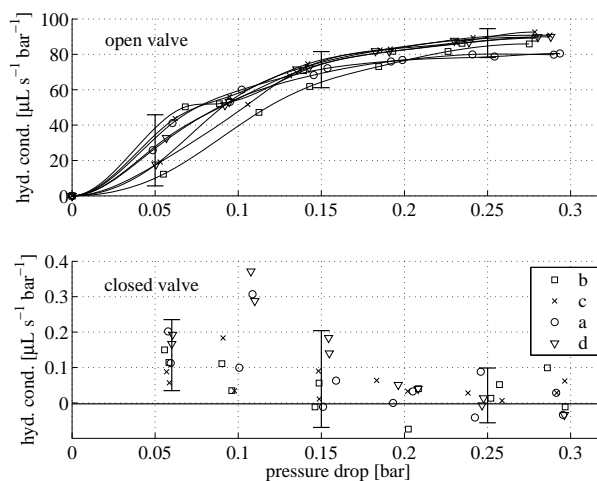


Figure 5.8: Q - p characteristic for four valves with $t = 220 \mu\text{m}$ latex membrane, 2.9 mm cavity, and 1.8 mm slits, $E = 1.2 \text{ MPa}$. Two identical experiments were conducted to test the reproducibility. The diodicity is in excess of 10^2 and the valves have very little resistance in the open mode. The negative flow measurements are due to noise on the balance readings. This particular valve system was used in all of the pumping experiments. The errorbars indicate the $\pm 2\sigma$ level for three selected pressure drops.

valve c open ($P_3 \rightarrow \text{outlet}$) we are actually measuring c open connected in parallel to a serial connection of d closed, a open and b open, see Fig. 5.7. At a given pressure each valve is tested for $T_{\text{meas}} = 70 \text{ s}$. The first five seconds worth of data is removed because the switching of the external valves may transmit a disturbing pulse to the balance. Corresponding values of flow rate Q and pressure p are average values over the period of a measurement.

A valve is defined open when the hydraulic conductance is 10% of the maximum value at 0.3 bar. The opening pressure is found at the intersection between the 10% level and the spline for the hydraulic conductance, see Fig. 5.8.

A series of experiments with different sized cavities were performed. The purpose was to see the effect of cavity size d on the opening pressure p_{open} , Fig. 5.9. It is seen that the opening pressure increases greatly with decreasing cavity diameter.

The opening pressure is seen to follow a $p_{\text{open}} \propto d^{-4}$ dependence. Combining this information with the deflection $u \propto d^4$ from Eq. (5.6) we conclude that the membrane deflection needed for valve opening is constant. Using the opening pressures from Fig. 5.9 we may calculate the deflection ratio u/t , see Table 5.2.

Additional valve tests indicated that the ratio $u/t = \text{const}$ is constant independent of the thickness t , cavity diameter d and Young's modulus E . Using Eq. (5.6) and $u/t = \text{const}$. Using this approximation we arrive at a simple scaling model for the opening pressure, $p_{\text{open}} \propto E (t/a)^4$. The scaling model states that smaller valves with similar opening pressures are possible as long as the ratio between the membrane thickness t and cavity radius a is kept constant. According to this scaling a miniature valve with a diameter of $2a = 1 \text{ mm}$, and membrane thickness of $t = (1 \text{ mm}/2.6 \text{ mm}) \times 220 \mu\text{m} = 85 \mu\text{m}$, and

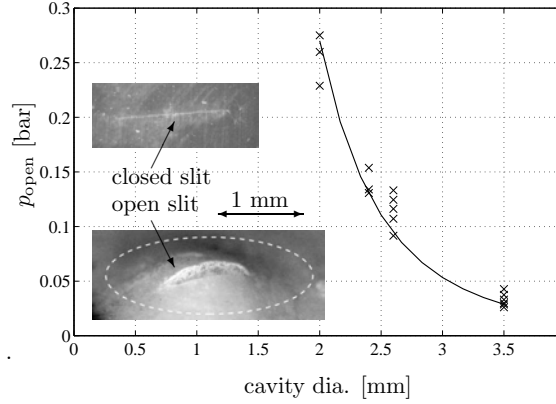


Figure 5.9: Opening pressure p_{open} vs. cavity diameter d . p_{open} is defined as the pressure where the hydraulic conductance is 10% of the maximum value (at 0.3 bar). The solid line is a polynomial fit $p_{\text{open}} \propto d^{-4}$. The insets show a relaxed membrane with a closed slit and a deflected membrane with an open slit. The dashed line is the perimeter of the membrane. Parameters: silicone valve system $t = 220 \mu\text{m}$, $E = 3.1 \text{ MPa}$

cav. dia. mm	mean u/t	std. dev. u/t
2.0	0.61	0.07
2.4	0.66	0.07
2.6	0.72	0.09
3.5	0.63	0.11

Table 5.2: The deflection ratio u/t vs. cavity diameter. The results indicate that for a given membrane thickness t there exists a $u/t \approx 0.7$ ratio where the valve opens. The mean values are all within the standard deviations. Parameters: $t = 220 \mu\text{m}$, $E = 3.1 \text{ MPa}$, silicone, Slit: 1.8 mm.

an opening pressure of $p_{\text{open}} = 0.1 \text{ bar}$ should be possible.

5.2.6 Integration issues

The integration of the different pump components is very important. The pump is constructed in modules that can be separated. In this section we describe some of the integration issues. Some of these issue are trivial while others are more advanced. The integrated pump are shown in Fig. 5.10.

Leaks

The pump is constructed in layered modules. Some of the layers are thermally bonded while others are mechanically compressed to form a seal. Cavities within the polymer layers or gaskets may give rise to a nonuniform compression with resulting leaks. This

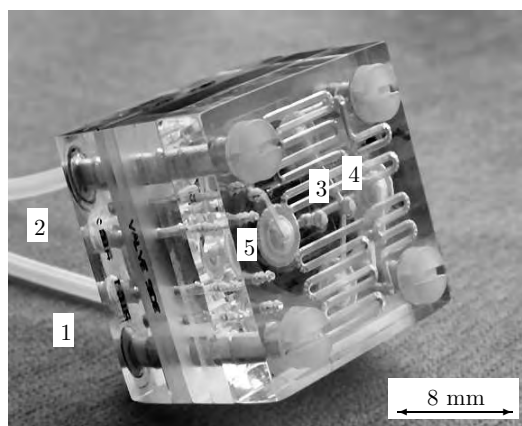


Figure 5.10: Picture of the assembled pump. Tubes (1) and (2) connect to the EO actuator via P_2 and P_3 , respectively. These external connections are only used for priming of the pump and are sealed of during operation. The inlet and outlet of the pump are marked (3) and (4), respectively (no tubes are attached for better visibility). (5) The valve system is seen from the opposite side compared to Fig. 5.4.

effect is non trivial and has to be considered when designing the flow system. More trivial causes for leaks or unintended cross flow are poor bonding or loose external tubing.

Sealing

The pump is held together by four custom fabricated polycarbonate M2×20 mm bolts. Initially stainless steel bolts were used because of their good mechanical properties. However, it was found that the bolts made electrical contact with the buffer through the ion exchange membranes. Voltage differences in excess of 2 V existed between the bolts. This was unacceptable because it meant that there were stray currents, hence the need for non-conducting bolts. The polycarbonate bolts are much weaker mechanically but still strong enough to give the necessary compression.

Internal flushing system

Thermally bonded parts are thoroughly tested for functionality after bonding. This is necessary because bonded channels can be deformed if the bonding pressure or temperature were too high. Aligning of interconnections between layers is also critical. If holes are misaligned no fluid can pass.

In the actuator some of the channels are defined by the gasket layers. This type of design can give problems because of the flexible nature of the gaskets. Hence, the channel dimensions depend on the compression of the layers at assembly. Sometimes the channels would be completely blocked. To some degree this was solved by minimizing the amount of gasket defined channels.

After assembly the hydraulic resistance of the internal flushing system is evaluated. This value should be low in order not to give any considerable internal pressure drop

during operating.

Compliance

The actuator and the valve system specifications have to match in order for the pump to function properly. A very important integration issue is the compliance K which is defined as the derivative of the volume with respect to the pressure p .

In the DC case the compliance affects the response time of the pump but in the AC case it affects the Q - p characteristics. The main contribution to the compliance comes from the freely suspended ion exchange membranes. The frit support was changed from a relatively coarse polymer mesh (1 mm) to a fine frit (10-16 μm). By grinding the surface of the frit support a completely smooth support was obtained. However, the membrane itself has a clearance of 90 μm to each side because of the gaskets. In the worst case scenario this would yield a variable volume of $5 \times 5 \times 0.18 \text{ mm}^3 = 4.5 \mu\text{L}$. Inserting a 180 μm thick glass fibre plate reduces the clearance of the ion exchange membrane to a minimum. A typical value for the compliance is $K = 2 \mu\text{L bar}^{-1}$ for each frit compartment.

In the valve chip the flexible membranes can increase the compliance as well. Especially the the cavity design is important. If the cavity is shaped as a cylinder it is very likely that air bubbles will be trapped along the perimeter of the cavity. A conical shaped cavity reduces the risk of this happening. Optimally, the cavity is shaped to match the deflection leaving almost no dead volume when the valve is fully open.

Electrical contact

The electrical resistance of the pump should be reproducible for a given buffer concentration. In order to achieve this the pump must be constructed such that it is possible to fill the electrode reservoirs and internal chambers the same way each time. Trapped air may change the electrical resistance. Using a glass frit as membrane support has a second advantage. Because of the hydrophilic nature of the porous glass a good electrical contact is easily made between the electrode chamber and the ion exchange membrane.

5.2.7 Pump characteristics

The applied voltage was controlled from LabView through a data acquisition card. The output voltage from the data acquisition card was in the range $\pm 10 \text{ V}$. By connecting this output to a 3-fold amplifier the desired voltage range could be obtained. In all experiments a square wave $V = \pm 30 \text{ V}$ was applied. The setup shown in Fig. 5.6 was modified to accommodate the pump between the two pressure sensors, p_1^{sens} and p_2^{sens} instead of the switching valves (1-4).

Flow rate and pressure characteristics

The first test is to measure the free flow rate, i.e., no backpressure applied. In this case the flow rate should be stable over time. The pump is operated for two hours without any noticeable change in performance, see Fig. 5.11(a). The flow rate is calculated by

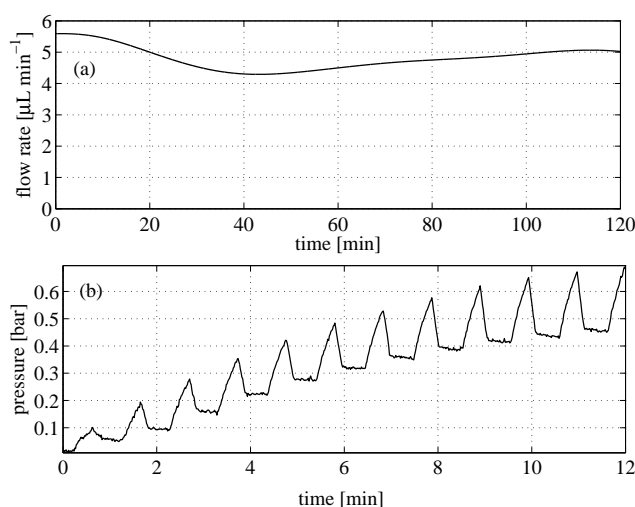


Figure 5.11: (a) Average free flow rate Q versus time. The flow rate is found as the derivative of a spline fitted to the volume vs. time data. The peaks from individual strokes are averaged out by the spline. Parameters: period $T = 40$ s, buffer 20 mM borax, voltage ± 30 V, latex valve system, $t = 220$ μm , $E = 1.2$ MPa, $d = 2.6$ mm. (b) Backpressure p versus time, when the outlet of the pump is blocked. The plot shows the gradual pressure buildup. There is a small amount of compliance in the pressure sensor. Parameters: same as panel except the period which is now $T = 60$ s.

differentiating the spline fitted to the volume versus time data. The flow rate varies 0.5 $\mu\text{L min}^{-1}$ around the mean value of $Q = 5$ $\mu\text{L min}^{-1}$. The actuator should supply a flow rate of $Q = 12$ $\mu\text{L min}^{-1}$. The reason for this discrepancy is the compliance and the efficiency of the valve system.

The pressure capacity of the pump is measured by blocking the outlet, see Fig. 5.11(b). The pressure builds up gradually. Apparently, only one of the stroke directions contributes to the pressure buildup. This is seen by the plateau in between the peaks. The reason could be that the compliance is different on different sides of the frit. The immediate relaxation in pressure right after the peak is probably because the valve membrane returns to its closed position. The backflow resulting from membrane movement is roughly $V_{\text{back}} = 0.5$ μL . The terminal pressure is approximately $\Delta p = 0.5$ bar, which is quite low compared to the expected actuator pressure of $\Delta p = 10$ bar. The largest pressure measured with a valve system was $\Delta p = 2$ bar.

Flow rate dependence on stroke period

The flow rate depends on the stroke period. Two mechanisms are important. Due to ion depletion near the ion exchange membranes the current and hence the flow rate drops over time. The average flow rate of the actuator is therefore larger for a short stroke period than for a long stroke period.

If the pump is operated with a small stroke volume it is more susceptible to flow reduction because of compliance than if operated with a large stroke volume. On the

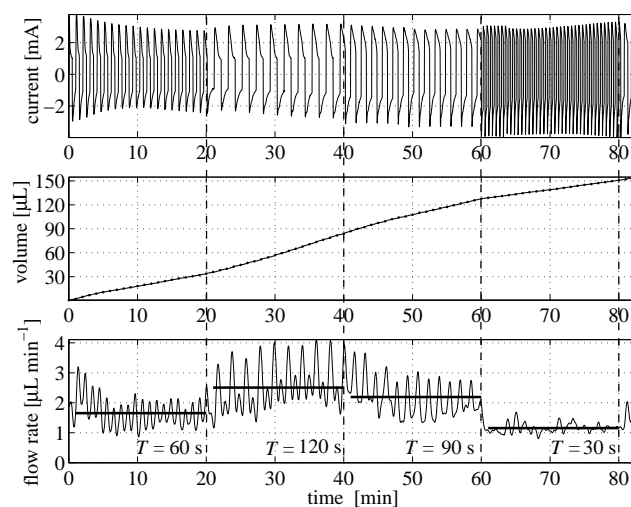


Figure 5.12: Current I , volume V , and flow rate Q versus time. The period T is varied over time: 0-20 min $T = 60$ s, 20-40 min $T = 120$ s, 40-60 min $T = 90$ s, 60-80 min $T = 30$ s. The horizontal solid lines indicate the average flow rate for each period. The flow rate Q is seen to increase with the length of the period T . Parameters: buffer 20 mM borax, voltage ± 30 V, latex valve system, $t = 220$ μm , $d = 2.6$ mm.

other hand a pump operated with a very long period may have unnecessary low flow rate because of ion depletion. The optimum period depends on the compliance and on the stroke volume. In Fig. 5.12 the flow rate Q is measured for different stroke periods.

From Fig. 5.12 it is seen that the flow rate increases with increasing stroke period. The stroke volumes were measured after the experiment by removing the valve chip and connecting each port P_2 and P_3 to a half filled measurement tube. The stroke volumes could then be measured by observing the moving interface in the respective tubes. In a tube with an inner diameter of $2a = 0.5$ mm there is $V_{\text{tube}} = 0.196$ $\mu\text{L mm}^{-1}$. The results were $V_{15\text{ s}} = 0.30$ μL , $V_{30\text{ s}} = 0.95$ μL , $V_{45\text{ s}} = 1.6$ μL , $V_{60\text{ s}} = 1.9$ μL . The compliance was measured by applying 1 bar of excess pressure to a measurement tube and observing how far the interface moved. The compliances on each side of the frit were measured to $K_1 = 1.5$ $\mu\text{L bar}^{-1}$ and $K_2 = 1.8$ $\mu\text{L bar}^{-1}$, respectively. The low ratio between the stroke volume and compliance implies that the pump will not be able to produce any significant pressure compared to the pressure capacity of the actuator.

Flow rate and current

In the actuator the flow rate and current are almost in phase. However, when coupled to nonlinear components such as the valve system a phase lag between the flow rate of the AC EO pump and the current is introduced, see Fig. 5.13.

The difference in flow rate in the two stroke directions indicates that there is an asymmetry in either the actuator or the valve system. We also note that the peak currents are slightly different when positive and negative voltages are applied. Such asymmetries

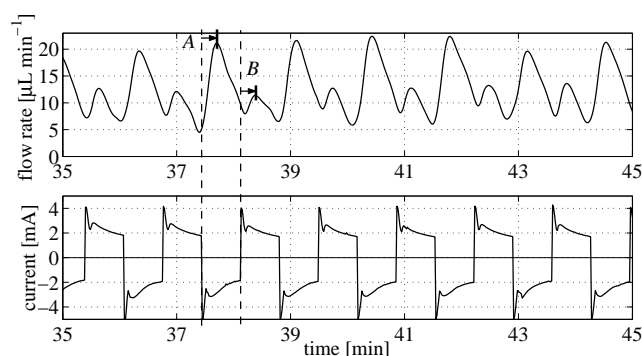


Figure 5.13: Flow rate Q and current I versus time. At position A the flow has switched from positive to negative. It takes approximately 10 s for the flow rate to respond. Then the flow rate decreases again because of the decrease in current. At position B the same thing happens with smaller amplitude. Parameters: period $T = 80$ s, buffer 20 mM borax, voltage ± 30 V, latex valve system, $t = 220$ μm , $d = 2.6$ mm.

in flow and current have been observed in almost all of the experiments.

In this case, the average flow rate is close to the predicted value of $Q = 12$ $\mu\text{L min}^{-1}$, which means that the valve system and actuator are performing well in spite of the asymmetry.

5.2.8 Outlook

Future work involves the development of a system capable of separating the buffer in the actuator from the externally pumped liquid, e.g., by using oil plugs. Such a system would render the pump independent of the external liquid and hereby improve on the design idea in Ref. [13] where EO induced viscous drag in a two liquid system was used as the pumping mechanism. The present design already has a separator system consisting of two meanders with side channels enabling precise positioning of separator plugs, see Figs. 5.4 and 5.10. The separator plug should stay in the meander during operation. This implies that the problems with flow drift (asymmetry in stroke volumes) and compliance must be resolved before such a system could work satisfactorily.

5.2.9 Conclusion

We have presented a novel AC electroosmotic pump with rectifying membrane valves. The pump is almost maintenance-free because of the bubble-free palladium electrodes.

The conditions for bubble-free operation of palladium electrodes have been analyzed numerically and experimentally. A simple diffusion model was found to give an adequate description of the bubble formation mechanism.

A full-wave rectifying valve system has been designed and tested successfully. The parameters governing the valve characteristics have been investigated and design guidelines have been proposed to aid in further miniaturization of the promising membrane valve concept.

The AC EO pump is more versatile than the previous DC EO pump because it is also capable of pumping buffered solutions with particles as these only have to pass the valves and not through the nanoporous frit. Because of the possibility to pump all types of liquids in a precise and controlled manner, the described concept and design bears great promise.

Acknowledgements

We would like to acknowledge Torben Jacobsen for helpful discussions on electrochemistry. This work is partly supported by the Danish Technical Research Council, μ TAS Frame Program Grant No. 26-00-0220.

_____ end of paper _____

Chapter 6

Additional material for the AC EO pump

The work with bubble-free palladium electrodes was inspired by conversations with Assoc. Prof. Torben Jacobsen from the Department of Chemistry at DTU. The initial experiments were conducted at his laboratory. However, the main experiments and modelling were done by me during my stay at University of Michigan.

Prior to the membrane slit valve design presented in Chap. 5 a lot of different materials and valve geometries were tested. A simple setup for measuring the Young's modulus was constructed because the available stress and strain equipment could not handle the small sample sizes.

An automated valve testing setup was constructed because of the large number of measurements needed. The setup worked very well and has now been modified to become a permanent setup at MIC, DTU for measuring hydraulic resistance, see Fig. B.3. Some important aspects about measuring pressure are also presented in this chapter.

The AC electroosmotic pump with rectifying polymer membrane valves features a rather complex internal flow system. A simple 2D version of computer aided design (CAD) software was used to reduce the development time. A brief discussion of some of the design issues is given in this section.

Fabrication of the pump involves aligning and bonding of layers. Hence some practical details are given about bonding, alignment and fittings.

6.1 Bubble-free electrodes

An essential part of the EO actuator is the bubble-free electrodes. In this section we discuss the physics and mathematical modelling of the diffusion process.

Hydrogen is introduced into the Pd phase through cathodic processes in aqueous media. Hydrogen partially fills the octahedral holes in the Pd crystal to form PdH_x . Although hydrogen atoms occupy only interstitial sites, the sublattice of metal atoms in PdH_x is larger than the parent lattice. The PdH_x lattice therefore undergoes expansion or contraction as the Pd/H ratio changes, [42].

A H/Pd ratio of 0.57 is reported giving a lattice constant of 4.04 Å compared to the normal 3.89 Å. The differences in lattice constants from varying H/Pd ratios yields stresses in the material which can lead to microcracking. Using the values for density and atomic weight we can estimate the maximum concentration of hydrogen to be stored.

$$\rho_{\text{vol,Pd}} = 12.02 \text{ kg/L} \quad (6.1)$$

$$\rho_{\text{mol,Pd}} = 0.106 \text{ kg/mol} \quad (6.2)$$

$$c_{\text{Pd}} = \frac{\rho_{\text{mol}}}{\rho_{\text{vol}}} = 113 \text{ mol/L} \quad (6.3)$$

$$c_{\text{H}} = 0.57 c_{\text{Pd}} = 64 \text{ mol/L} \quad (6.4)$$

Numerically the surface concentration $c(r = a)$ is calculated as a function of current density i and time t using a diffusion model. Diffusion characterized by the diffusion constant D_{H} is the governing transport process once the hydrogen is in the Pd phase. The electrodes are made of thin palladium wires with radius a . The geometry is therefore cylindrical with no variation in the longitudinal direction. The model is a one dimensional linear diffusion equation with inhomogeneous Neumann boundary conditions, Eqs 6.7.

$$\frac{\partial c}{\partial t} - \frac{1}{r} \frac{\partial}{\partial r} \left(r D_{\text{H}} \frac{\partial c}{\partial r} \right) = 0 \quad (6.5)$$

$$D_{\text{H}} \frac{\partial c}{\partial r} \Big|_{r=0} = 0 \quad (6.6)$$

$$D_{\text{H}} \frac{\partial c}{\partial r} \Big|_{r=a} = \frac{i}{F} \quad (6.7)$$

where i is the current flux, F the Faradaic constant, c the concentration of H in Pd. The equations are made dimensionless and solved numerically in MATLAB. The results were plotted in Fig. 5.2. The above boundary conditions represent a simplified model. In reality some of the hydrogen generated at the surface may diffuse into the solution rather than into the electrode. The surface reaction rate will also most likely be nonuniform due to the electrode geometry. The sides facing away from the opposing electrode will face a smaller current density. The model assumes a uniform current density.

6.2 Valve and membrane material testing

The flow characteristics of a membrane valve are highly dependent on the membrane material and dimensions. Hence, a lot of different materials were tested. The PMMA valve system is bonded together at $T_b = 109 \text{ }^\circ\text{C}$ which is slightly above the glass transition temperature $T_g \approx 105 \text{ }^\circ\text{C}$ for PMMA. It was found that many polymer membranes would deform plastically at that temperature. However, silicone has a high melting point of $T_m \approx 200 \text{ }^\circ\text{C}$ and is therefore suited for this application. Furthermore, it has a good shape memory, i.e., it recovers its original form after a deformation. The silicone membranes are laser cut from a plate. The laser burns the silicone and therefore leaves ashes on the surface. The ash can easily be removed by rinsing with water. Latex also worked well as a membrane material in some cases. However, problems with sticky surfaces could result

in large opening pressures. The surface would become sticky after heat exposure either from the laser cutting or bonding. Another problem with the latex membranes was water absorption which makes the membranes swell. The swelling can cause the membrane to be permanently deflected and hereby leak. The advantage of a latex membrane is that it is very soft and therefore seals and deflects very well.

label	t μm	ρ kg m^{-3}	E MPa
silicone 1	270/320/340	1071	1.6
silicone 3	190/210/220	1108	3.1
silicone 5	270/250/220	1175	11
silicone 6	470/450/430	1130	7.2
silicone 15	300/310/330	1144	7.9
latex	220	-	1.2

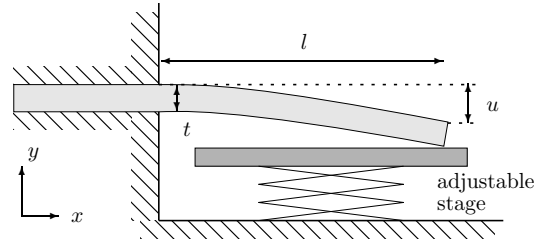


Figure 6.1: (table) Measurement of Young's modulus for different types of membrane material. Young's modulus of the silicone qualities are varied by compound mixing ratios and the clamp moulding pressure. The thickness t is measured at three different positions. The density ρ is based on an average thickness whereas the bending is based on the middle thickness. (figure) The deflection u_d was measured using an adjustable stage.

Additional valve tests indicated that u_d and t depend linearly on each other independent on cavity diameter d and Young's modulus E , see Fig. 6.2. In total more than 21 valve systems were characterized. Using Eq. (5.6) and the approximation $u/t = \text{const}$ we arrive at a simple scaling model for the opening pressure, $p_{\text{open}} \propto E (t/a)^4$. Further work is needed to verify this relation. Very precise measurements of the cavity diameter, and the membrane thickness are needed because these parameters enter the equations in powers of 4 and 2, respectively. For very thin membranes it may also prove difficult to make a perfect slit due to the finite width of the knife blade.

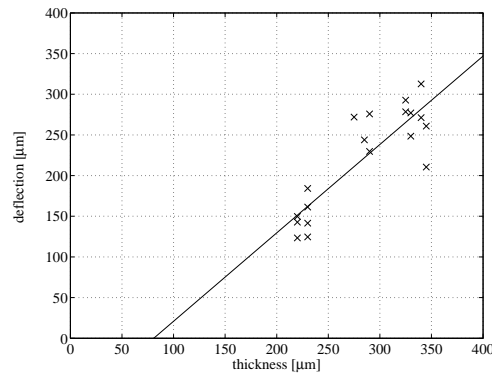


Figure 6.2: Membrane deflection u_d at the valve opening pressure vs. membrane thickness t . The solid line is a linear fit with slope 1.1. The opening pressure is defined as the pressure where the hydraulic conductivity is 10% of the value at $\Delta p = 0.3$ bar. Parameters: silicone valve system.

6.3 Automated valve testing setup

The valve testing was automated because of the large number of measurements needed. The testing setup consists of two valve systems. One for setting the correct pressure across the valve and one for directing the flow to the correct ports. In order to obtain fast and accurate pressure measurements in a microfluidic system it is important to reduce the compliance. Flow resistance times compliance gives a characteristic time. In a compliant system with large flow resistance this time scale may be several minutes or even hours. As a rule of thumb the pressure measurements will have transients of the same order. It is, however, highly dependent on how the specific system is constructed. A large part of the compliance is typically introduced through the coupling of the pressure sensor. In the present work silicon membrane-based pressure sensors from Honeywell have been used, see Fig. 6.3(a)

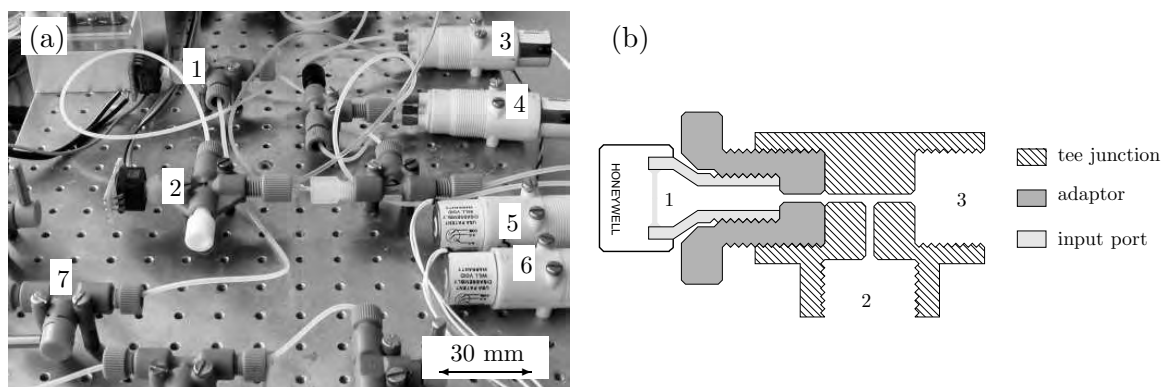


Figure 6.3: (a) (1) and (2) Honeywell pressure sensors mounted in a tee and cross junction respectively, (3-6) 3-way solenoid valves (7) manual shut valve. (b) The pressure sensors input port is mounted in an adaptor that again fits into the receiving tee junction. The interior of the pressure sensor can be filled by inserting a thin capillary from port (3) towards (1) the membrane while being careful not to exert any significant force against the fragile membrane. The swept volume will only be the volume between port (2) and (3).

The pressure sensor comes with a tapered stainless steel input port designed for connecting to a large bore flexible, e.g. silicone, tubing. It is not recommended to use this standard fitting for microfluidic systems since it will introduce a significant amount of compliance to the system.

The alternative is to make a male thread on the input port. The port can then fit into an adaptor, e.g. female M3 to male 1/4"-28. Standard teflon tape should be used to ensure a tight connection between the input port and the adaptor. The sensor can then be attached to an appropriate female fitting with a minimal dead volume as a result. In order to decrease the compliance even further it is recommended to fill up the interior of the pressure sensor by attaching a capillary to a syringe. The dead volume of the pressure sensor can be as high as $\mathcal{V}_{\text{dead}} \approx 100 \mu\text{L}$ depending on the model but if properly prepared the compliance is very low $K < 1 \mu\text{L bar}^{-1}$ instead of $K \approx 50 \mu\text{L bar}^{-1}$ or worse. For comparison the swept volume of an Upchurch tee junction ID = 0.5 mm is $\mathcal{V}_{\text{swept}} = 2.9 \mu\text{L}$.

6.4 The reservoir and separator module

The reservoir module seen in Fig. 6.4(a) has several functions. The reservoir chamber holds an electrode. The power lead (1) is inserted through the channel and a Pd wire soldered onto it. The Pd wire can be softened by annealing it with a hot flame. After that it is straightforward to shape it. The soldering tin is sealed off from the reservoir by epoxy. This is an important step because the soldering tin can react with the buffer and hereby contaminate the solution.

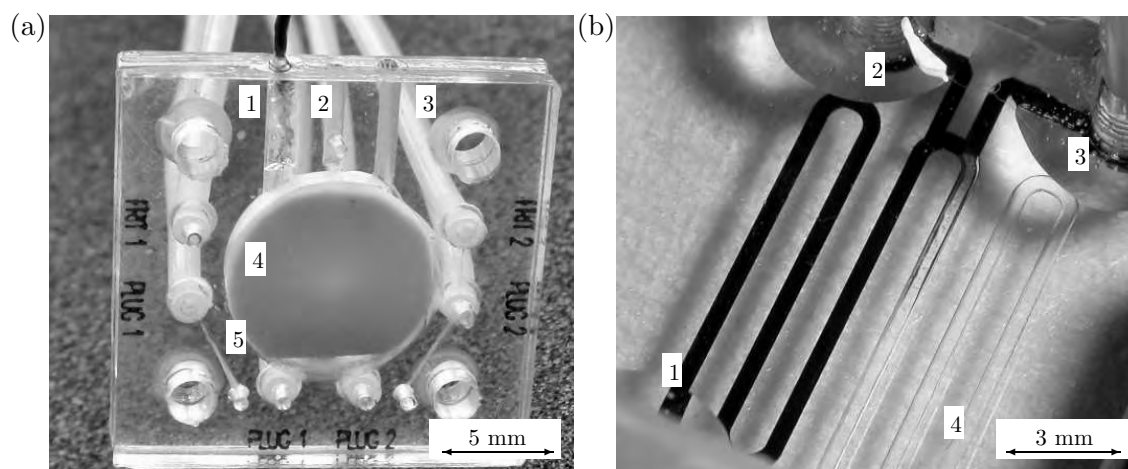


Figure 6.4: (a) Picture of the reservoir module. (1) Power lead sealed with epoxy (2) vent channel (3) reservoir filling channel (4) support frit 10-16 μm pore size (5) bypass channel. (b) Picture of a test separator system. The channel is milled with a cross section of $400 \times 400 \mu\text{m}^2$. (1) Inlet (2) plug inlet, (3) plug outlet and (4) outlet.

The reservoir chamber is filled with buffer by inserting a thin needle through (3) the reservoir filling channel. The needle fills the reservoir from the bottom and up. The trapped air escapes through (2) the vent channel. The reservoir module also serves as support for the ion exchange membrane. (4) The support frit is polished into a smooth transition between polymer and frit. (5) The extra bypass channels are necessary in order to make room for the six fittings. There is one tube for each frit compartment, e.g., *frit 1* and *frit 2*. Inserting an oil plug in the two separators requires additional two times two tubes. In total this gives a staggering number of eight external connections, where six of them are for service purposes only.

In a future version of the pump the six service tube fittings should be replaced with hex socket set screws. In this way the service channels could be accessed with a simple hex key. Replacing the liquid within the inner loop could be done by loosening the *frit 1* and *frit 2* ports and apply pressure to the inlet while blocking the outlet. Similarly, oil plugs could be injected only by using a syringe and a hex key.

As mentioned in Sec. 5.2.8 a separator system can make the AC EO pump independent on the pumped liquid. In Fig. 6.4(b) a test separator system is depicted. In analogy with

a reciprocating pump; the meander structure is the displacement chamber while the oil plug is the moving boundary that exerts a force on the pumped liquid. In this way mixing of the liquids is avoided.

Injecting of an oil plug into the system is done by applying oil between ports (2) and (3) while keeping (1) and (4) closed. Once the oil plug is injected (2) and (3) are closed again. The channel is made of PMMA which is slightly hydrophilic. Ideally, the oil plug should have a contact angle of 90° with the PMMA and the buffer. If the contact angle is too low the oil plug may wet the surface which actually can be seen in the figure. It was found that the magnetic oil suspension from the figure mixed with paraffin oil in the ratio 1:10 worked fine. The channel walls should be as smooth as possible in order not to breakup the oil plug. Laser machined channels were too coarse. Therefore, this part of the fabrication had to be done with the micromilling machine. The test separator system was tested with the EO actuator. The Achilles heel of this system would be drifting of the plugs. There is no mechanism that prevents the plugs from leaving the separator. Small asymmetries could accumulate over time and thereby evacuate the plugs from the system. The system was not tested in the integrated version due to lack of time and problems with the stability of the EO actuator.

6.5 Design and fabrication

This section describes some of the design issues when fabricating multilayered polymer structures. In a multilayered structure alignment is very important. Design software can be used to visualize the complex structures.

6.5.1 Computer aided design

The many layers in the pump were designed in the 2D vector drawing program COREL DRAW 9.0. The drawing software was used in the initial design phase in order to make the pump as compact and simple as possible, i.e., reduce the number of layers. The 3D nature of the channel routing makes it challenging to use 2D computer aided design (CAD) but the machining of the part is also done in 2D (with depth control). The design can therefore be relatively easily exported to the software in the milling or laser machine. One complication to the design process is that the layers can only be machined from one side. Otherwise a setup for aligning would be necessary. The single side processing requires that some of the layers are mirrored. This complication combined with the large number of layers (16 or more) made it useful to label them. The labelling also assisted in the assembly process, see Fig. 6.4. Labels such as *frit 1*, were marked by laser and colored with a black marker. The color in the plane was then removed by a scalpel so that only the color in the letters remained. The layers were then bonded and the label would be permanent.

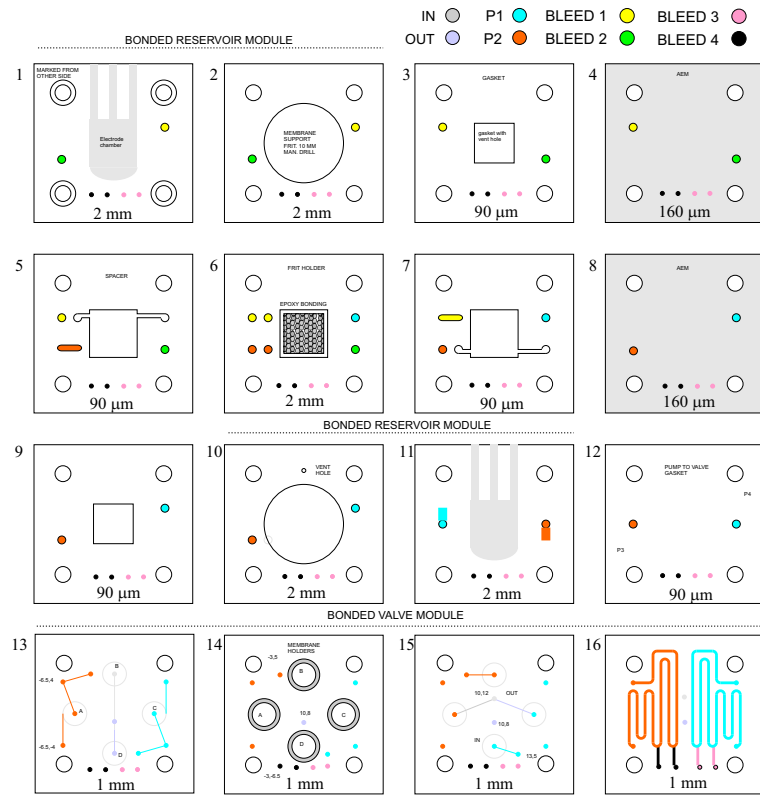


Figure 6.5: Drawing of the pump components. A 2D drawing software was used as a design tool to check the alignment of the through holes etc. The presented design is representative but not an accurate description of the final pump design. The thickness and sequence of the layers are indicated.

6.5.2 Fabrication of the layers

The pump consists of multiple layers. The rigid layers are structured from PMMA plates with the following thicknesses (0.250, 1, 1.5, 2) mm. Depending on the function of the layer different thicknesses would be used. The modules facing the exterior of the pump should be more than 3 mm thick to ensure uniform compression and thereby avoid leaks.

Most of the fabrication was done with the CO₂ laser. The line width of the laser beam is approximately 200 μm. A precision milling machine is however, in many aspects, superior to the laser system. The laser is very fast and it is easy to setup a design, but the channels it generates have sloped walls and the ablation process deposits material outside the channel. The milling machine is very slow in contrast to the laser and requires more planning but the finishing quality is typically much better. In a large volume production all the parts would be injection molded.

6.5.3 Bonding and alignment

Some of the layers in the pump are adjoined by thermal bonding. Structures with multiple layers and functionality are denoted modules. This section describes the bonding process.

Prior to bonding the layers must be cleaned. This is done by rinsing them in deionized water. Cleaning with alcohol can cause the chip to crack due to the stress induced by the laser machining. Milled structures do not have this built-in stress. After cleaning the layers are dried with nitrogen or a cleanroom wipe. The layers are then placed on a glass plate to prevent imprinting from the rough surfaces, see Fig. 6.6(a). The alignment of the layers is done by placing two or more pins in the corner through holes. The through holes were marked with the laser and subsequently mechanically drilled 0.1 mm larger than the pin. The precision of this type of alignment is therefore within 200 μm . The pins should be shorter than the total thickness of the layers to ensure clearance between the pins and the glass plates. In this way a lot of pins with different lengths are needed but it is still the preferred method of alignment since it is reliable and easy to use.

The aluminum blocks are then put together with care and compressed using a clamp, see Fig. 6.6(b). The clamp force should be adjusted to achieve a reasonable bonding pressure. This method is largely based on experience. The yield is typically 50% or better. Usually two chips were bonded simultaneously. This stabilizes the blocks and saves time.

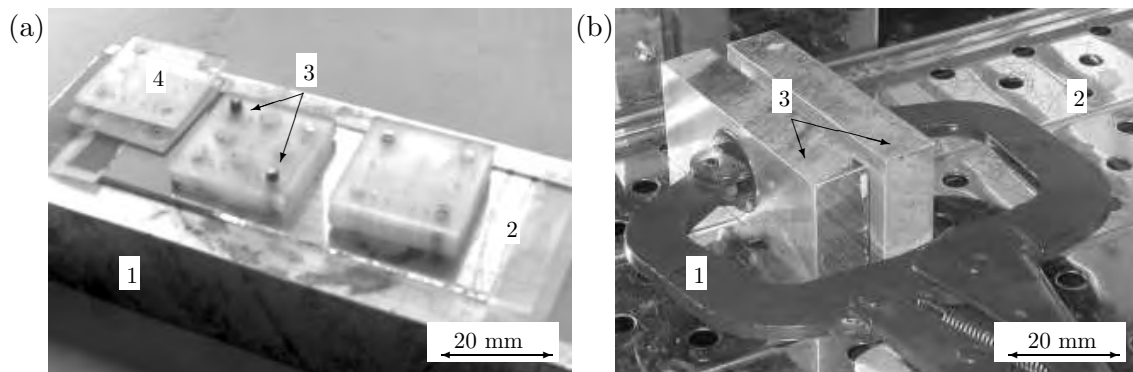


Figure 6.6: (a) Picture of alignment setup. (1) The aluminium block (2) the glass plate (3) two pins inserted in corner through holes (4) additional layers (b) Picture of the clamped blocks. (1) clamp, (2) oven plate and (3) the two aluminium blocks.

The clamped layers are then inserted into the preheated oven and bonded at $T_b = 109\text{ }^\circ\text{C}$ for 90 min. Multiple layers can be bonded simultaneously. Another type of alignment was also used. A very simple but effective method is to attach a strip of adhesive tape in each corner of the chip. Again, the strips should be of appropriate width and length in order not to interfere with the glass plate.

The manufacturers of PMMA add their own secret additives to the polymer in order to improve some properties. Various manufacturers therefore have different PMMA qualities. This gave some problems because the different PMMA qualities performed differently in terms of laser ablation and bonding.

Chapter 7

AC EO pump with mobile plug valves

The following work was carried out during my five month external stay at University of Michigan, Ann Arbor, MI, USA in the spring of 2004. Assist. Prof. Ernest F. Hasselbrink (Charlie) was my daily supervisor in that period. A fellow PhD student Meng-Ping Chang did the cleanroom part of the valve fabrication.

The idea was to construct an AC EO pump with a flow rectifying system based on the mobile polymer plug valve concept. This work was done prior to that described in Chaps. 5 and 6. Assist. Prof. Hasselbrink had previously worked with the mobile polymer plug valves at Sandia National Laboratory, Livermore, CA, USA. The EO actuator and valve system were not integrated in these preliminary tests. It proved to be very difficult to reproduce the published data from Hasselbrink *et al.*, [35] and a lot of adjustments in the fabrication method and polymer recipes were needed.

7.1 General

The pump consists of a microvalve system and an EO actuator, Fig. 7.1(a). The purpose of the microvalve system is to rectify the oscillating flow from the EO actuator. The pumping scheme is therefore identical to the one described in Chap. 5, however, both the EO actuator and the valve system differ considerably. The major challenge was to fabricate a working valve system. Hence most of the focus was concentrated on that part of the project.

7.2 EO Actuator with bubble-free electrodes

The actuator consists of a porous frit encapsulated within a thick PMMA casing. Electrodes made of palladium are placed adjacent to the frit surface. The spacing is needed to ensure a uniform electrical field and prevent any obvious nucleation sites for bubble formation, see Fig. 7.1(a).

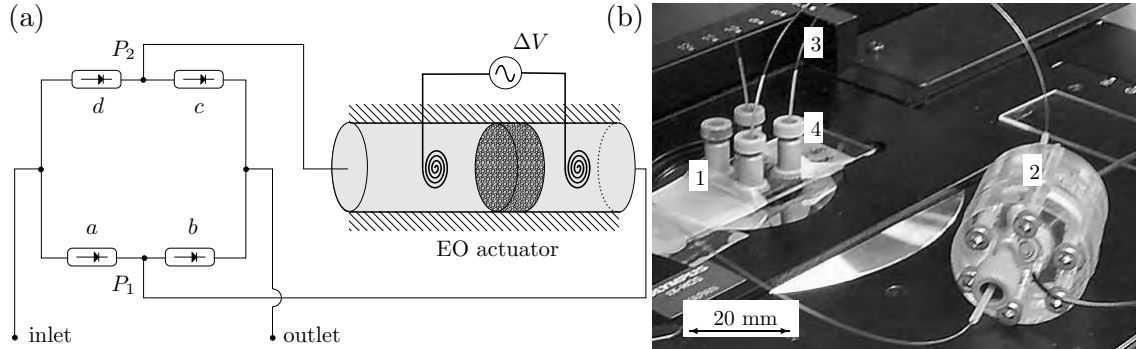


Figure 7.1: (a) Flow diagram of the frit-based EO pump together with 4-way microvalve system. The valves are labelled $a - d$. The electrodes are enclosed because they are bubble-free. (b) Picture of (2) the EO actuator coupled to a (1) two-valve system using high-bore (ID = $250 \mu\text{m}$) (3) capillaries. The capillaries are connected to the valve chip using (4) Upchurch nanoports.

The frit is made of 99.99% silica with a pore size of $2a = 200 \text{ nm}$. It is 10 mm in diameter and 4 mm thick and positioned between the two chambers with bubble-free palladium electrodes. The electrodes are made of a 50 mm long wire with a diameter of 0.3 mm. The fluidic connections between the EO actuator and the valve system are made using high-bore capillaries in order to avoid any significant pressure drops, see Fig. 7.1(b). A flow rate $Q = 30 \mu\text{L min}^{-1}$ through 1 m of tubing with ID = $250 \mu\text{m}$ only gives a pressure drop of $\Delta p = 0.05 \text{ bar}$. The voltage applied to the EO actuator is a square wave generated by a LABVIEW controlled trigger relay coupled to a DC power supply. The flow rate generated by the EO actuator is found by measuring the stroke length of the liquid air interface in a capillary. At 10 V it gives $Q = 17 \mu\text{L min}^{-1}$. The hydraulic conductance of the frit is measured to be $R_{\text{hyd}}^{-1} = 0.73 \mu\text{L} (\text{min bar})^{-1}$.

The bubble-free palladium electrodes used are similar to those described in Chap. 5. In this case the electrodes are embedded in the design and it is therefore more critical that they operate completely bubble-free, see Fig. 7.1. Gas formed at the electrodes significantly decreases the pump performance due to the added compliance, see also Appendix A.

7.3 Valve system

The valve principle relies on a moving plug made of polymer, see Fig. 7.2(a). In the open mode the flow can bypass the plug through the bypass channel. If the flow then changes direction the plug will experience a pressure force due to the pressure drop across the bypass channel. If sufficient this force will drive the plug to the opposite valve seat and thereby close the valve.

The experiments from Ref. [35] resulted in a simple relation between opening pressure and static friction. $P_{\text{open}} A_{\text{cross}} = c_f A_{\text{surf}}$, see Fig. 7.2(b). Using data from experiments with polymer plugs in a capillary tubes we obtained an estimate for the friction coefficient c_f . We also noted that, the initial opening pressure may differ considerably from the sub-

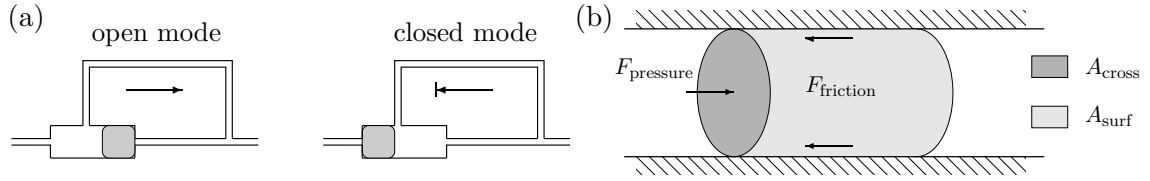


Figure 7.2: (a) Schematic of the mobile plug valve in the open and closed mode. In the open mode the flow can bypass the valve via the bypass channel. In the closed mode the plug seals off the valve. (b) Schematic of a plug in a channel. The different shadings mark the friction and pressure area respectively. The friction area has contact to the wall. The pressure area is the same as the cross section of the channel.

sequent opening pressures. This effect seemed to be even more explicit in the valve chip setting. Using the above model we then calculated the opening pressure for the relevant plug dimensions. Based on the flow rate of the EO actuator and the calculated opening pressure the hydraulic resistance of the bypass channel may be derived.

The valve fabrication involves is two steps. The first being the valve chip fabrication and the second being the plug fabrication. The polymerization process involves three steps: (1) Making an appropriate polymer compound. (2) Loading the liquid polymer solution into the channels. (3) In situ photopolymerization of the mobile polymer plugs.

7.3.1 Valve chip fabrication

The original valve design from [35] was based on a two-depth etching process of mirror identical pieces electrostatically bonded and subsequently annealed. In this way they could generate cylindrical channels with different radii. In order to simplify the fabrication process we used a single-depth etch and bonded with a flat lid. The process was optimized for making the channel walls as smooth as possible.

Microfabrication

Conventional microfabrication procedures were applied to manufacture the microvalves. Processing was made using photolithography and isotropic wet-etching in a glass substrate. Borosilicate glass substrates with a thickness of $400 \mu\text{m}$ from S. I. Howard Glass were used for this application because the transparency of glass allows for subsequent UV laser polymerization. Fig. 7.3 shows the fabrication procedure for the microvalves. The glass substrates were initially cleaned in piranha solution (50% H_2SO_4 and 50% H_2O_2) for 15 minutes, rinsed with DI water and dried in a spin rinse dryer (Semitool). Chrome (thickness 300 nm) was sputter-coated on the cleaned glass substrates to serve as a protecting layer for the subsequent wet-etching. One micron thick positive photoresist (S1813, Shipley Microposit) was deposited on the substrates and then soft-baked on a hotplate at 115°C for 70 seconds. The substrates were exposed with UV light in EVG-620 mask aligner for 13 seconds, and immersed in MF-319 developer (Shipley Microposit) for 66 seconds. After rinsing (DI water) and drying, the substrates were hard-baked on a hotplate

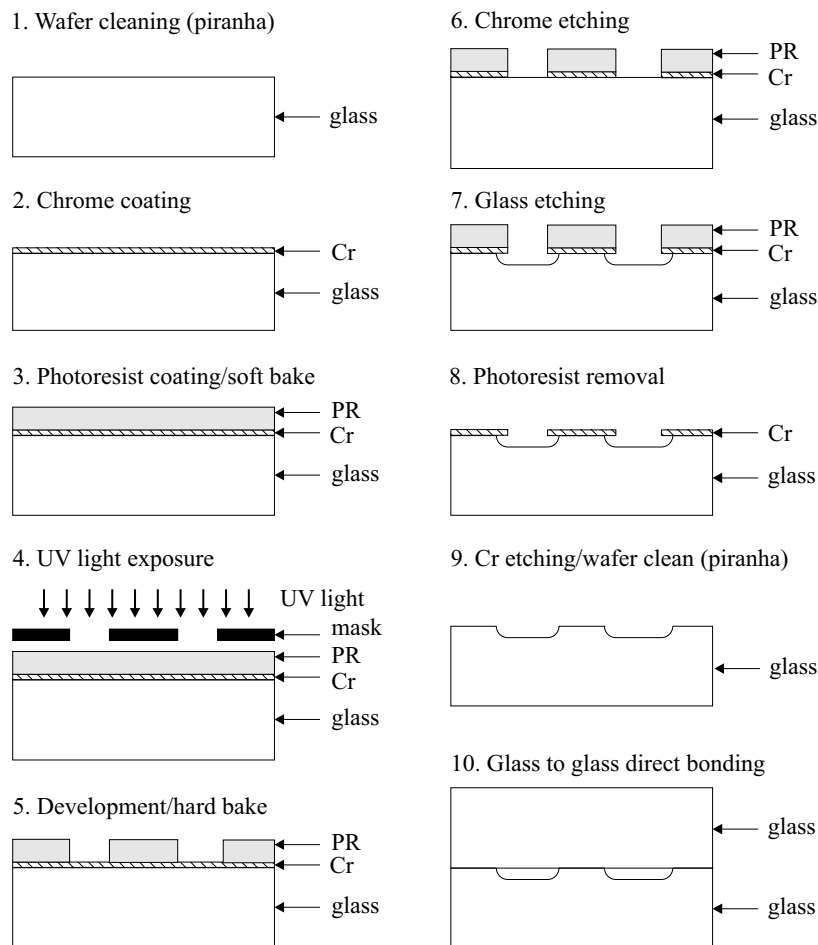


Figure 7.3: Flow chart for the fabrication process. The glass substrates are $400\ \mu\text{m}$ thick and made of borosilicate. Inlet and outlet holes were electrochemically drilled before bonding. Courtesy of Meng-Ping Chang.

at $115\ ^\circ\text{C}$ for 15 minutes. Unwanted chrome portions on the substrates was then removed in a chrome-etchant bath. The glass etchant was produced by mixing HF (49 %), HCl (49 %) and DI water in the ratio of 10:5:85. The purpose of adding HCl is to enhance the smoothness of the sidewalls of etched channels [46]. Slight agitation is necessary for improving the transportation of both fresh etchant to the glass surface and reaction product away from the glass surface, which also contributes to the surface smoothness. To achieve $25\ \mu\text{m}$ etching depth, the glass substrates were immersed in the glass etchant at room temperature ($20\ ^\circ\text{C}$) for about 40 minutes. The outlet-connection holes were manufactured by electrochemical drilling in 49 % NaOH solution. The glass to glass bonding was realized by the following procedure: submerging the glass substrates in KOH (49 %) at $85\ ^\circ\text{C}$ for 2 minutes, rinsing and drying, then exerting uniform pressure (up to 2 bar) all over the glass substrate, and finally annealing in an oven at $550\ ^\circ\text{C}$ for 5 hours.

Fittings

External fluid connection were made using nanoports from Upchurch Scientific, Fig. 7.4. The nanoport is attached to the chip using an epoxy ring. The epoxy is then cured in the oven at 135 °C for 42 min. This particular curing time was found to work better than the other ones listed by Upchurch Scientific. The fittings are rated to pressures up to 100 bar. However, a more conservative estimate of 20 bar seems more realistic based on our experience. The fittings can be removed from the chip by submerging the nanoport in acetone overnight. The O-rings and nanoport should be carefully inspected and cleaned before reusing.

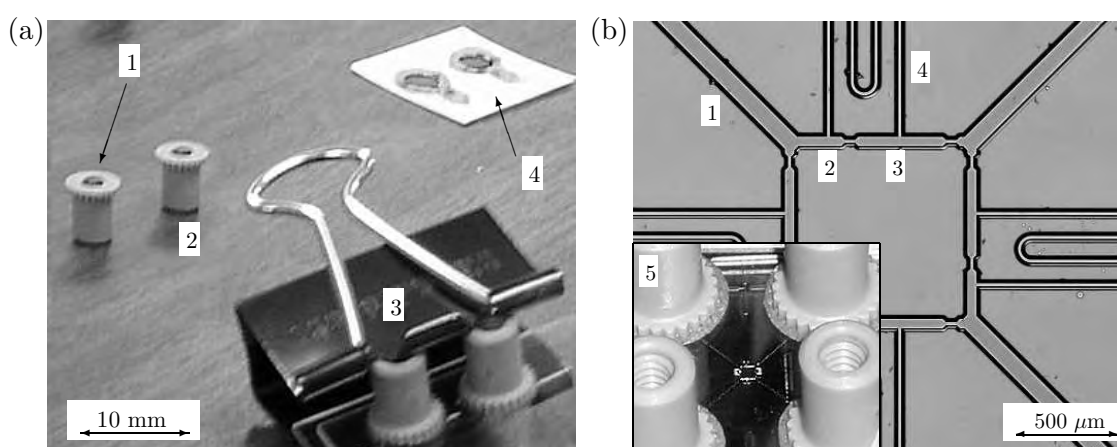


Figure 7.4: (a) Picture of the Nanoport fittings. (1) An O-ring with a square cross section fits into a nanoport (2). The nanoports are attached to the chip using a clamp (3) and epoxy rings (4). A thick glass slide is inserted between the chip and the clamp to prevent the chip from breaking. (b) Picture of the valve chip. (1) Transport channel, (2) residual channel, (3) main channel, (4) bypass channel and (5) an inset showing the position of the valve system on the valve chip.

Valve dimensions

The channel dimensions in the valve chip are given in Fig 7.5. The listed widths and lengths are the maximum, i.e., the top part of the wafer. The dimensions were measured using a 10× + 1.6× objective coupled to a CCD camera. The length and widths were recorded in pixels values. The conversion factor to physical dimensions was 1.6 μm per pixel. This conversion factor is found by using microruler of known dimensions.

7.3.2 Customizing the polymer compound

The polymer compound is critical for the properties of the polymer plugs and thereby the performance of the valves. The key ingredients were chosen according to Ref. [35]. Monomers were obtained from Sigma Aldrich, and chosen generally from the family of acrylates and methacrylates. There are five ingredients going into the recipe, see Table 7.1. Changes in the ratio between the ingredients will change the properties of the plug.

channel	width/length
side etch	25 μm
main ch.	104 μm /580 μm
residual ch.	104 μm /285 μm
bypass ch.	65 μm /1,1.7,5,10 mm
tapered ch.	66 μm /50 μm
transport ch.	150 μm /7 – 9 mm
depth	24 μm

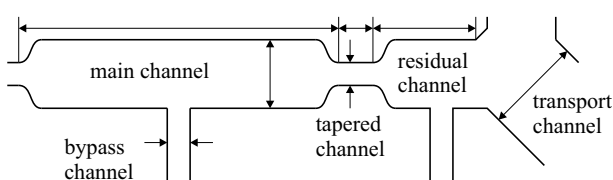


Figure 7.5: (table) Channel dimensions of the plug valve system in two different batches. (figure) Diagram for the channel sections in the valve. Width and length are indicated with arrows. The flow through a section is parallel to the length and perpendicular to the width.

function	name
monomer	2,2,2-trifluoroethyl acrylate (TFEA)
crosslinker	1,3-butanediol diacrylate (BDDA)
solvent	2-methoxyethanol
photoinitiator	2,2'-azobisisobutyronitrile (AIBN)
inhibitor	4-methoxyphenol

Table 7.1: List of ingredients in the polymer compound.

When the AIBN photoinitiator is exposed to UV light it changes state to AIBN* which starts the polymerization. The polymerization is exothermic and can be thermally initiated as well, hence an inhibitor is required to stop runaway polymerization. Inhibitors such as oxygen and 4-methoxyphenol absorb the AIBN*. By removing the oxygen it is easier to control the level of inhibitors. Twelve different recipes were tested, however, the most successful experiments were done with a recipe denoted R6. A mixture of $\mathcal{V}_{R6} \approx 1$ mL contains: 250 μL BDDA, 350 μL TFEA, 400 μL 2-methoxyethanol, 16 mg AIBN, 8 mg 4-methoxyphenol, 50 μL water. The solution is purged with nitrogen in order to remove the oxygen before use.

Elasticity and porosity

Increasing the ratio between the monomer (TFEA) and the crosslinker (BDDA) makes the plug more soft but makes it also more difficult to crosslink. A hard plug is good for holding of high pressures and durability. A soft plug can be torn or ejected from its sealing position if the pressure is high enough. However, a hard plug will not deform very well to the valve seat under low pressures. The consequence can be that the valve leaks at low adverse pressure. The solvent makes the solution less viscous and can make the plug nanoporous. A nanoporous plug can be used as a saltbridge. Allowing ions but not bulk flow to pass. A microporous plug can be generated by adding a porogen, e.g. water or

another polar solvent, to the polymer solution. Water should be added until the phase separation is observed ($\approx 5\%$). A microporous plug is softer than a nanoporous plug. In other applications the porous polymer could be useful. Microporous plugs could be used as an EO supporting frit and nanoporous plugs could be used as a salt-bridge.

Opening pressure, shrinkage and recycling

If the plug is highly crosslinked the plug is also very rigid. A rigid plug often will require a prohibitively high initial opening pressure $p_{\text{open,init}} > 20 - 100$ bar. Such high pressures can cause the chip bonding to break or the fittings to leak. Microporous plugs have low initial opening pressures compared to the nanoporous ones. A computer controlled syringe pump with pressure feedback was used for controlling the applied pressure. The pressure was gradually increased until the plug moved.

Once the plug moved the valve was flushed with either IPA or buffer. The onset of flow replaces the initial polymer solution with the flushing liquid. The plug usually shrunk because of the change in environment. If the plug shrinks too much the flow can easily go around the plug making the plug immobile. It was found that a microporous plug does not shrink as much as a nanoporous plug.

In the case that the polymerization fails the chip can be reused. After removing the nanoports in acetone the chip can be heated to $600\text{ }^\circ\text{C}$ and the polymer will turn into ash. The ash can be flushed out once new fittings have been mounted.

7.3.3 Loading the polymer solution

Filling the channels with polymer can be done in several ways. The polymer produces very smelly and quite toxic fumes. It is therefore preferred to work under the fume hood. The contact angle between glass and polymer is low. Hence the channels fill themselves due to capillary forces once polymer is introduced in one port. Using a pipette $V_{\text{load}} = 2\text{ }\mu\text{L}$ of polymer is placed in a port and the channel filling can be observed with the naked eye if one concentrates. The complete filling takes less than 3 seconds so one should pay attention because it is very difficult to distinguish an empty and a full channel. This is, however, possible in a microscope if a reference image was taken of the empty channels. Empty channels will appear with a darker shadow on the side walls than in a filled channel. If an interface exist the liquid and gas phase can be determined by observing the contact angle.

The internal volume of the chip is only $V_{\text{int}} = 0.3\text{ }\mu\text{L}$ so the excess polymer is kept in the filling reservoir. This reduces the compliance when the cap is tightened. The procedure was to fill one port with polymer and wait 1 min or more to ensure that the liquid had spread to the whole chip. Subsequently the remaining reservoirs could be filled to reduce compliance. Finally the caps are tightened in turn. Sealing of the channels are important for two reasons: (1) It eliminates toxic fumes in the lab. (2) It stops evaporation of polymer and hence puts the liquid at rest. It is impossible to observe flow if there are no particles or interfaces. Even a minor flow would interfere destructively with the polymerization process, see Fig. 7.6(a).

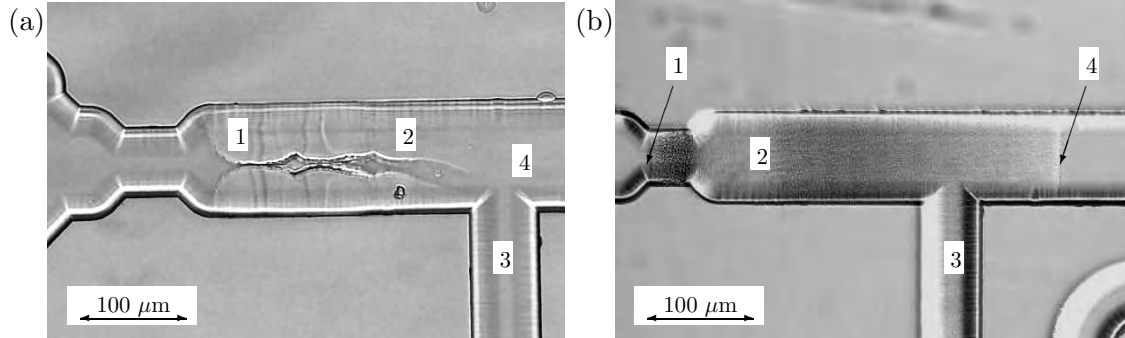


Figure 7.6: (a) Picture of a (1) plug formed while the liquid was not at rest. In such a situation the exposure time will be longer than normal and the plug will grow from the wall and out leaving a (2) cleft in the middle of the (4) main channel. Debris may also have been flushed into the (3) bypass channel. (b) In this case runaway polymerization was observed. (2) The plug fronts are indicated at (1) and (4) but also extends into (3) the bypass channel. Adding some more inhibitor (4-methoxyphenol) to the recipe solved the problem.

7.3.4 Controlling the exposure

Once the polymer is loaded into the channels the plugs are formed by exposing selected regions of the polymer filled channel to UV light. Three exposure configurations were considered: (1) Exposure through a mask in direct contact with the chip. (2) Focusing the beam into a sheath of light defining the thickness of the plug. This method requires multiple exposures for each plug (3) Shaping the exposure region to form the total plug.

The two latter methods, denoted direct exposure, use the same optical setup. They only differ in the way the plug is constructed in the length direction.

Exposure through a mask

Mask exposure has the advantage of the possibility of multiple exposures and complex shapes at the same time. One of the disadvantages is, however, diffraction from the mask. Diffraction of the UV light $\lambda = 355 \text{ nm}$ sets a limit to the resolution of the polymerization, [47].

$$b_{\min} = \frac{3}{2} \sqrt{\lambda(s + z/2)} \quad (7.1)$$

where b_{\min} is the minimum resolution dimension, s is the distance from the mask to exposed region and z is the depth of the plug. Using the values, $s = 400 \text{ μm}$ and $z = 25 \text{ μm}$ we obtain $b_{\min} = 18 \text{ μm}$. This is a relatively large value considering that the length of the plugs is of the order 100 μm . Working with mask exposure was also quite difficult from an experimental point of view. It was not possible to see the formation of the plug due to lack of light. Hence the exposure times needed to be based on data from numerous experiments. The lack of visual feedback is a major problem in the development phase. Often some kind of incident, such as bubble formation, would happen during the polymerization and

it would be important to observe this. Finally, the mask was drilled by the high intensity of the laser light. The conclusion was therefore that exposure through a mask is better suited for production than development in this particular case.

Direct exposure

Direct exposure has the advantage of more uniform intensity and allowing for optical viewing during polymerization. Laser light was shaped into a rectangle using mirrors, lenses and cutoff masks. Finally the light was focused using a Olympus 4× objective, see Fig. 7.7 and 7.8. The objective should not have too thick lenses since glass absorbs UV light. However, too much intensity makes the polymer form gases which interferes with the polymerization. The intensity can be reduced with an attenuator or by making the exposure region larger. The focal length for the 4× objective is 17 mm just enough for the nanoports with sealing caps to slip under the objective. The chip was viewed with a 10×

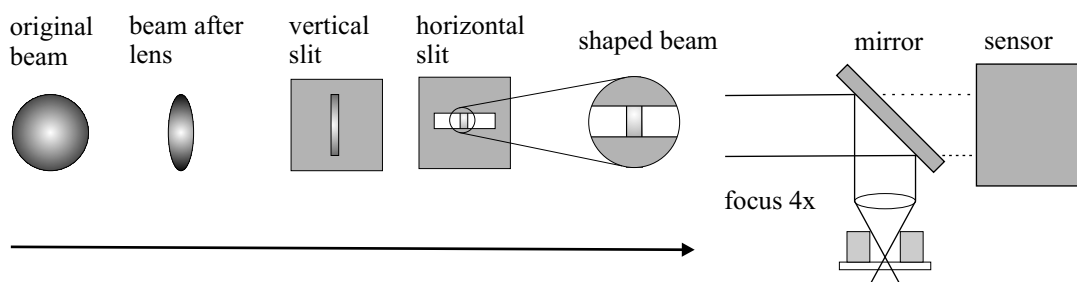


Figure 7.7: Shaping the beam from a circular shape 3 mm dia. to a rectangle $250 \mu\text{m} \times 150 \mu\text{m}$. The position of the beam before cutoff can affect the energy transmission a lot. The energy is therefore measured after the slits but without the loss from the final UV mirror and focusing objective.

objective from below. The lens was protected from the UV light with a sheath of polymer placed directly above the objective to prevent accidentally drilling of the objective. The exposure area was visualized using UV fluorescent dye placed between two $100 \mu\text{m}$ thick glass covers. The chip is made of two $400 \mu\text{m}$ glass pieces. Hence a small misalignment exists in the focus of the viewed and actual exposed region. The laser was operated in low intensity mode while the exposure region was shaped. Once the correct shape was achieved the dye was removed and the real chip inserted. Using the x - y manipulator on the microscope the chip was put in position. The boom shown in Fig. 7.8 was demounted after each experiment. The two different exposure modes can be seen in Figs. 7.9(a-b). The box exposure has the advantage of making the whole plug simultaneously. It was, however, quite difficult to obtain a uniform light intensity and avoid fringe patterns from the cutoffs. With the sheath exposure it was easy to obtain a uniform light intensity. The method did, however, require precise alignment and longer exposure times. In the end the box exposure was preferred.

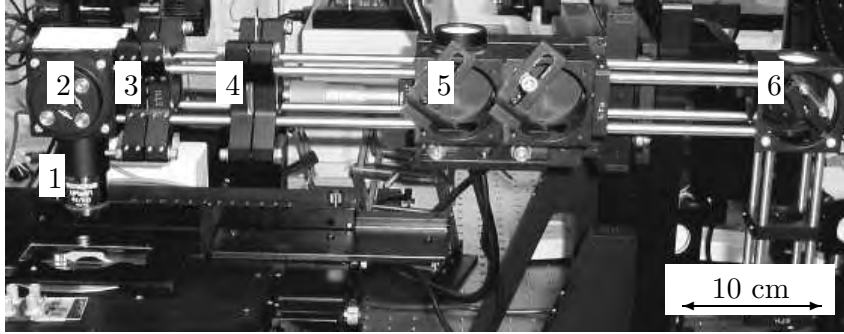


Figure 7.8: Picture of the optical setup. (1) The focusing lens was typically a $4\times$ objective. (2) Adjustable UV mirror. For intensity measurements the mirror would be removed and a sensor placed instead at the end of the boom. (3) Horizontal slit. (4) Vertical slit. (5) Boom mount. The boom was demounted after each experiment so that other people could use the microscope. (6) UV mirror.

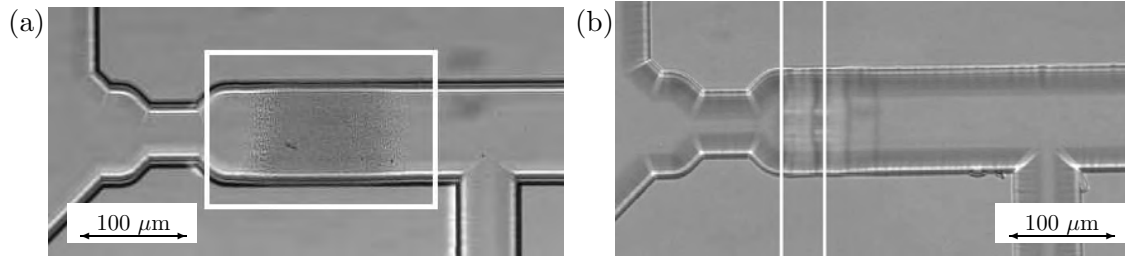


Figure 7.9: (a) The region within the white box is exposed to UV light. Notice that the exposure region is somewhat larger than the plug. This is done to increase plug growth rate and hereby decrease the total dose. (b) Sheath exposure region marked with a white lines. The final plug will be constructed from multiple overlapping exposure regions. In the picture 3 out of 5 exposures are completed.

Light intensity

The UV light source was a frequency tripled Nd:YAG laser ($\lambda = 355$ nm) operating at 10 Hz with a pulse energy of 4.5 mJ/pulse. The size of light beam at the source was approximately 3×3 mm² giving an intensity of 50 mJ cm⁻²/pulse. The sensor used has a maximum intensity of 100 mJ cm⁻²/pulse. The minimum pulse energy it could measure was 0.015 mJ/pulse.

In order to have consistent exposure it is necessary to measure the pulse energy from the laser. The optimal place to measure the intensity would be right above the chip. However, due to its size it was not possible to fit the sensor in that position. One of the main causes of variations in transmission of energy is misalignment of the beam when it is cutoff. The sensor was therefore positioned after the two cutoffs, see Fig. 7.7.

The power of the laser can be adjusted using the attenuator. The sensor is not sensitive enough to measure the pulse energy after the cutoffs in the reduced mode. Hence the

energy is measured in full power mode. Then the ratio between full power and reduced power is found at the source of the laser. In this way one can estimate the energy transmitted after the cutoffs. The energy measurements are made without the mirror installed. So the beam goes directly into the sensor, see Fig. 7.7. There will still be some loss in the transmission from the final UV mirror and the focusing objective. However, this loss is considered to be relatively consistent from experiment to experiment.

Controlling the plug size

The width of the exposure region should be wider than the channel in order to make the plug conform to the shape of the cross section. The length of the exposure region should be such that the plug generated has a length of 1.5 – 2 times the channel width. The plug needs to have a certain length in order to prevent tilting when moving back and forth, see Figs. 7.10(a-b). Long exposure times tend to increase the dose more than the length of the plugs. In order to minimize the dose it is therefore optimal to stop the exposure when the plug size ratio has reached about $w/a = 0.7 - 0.8$, see Fig. 7.10(c).

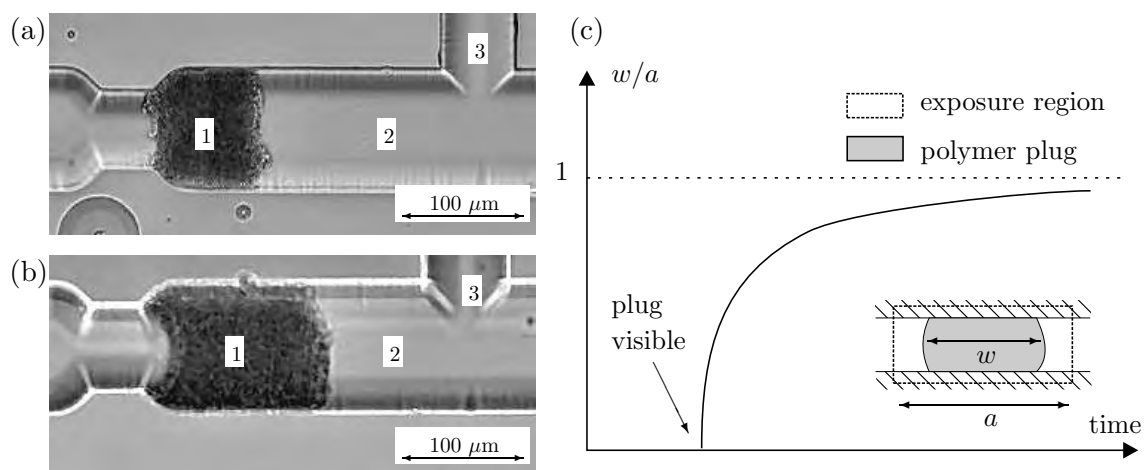


Figure 7.10: (a) Picture of a short (1) microporous plug (R6 recipe). The plug length is close to the width of the channel. A short plug is likely to get stuck in the junction between (3) the bypass and (2) the main channel. (b) Picture of a plug with an appropriate length. After polymerization the plug can shrink up to 30% when exposed to a different solution. The labels are the same as in panel (a). (c) The growth of the plug is not linear. Initially the plug is invisible. After 20-30 seconds it should be visible and usually exposure is ceased after 60 seconds or less.

7.3.5 Valve characterization

The valve system is a critical part of the pumping system. Unless the valve system meets the requirements for switching flow rates and pressures the pump will not work.

The valves are characterized by the following parameters: (1) Initial opening pressure. (2) The flow rate required to switch the valve state from open to closed, i.e., *switch open*

→ *closed*. If the switch flow rate is higher than what the EO actuator can supply the valve will never close. (3) The pressure required to switch the valve state from closed to open, i.e., *switch closed* → *open*. If the switch pressure is higher than what the EO actuator can supply the valve will remain closed. (4) The ratio between hydraulic resistance in the closed and open mode, i.e., the diodicity.

Experimentally

The fluidic setup was very similar to that described in Fig. 2.5. The only difference is that we used a syringe pump instead of pressurized reservoirs. Pressures were measured using 0-10 bar pressure transducers from Honeywell, Freeport, IL, USA. The flow rate was measured by collecting fluid in a reservoir placed on a Mettler AB104 balance with 0.1 mg precision. The flow was provided by a LABVIEW controlled syringe pump. The flow rate of the syringe pump was set through a feedback control loop to maintain a constant pressure.

The switch flow rate was measured by slowly increasing the flow rate of the syringe pump until the valve switched position. The switch flow rate does vary a lot because of variations in friction between plug and wall.

The switch pressure was measured in a similar way. By controlling the syringe pump the pressure could be gradually increased until the plug moved from its seat. This value could be dependent on the valve history. If the valve prior to opening had been holding off high pressures it could be jammed into the valve seat. This effect could be avoided by changing the valve seat geometry or by increasing the hardness of the plug.

Results

The valve characteristics for two different 4-valve systems are shown in Table 7.2 and Table 7.3. The valve system in Table 7.4 is only a 2-valve system. This means that it only rectifies in one pumping direction. Each of the valves in a system is given a letter *a-d* and characterized individually in terms of initial opening pressure, switch flow rate and switch pressure. The overall hydraulic resistance of the system in closed and open configuration is also measured. The individual valve configuration in the closed mode is noted. The ratio $R_{\text{closed}}/R_{\text{open}}$ is the diodicity. The data for the plug exposure energy is associated with large uncertainties.

Valve system 1	<i>a</i>	<i>b</i>	<i>c</i>	<i>d</i>
Initial opening	0.6 bar	0.6 bar	3 bar	5 bar
Switch open → closed	$2.5 \mu\text{L min}^{-1}$	$1.7 \mu\text{L min}^{-1}$	$1.7 \mu\text{L min}^{-1}$	$5 \mu\text{L min}^{-1}$
Switch closed → open	0.15 bar	0.01 bar	0.02 bar	0.2 bar
Closed mode	open	closed	closed	open

Table 7.2: The diodicity was found to be $R_{\text{closed}}/R_{\text{open}} = 48$. The valves have 10 mm bypass channels and the liquid is IPA at 25 °C. Parameters: R6 recipe, 14 Jun 2004, plug exposure 1.8 J cm^{-2} .

A few single valves were also fabricated for test purposes, see Fig. 7.11. This single valve had the highest diodicity of 85. In general the low diodicities may be caused by

Valve system 2	<i>a</i>	<i>b</i>	<i>c</i>	<i>d</i>
Initial opening	< 1 bar	< 1 bar	< 1 bar	< 1 bar
Plug length	200 μm	191 μm	205 μm	218 μm
Switch open \rightarrow closed	20 $\mu\text{L min}^{-1}$	10 $\mu\text{L min}^{-1}$	5 $\mu\text{L min}^{-1}$	1.7 $\mu\text{L min}^{-1}$
Switch closed \rightarrow open	1.8 bar	0.24 bar	0.03 bar	0.03 bar
Closed mode (out to in)	closed	closed	closed	open

Table 7.3: The diodicity was found to be $R_{\text{closed}}/R_{\text{open}} = 28$. The valves have 10 mm bypass channels and the liquid is IPA at 20 °C. Parameters: R6 recipe, 15 Jun 2004, plug exposure 3.4 J cm⁻².

Valve system 3	<i>a</i>	<i>b</i>	<i>c</i>	<i>d</i>
Switch open \rightarrow closed	5 $\mu\text{L min}^{-1}$	5 $\mu\text{L min}^{-1}$	-	-
Switch closed \rightarrow open	0.03 bar	0.03 bar	-	-
Closed mode (out to in)	closed	closed	blocked	blocked

Table 7.4: The diodicity was found to be $R_{\text{closed}}/R_{\text{open}} = 35$. The valves have 1.7 mm bypass channels and the liquid is IPA at 20 °C. $R_{\text{open}}^{-1} = 7.3 \mu\text{L (min bar)}^{-1}$. Valve c and d did not work well enough and were subsequently blocked by extra polymerization. The valve system therefore only works as a halfway rectifier. Parameters: R6 recipe, 9 Jun 2004, plug exposure 2.5 J cm⁻².

the fact that the plugs are microporous and hence flow can go through them. Another explanation is that the single depth layout of the valve is a disadvantage from a sealing point of view.

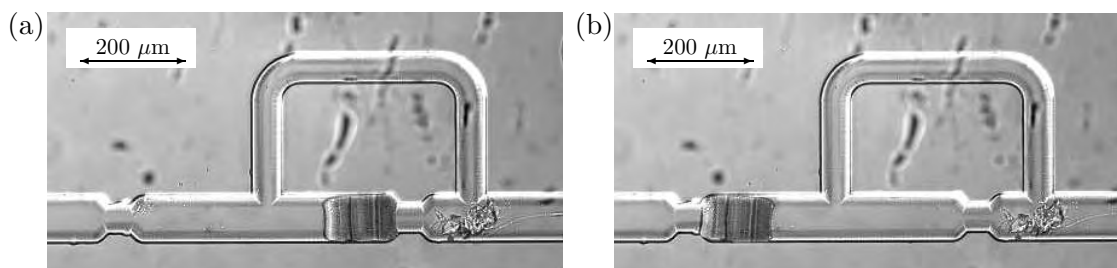


Figure 7.11: Microvalve with mobile polymer plug (R6 recipe). The channel depth is 25 μm . The bypass channel is 1 mm long. Diodicity measured to $R_{\text{closed}}/R_{\text{open}} = 85$. (a) Valve is open because flow can go through the bypass channel. (b) Valve is closed because the plug is sealing against the channel tapering. Debris from the polymerization can be seen in the residual channel.

7.4 Pump characteristics

A pump characteristic is shown in Fig. 7.12(a). It is obtained with the EO actuator coupled to a valve system as shown in Fig. 7.1. The valve system worked well for a short period of time. In that time the $Q - p$ characteristic of the pump was recorded over a period of 20 min. The relation is seen to follow the expected linear relationship. The performance

was $\Delta p_m = 0.55$ bar and $Q_m = 3 \mu\text{L min}^{-1}$ at $\Delta V = 30$ V and $T = 20$ s. Both these values are much smaller than expected. This is due to the compliance in the EO actuator and the very inefficient valve system. The compliance in the actuator came from bubbles generated at the electrodes. One explanation is that the large flow resistance of the valve system caused the pressure in the actuator to drop significantly when in suction mode. The low pressure then caused the, otherwise bubble-free, electrodes to emit bubbles.

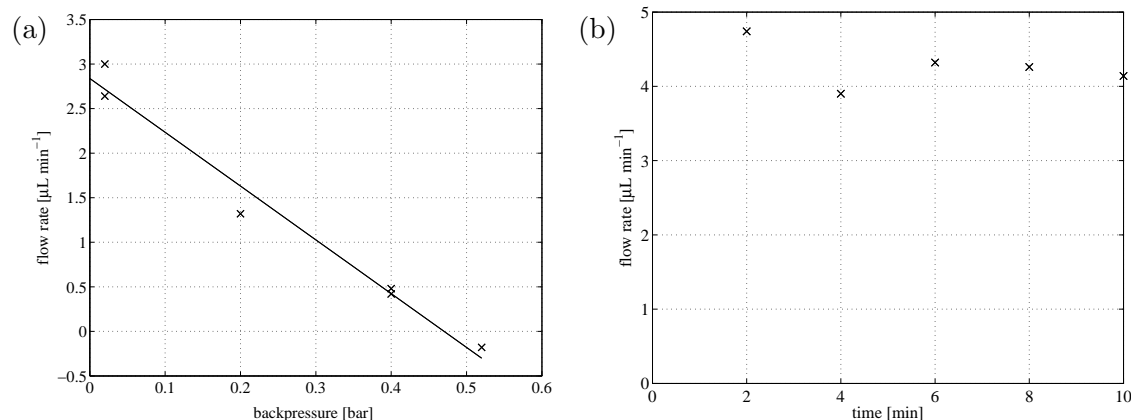


Figure 7.12: (a) Pump characteristic using valve system 1. The pump is operated at $\Delta V = 30$ V, with a period of $T = 20$ s, $c = 5$ mM phosphate buffer, pH = 6.5. $Q_m = 2.8 \mu\text{L min}^{-1}$ and $\Delta p_m = 0.55$ bar. There were some bubbles in the electrode chamber. The valves would also occasionally get stuck. In the measurements above all valves were active. (b) Free flow rate measurements in sequence. The flow rate is fairly stable, however, very sensitive to the proper function of the valve system. The average flow rate is approximately $Q_m = 4.3 \mu\text{L min}^{-1}$ with same parameters as in panel (a).

In a second run the free flow rate Q_m was measured as a function of time, see Fig. 7.12(b). The flow rate $Q - t$ varies less than 15% over a 10 min period. After that time one of the valves ceased to function and the measurement was stopped. The R6 valves also seemed to wear over time so it was difficult to reproduce the results. Finally, the flow rate is plotted against the actuation period, see Fig. 7.13. In an ideal pump the flow rate would be independent of this period. However, due to the compliance of the system we see an increase in flow rate with increasing period. This is consistent with the predictions from the equivalent circuit model simulations, see Appendix A.

7.5 Conclusion

An electroosmotic pump with microvalves has been fabricated and tested. The electroosmotic actuator was based on a commercially available frit and bubble-free palladium electrodes. Palladium was used because of its ability to store hydrogen in its atomic lattice. A system of microvalves with mobile monoliths were tested. Due to the geometry of the valve seat only a relatively low diodicity $\approx 30 - 85$ was achieved. Furthermore, a high fluidic resistance in the valve system caused a significant drop in pressure on the suction

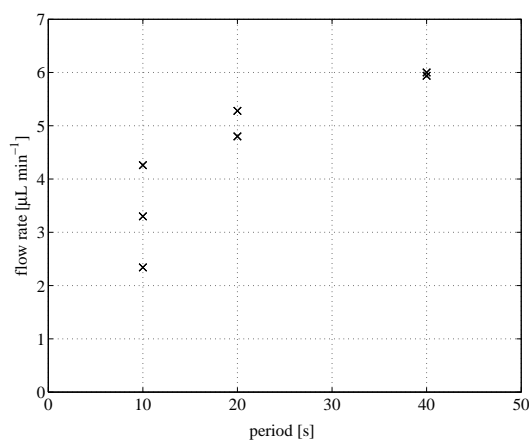


Figure 7.13: Flow rate versus actuation period. Pump operated at $\Delta V = 10\text{ V}$, $c = 5\text{ mM}$ phosphate buffer. Valve system 3 (2-way). The flow rate of the EO actuator was measured to $Q_m = 17\ \mu\text{L min}^{-1}$. Hence approximately than 35% is transferred to the pump.

side. This drop in pressure was enough to release hydrogen from the palladium electrodes and into the solution. The gas added a large amount of compliance to the system which dramatically lowered the performance of the pump. Two improvements are needed: (1) A microvalve with lower hydraulic resistance when it is open. An improved design with wider transport channels was designed but not fabricated due to lack of time. In the original valve design [35] the channel cross sections are round. The round channels gives a better seat for the plugs to seal against. However, the movement of the valves was also a problem. (2) Reliability and durability of the plugs must also be improved to ensure long-term operation. In many cases the plugs would be deformed after polymerization. The best performing plugs were very soft. However, their good qualities in sealing would work against them in terms of durability. The challenge is to construct a soft but durable plug that retains its size when exposed to different solvents. Sandia National Laboratory has worked with this valve concept for several years. A recent paper by Kirby *et al.*, [36] presents the latest advances with the mobile polymer plug valve.

Chapter 8

Additional pump projects

In this chapter three separate pump related projects are presented.

The first project is a design idea for an EO pump capable of pumping all types of liquids especially oils. The pump is denoted the two-liquid viscous EO pump. The design has still yet to be realized, but the concept has been analyzed in the paper *A novel electroosmotic pump design for nonconducting liquids: theoretical analysis of flow rate-pressure characteristics and stability* by A. Brask, G. Goranović, M.J. Jensen and H. Bruus, [13]. The full paper is presented in Appendix C.

The second project is a theoretical analysis of an existing EO pump by Y. Takamura *et al.*, [20]. One of our purposes was to verify the validity of equivalent circuit theory in EO pump analysis. The analysis resulted in the paper *Theoretical analysis of the low-voltage cascade electroosmotic pump* by A. Brask, G. Goranović and H. Bruus, [14]. The full paper is presented in Appendix D.

The third and ongoing project involves a recently proposed pumping mechanism by A. Ajdari (2000): *Pumping liquids using asymmetric electrode arrays*, [48]. The effect is also denoted induced-charge EO pumping (IC EO). In the capacity of co-supervisor together with Prof. Henrik Bruus we planned to design and build a pump based on this effect. In 2003 a BSc. project by Morten Arnoldus and Michael Hansen was set up. A pump was designed and fabricated but not tested successfully. In 2004 the project was continued with a MSc. project by Misha M. Gregersen. Preliminary tests have been successful.

8.1 The two-liquid viscous EO pump

8.1.1 Background

The two-liquid viscous EO pump is a design idea that was first presented in my master thesis, *Principles of electroosmotic pumps* from 2002, [8]. The design was only supported by relatively simple simulations in the thesis. The used CFD software COVENTOR 2001.3 was only capable of simulating miscible liquids. It was therefore a major challenge to predict the behavior of the pump in the immiscible case superposed with electric fields. In 2004 fellow PhD students Mads J. Jensen and had developed a CFD code capable of

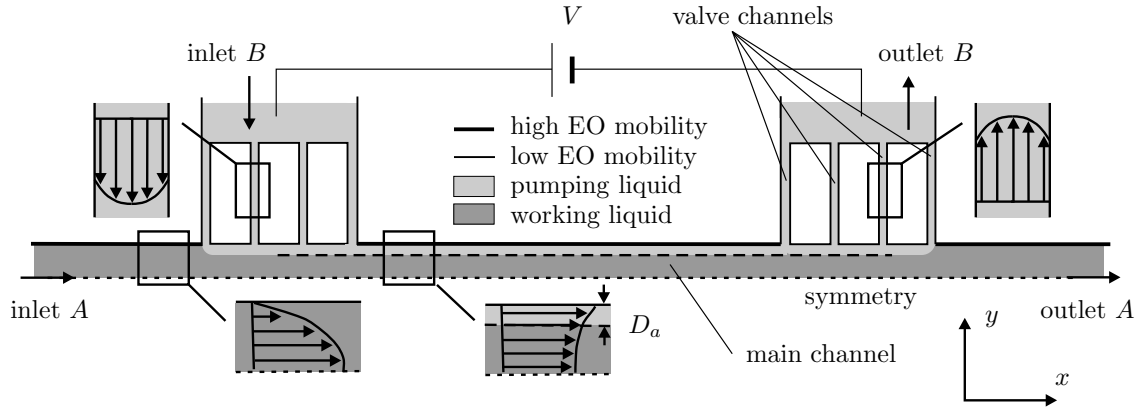


Figure 8.1: Top view of a possible design of the two-liquid viscous pump. The nonconducting working liquid (dark gray) is being dragged by the EO driven pumping liquid (light gray) that flows along the edge of the main channel. The pump is mirror-symmetric around the central vertical plane, and only one half is shown. The un-coated walls are marked as the thick edges of the main channel. Coated walls are marked with thin edges. In inlet A and outlet A the flow is parabolic, while in the valves and in the main channel it is a superposition of parabolic and an EO driven plug flow.

handling free surfaces and Dr. Goran Goranović a theory for electrohydrodynamic induced instabilities. These tools were then used to evaluate the stability of the interface. We found that the interface would be stable in normal operating conditions, [13]. We therefore proceeded with publishing the design idea.

8.1.2 Introduction

In Fig. 8.1 a possible realization of the design is shown. The nonconducting working liquid is being dragged along by the conducting pumping liquid. Based on computational fluid dynamics the flow rate is estimated to be of the order $Q_m \approx 1 \text{ nL (s V)}^{-1}$ and the pressure capacity $\Delta p_m \approx 100 \text{ Pa V}^{-1}$ depending on the achievable geometries and surface chemistry. The pumping liquid is introduced to the main channel through the array of side channels denoted the pressure valves. This is properly one of the most important innovative ideas in the design and is therefore explained in more detail in the following.

8.1.3 Pressure valves

The function of the pressure valve is to introduce the pumping liquid into the main channel while maintaining the pressure buildup in the main channel, see Fig. 8.1.

In the case of an infinitely thin Debye layer the EO flow rate in a rectangular microchannel of length L , height H , and width a is given by

$$Q_{\text{eo}} = u_{\text{eo}} H a = \alpha_{\text{eo}} \Delta V \frac{H a}{L} \propto a. \quad (8.1)$$

Here u_{eo} is the electroosmotic velocity, α_{eo} is the electroosmotic mobility, and ΔV is the

electric potential drop inside the channel. We refer to this situation as ideal EO flow. The associated EO pressure p_{eo} is given by

$$\Delta p_{eo} = Q_{eo} R_{hyd} = \alpha_{eo} \Delta V \frac{H a}{L} R_{hyd}. \quad (8.2)$$

The hydraulic resistance of a high aspect ratio rectangular channel $H \gg a$, can be found in Table 8.1. The pressure driven flow rate Q_p through the channel is given by

$$Q_p = \frac{\Delta p}{R_{hyd}} \propto a^3, \quad (8.3)$$

where Δp is the pressure drop along the channel.

From Eqs. (8.1) and (8.3) it follows that pressure driven flow will be negligible compared to the EO flow for small values of a . This can be used to obtain a kind of pressure valves in the two-liquid viscous pump. If narrow channels are placed on the sides of the main channel, their large hydraulic resistance prevents a significant loss of the pressure from the pump into the sides, while at the same time allows the driving EO flow to pass through them. Many are needed in order to minimize the electrical resistance. The pressure valves offer two additional advantages. The electrode reservoirs separated by the valves can be exposed to atmospheric pressure. Thus bubble formation from electrolysis will not enter the pump and cause problems. Furthermore, this allows for placing the pump anywhere in a fluidic network.

8.1.4 Conclusion

The two-liquid EO pump is as previously mentioned only a design idea. It will be quite difficult to build due to the high aspect channels and possible need for EO retarding coatings. The priming of the pump will also be critical in the case of immiscible liquids. The pump is also very weak in terms of pressure $\Delta p_m \approx 100 \text{ Pa V}^{-1}$ and flow rate $Q_m \approx 1 \text{ nL (s V)}^{-1}$ compared to other types of micropumps. So unless there is a specific need for this type of pump my guess is that it will never be built. However, the concept of pressure valves may be very useful in situations where electrical contact is needed without fluidic contact, i.e, similar to an ion exchange membrane.

8.2 Equivalent circuit theory

8.2.1 Background

Equivalent circuit theory was first applied to EO pumps in 2001 by W. E. Morf *et al.* [16]. Inspired by this work a theoretical analysis of the low-voltage cascade EO pump was presented in my master thesis from 2002, [8]. The low-voltage cascade pump had been published in a conference proceeding without any theory. The paper *Theoretical analysis of the low-voltage cascade EO pump* was published in 2003, [14] and has already picked up a number of citations which demonstrates the need for useful analytical tools in microfluidics. The following sections are based on this paper.

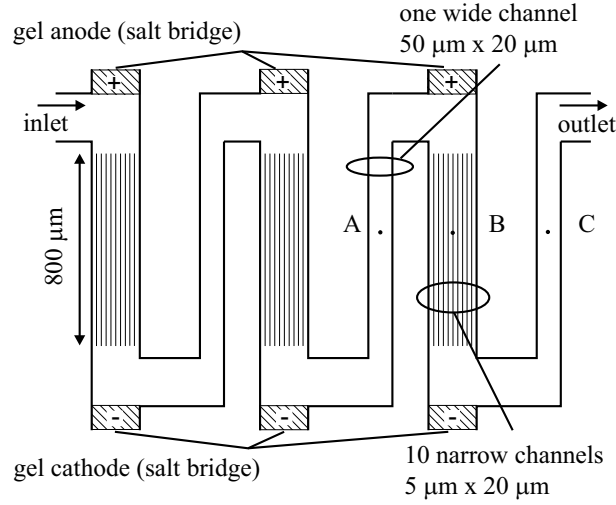


Figure 8.2: Top view of the low-voltage cascade EO pump with three steps (adapted from Fig. 3 in Ref. [20]). The total pressure is proportional to the number of steps. The EO flow is driven through many parallel narrow channels by a forward electric field and through one wide channel with a reversed electric field. A net flow is thus generated without accumulation of voltage.

To set the stage for the analysis we briefly recapitulate the working principles of the low-voltage cascade EO pump, [20]. The pump is designed to work as an effective pressure source for low applied voltages. The layout of the pump is shown in Fig. 8.2.

The main principle is to connect multiple EO pumps in series in order to accumulate pressure. Each elementary EO pump (denoted a step) consists essentially of a narrow channel section, marked B in Fig. 8.2, containing ten parallel channels, followed by a wide channel section, marked C in Fig. 8.2, containing a single channel. The EO flow in the narrow channel section acts as a high pressure pump with forward electric field. In the wide channel section the electric field is reversed, but here the channel is so wide that the induced backpressure is small compared to the previous pressure. After flowing through one such pump step the accumulated voltage is thus zero, while an appreciable pressure is maintaining a net flow. This ensures EO pumping using a low operating voltage, indeed an attractive feature allowing the pump to be operated with a battery and thus to be portable. Furthermore, it is more safe to use low voltages. The disadvantage of a cascade pump is the extra complexity of the many electrodes.

8.2.2 Introduction

We begin our analysis by noting that water at room temperature has the kinematic viscosity $\nu = 10^{-6} \text{ m}^2 \text{ s}^{-1}$, and when, as in the experiment, it flows with the velocity $u \approx 10^{-3} \text{ m s}^{-1}$ through a channel of width $a = 50 \text{ } \mu\text{m}$, the Reynolds number, $Re = u a \nu^{-1} = 0.05$, is minute. For such a low Reynolds number the flow is laminar and the viscous forces are dominant. In the case of uniform flow, i.e. zero spatial derivatives in the flow direction, the Navier-Stokes equation becomes linear.

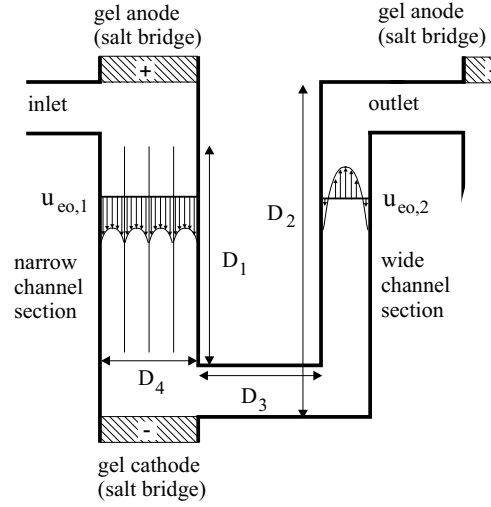


Figure 8.3: Simplified schematics of one step of the cascade EO pump shown in Fig. 8.2. The flow profiles in both narrow and wide channels are shown. There are ten channels in the narrow channel section, but for clarity only four are depicted. Even though the flow is reversed near the wall in the wide channel, the net flow is still positive. The parameters taken from Ref. [20] are: $D_1 = 800 \mu\text{m}$, $D_2 = 1230 \mu\text{m}$, $D_3 = 170 \mu\text{m}$, and $D_4 = 185 \mu\text{m}$.

In this limit, for a steady-state flow through a channel with a hydraulic resistance R_{hyd} , the flow rate Q_{hyd} induced by the pressure drop Δp_{hyd} is

$$Q_{\text{hyd}} = \frac{\Delta p_{\text{hyd}}}{R_{\text{hyd}}}. \quad (8.4)$$

The electroosmotic pressure Δp_{eo} , is defined as the hydraulic backpressure needed to balance the EO flow, i.e. $|Q_{\text{eo}}| = |Q_{\text{hyd}}|$. The total flow rate Q of a channel with both a pressure driven flow and an EO flow is simply

$$Q = Q_{\text{eo}} + Q_{\text{hyd}} = \frac{\Delta p_{\text{eo}} + \Delta p_{\text{hyd}}}{R_{\text{hyd}}}. \quad (8.5)$$

Likewise, the resulting velocity profile is given by a superposition of the velocity profiles of the EO flow and the pressure driven flow, respectively [7].

8.2.3 Analysis of the EO pump

The EO induced pressure buildup is very large in the narrow channel section, and thus the flow profile in this section becomes only slightly deformed under the influence of the actual backpressure. The resulting velocity profile u_1 , shown in Fig. 8.3, is a sum of a large, positive and flat EO flow velocity profile and a small, negative and parabolic backpressure velocity profile. The pressure buildup in the narrow channel section is denoted $\Delta p_{\text{eo}}^{\text{N}}$.

In the wide channel the electric field is reversed. A part of the pressure generated in the narrow section is therefore used both for overcoming the reversed, small, and flat EO

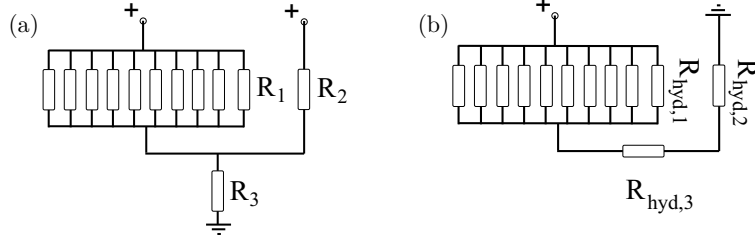


Figure 8.4: (a) The equivalent electrical circuit used in the calculation of potential drop across the EO section. (b) The slightly different equivalent circuit for the fluidic network used in the calculation of flow rates. There are $N = 10$ narrow channels each with the hydraulic resistance $R_{\text{hyd},1}$. In our calculations $R_{\text{hyd},3}$ is neglected.

flow profile and for driving the flow by pressure. The resulting velocity profile is the large, forward parabolic-like velocity profile u_2 shown in Fig. 8.3. It is evidently imperative to make the channel width considerably larger in this section to keep its backpressure to a minimum. The pressure drop in the wide channel section is denoted $\Delta p_{\text{eo}}^{\text{W}}$.

The final pressure buildup $\Delta p_{\text{step}}^{\text{max}}$ along the whole step is the EO pressure buildup in the narrow channel section minus the backpressure drop in the wide channel section,

$$\Delta p_{\text{step}}^{\text{max}} = \Delta p_{\text{eo}}^{\text{N}} - \Delta p_{\text{eo}}^{\text{W}}. \quad (8.6)$$

Refer to Eq. (8.2) for an analytical expression of the electroosmotic pressure.

8.2.4 Fluidic network model

The concepts from the previous section can be used to analyze the pump using the so-called equivalent circuit theory. In this theory the hydraulic resistance of a fluidic network is calculated by representing individual sections with equivalent hydraulic resistors using the usual rules for series and parallel resistors. The flow rate and the pressure drop for a hydraulic resistor are related by Eq. (8.4). For details see Ref. [16].

The equivalent circuit theory is only exact for a uniform and laminar flow. Hence it is not possible to analyze the flow near a bend. In the following analysis the bends are neglected, an approximation that is justified by CFD simulations.

The first step is to find the equivalent diagram for the pump. It consists of a parallel coupling of $N = 10$ identical resistors $R_{\text{hyd},1}$ followed by $R_{\text{hyd},3}$ and $R_{\text{hyd},2}$ in series as shown in Fig. 8.4(b). $R_{\text{hyd},1}$ and $R_{\text{hyd},2}$ are then computed using Table 8.1. The short channel connecting the narrow and wide channel sections can safely be neglected since $R_{\text{hyd},3} \ll R_{\text{hyd},1}, R_{\text{hyd},2}$. The total hydraulic resistance $R_{\text{hyd}}^{\text{total}}$ is therefore given as

$$R_{\text{hyd}}^{\text{total}} = N^{-1} R_{\text{hyd},1} + R_{\text{hyd},2}. \quad (8.7)$$

The maximum flow rate and backpressure of the low-voltage cascade EO pump is

$$Q_{\text{m}} = \frac{\Delta p_{\text{step}}^{\text{max}}}{R_{\text{hyd}}^{\text{total}}} \quad (8.8)$$

$$\Delta p_{\text{m}} = \Delta p_{\text{step}}^{\text{max}} \times N_{\text{step}} \quad (8.9)$$

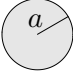
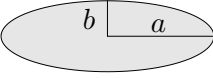
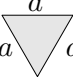
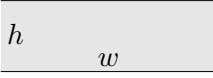
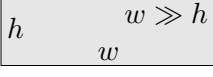
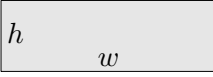
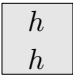
shape		R_{hyd}
circle		$\frac{8}{\pi} \mu L \frac{1}{a^4}$
ellipse		$\frac{4}{\pi} \mu L \frac{1 + (b/a)^2}{(b/a)^3} \frac{1}{a^4}$
triangle		$\frac{320}{\sqrt{3}} \mu L \frac{1}{a^4}$
two plates		$12 \mu L \frac{1}{h^3 w}$
rectangle		$\frac{12 \mu L}{1 - 0.63(h/w)} \frac{1}{h^3 w}$
rectangle		$\frac{12 \mu L h^{-4}}{\frac{w}{h} - \sum_{m=0}^{\infty} \frac{192}{\pi^5 (2m+1)^5} \tanh \left[\frac{(2m+1)\pi w}{2h} \right]}$
square		$\frac{12 \mu L}{1 - 0.917 \times 0.63} \frac{1}{h^4}$

Table 8.1: A list over the hydraulic resistance for straight channels with different cross sectional shapes. Consider a flow Q of a fluid with dynamic viscosity μ in a channel of length L . If the pressure drop over the channel of length L is Δp the flow rate is simply, $Q = \Delta p R_{\text{hyd}}^{-1}$. Courtesy of Henrik Bruus.

where N_{step} is the number of step is in the pump. In Table 8.1 hydraulic resistances of other cross sectional shapes are given.

8.2.5 Conclusion

Our theoretical analysis of the low-voltage cascade EO pump demonstrated the usefulness of equivalent circuit theory. It is my experience that equivalent circuit theory are often considered to be more difficult than it really is. The above analysis shows that it was possible to analyze relatively complex geometries by very simple means. With a spreadsheet software such as MICROSOFT EXCEL a fast and flexible model can be constructed in a matter of minutes. An equivalent circuit analysis should therefore always be done before a microfluidic device is constructed. A more advanced equivalent circuit model including nonlinear and time-dependent flow components is presented in Appendix A.

8.3 Induced-charge EO pumping

8.3.1 Background

In 1997 it was discovered that applying AC voltages to closely spaced microelectrodes could generate fluid circulation, [49, 50]. In 2000, A. Ajdari then proposed that by introducing an asymmetry, either geometrical or surface related, in the electrode array a net flow could be obtained, [48]. Brown *et al.* demonstrated the induced-charge EO (IC EO) effect six months later experimentally, [51]. In 2004, V. Studer *et al.*, [52] came with a more comprehensive experimental investigation of the pumping phenomenon.

8.3.2 Introduction

In 2003 we set up a BSc. project by Morten Arnoldus and Michael Hansen, supervised by Prof. Henrik Bruus and myself. The ambitious goal of the project was to design and build the first AC induced-charge EO pump. Brown *et al.* had demonstrated induced velocities up to about $v_{\text{slip}} \approx 100 \mu\text{m s}^{-1}$. However, the geometry of the pumping segment they used was unsuited for pumping purposes. The idea was to change the geometry while keeping the remaining parameters unchanged.

8.3.3 First IC EO pump generation

In 2003 the first IC EO pump generation was designed for actual pumping. In order to achieve that the pumping channel must be long, wide and shallow. The pumping channel must be long and shallow to achieve pressure and wide in order to increase the flow rate. A compact and elegant chip format was obtained by folding the pumping channel into a meander, see Fig. 8.5. In this way a 20 cm long, 1 mm wide and 10 μm deep channel is fitted onto a $18 \times 22 \text{ mm}^2$ chip.

The gold electrodes were defined by standard photolithography technique. Channels were made by applying a 10 μm SU-8 photoresist layer onto the electrode chip. Again photolithography was used to define the channels. Finally a PMMA coated glass lid was bonded on to seal of the channels.

The theoretical pump performance was $Q_m = 0.5 \text{ nL s}^{-1}$ and $\Delta p_m = 120 \text{ Pa}$, based on a slip velocity of $v_{\text{slip}} = 100 \mu\text{m s}^{-1}$. However, no pumping was ever observed because of two critical flaws: (1) The bonding process was extremely poor which meant that less than 10% of the produced chips was properly bonded. (2) The electrodes are arranged in such a way that each electrode lane is 16 mm long and between 10-60 μm wide. The length of the lanes made it susceptible to short circuits or loose connections. The grim consequence was that all of the 27 fabricated chips would either not be sealed or short circuited.

8.3.4 Second IC EO pump generation

In our second pump generation from 2004 by MSc. student Misha M. Gregersen the mistakes from the first generation was corrected. Instead of using thermal bonding, the more

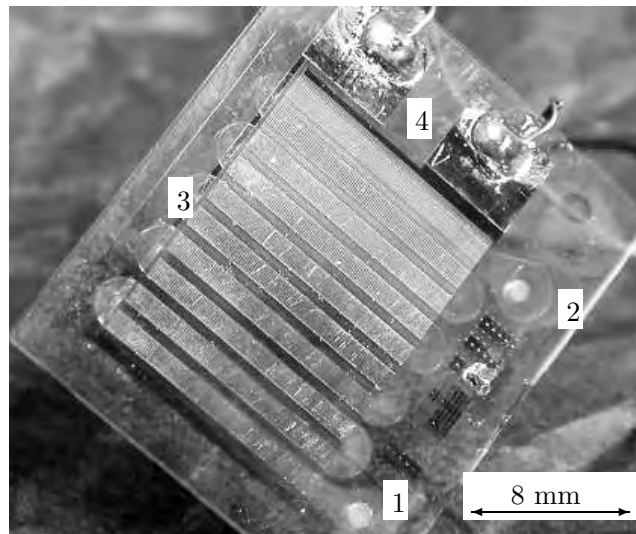


Figure 8.5: Picture of the first generation of AC EO pump developed at MIC. (1) Inlet, (2) outlet, (3) meander shaped pumping channel and (4) electrode pads. Courtesy of Morten Arnoldus and Michael Hansen.

reliable anodic glass bonding was used. The electrodes were also arranged in a more parallel manner, see Fig. 8.6. The total electrode array consists of 8 sub-arrays that each have their own power supply. In this way a sub-array can be decoupled if it is short circuited for some reason.

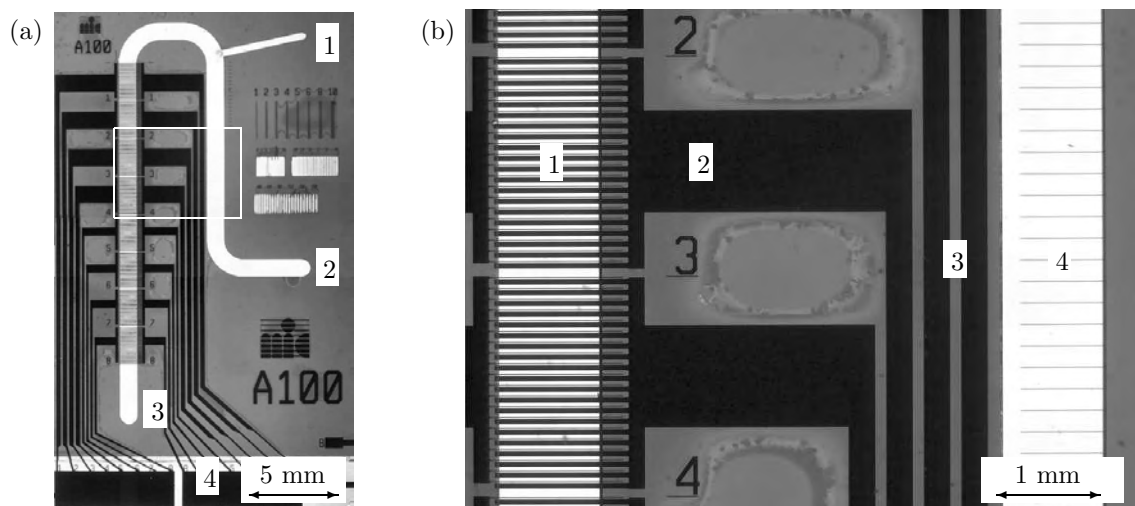


Figure 8.6: (a) Picture of the second IC EO pump generation developed at MIC. (1) Inlet to measurement channel, (2) outlet, (3) inlet and (4) electrical connection pads. (b) Magnification of the area in the white box in panel (a). (1) Asymmetric electrode array, (2-3) power supplies for the electrode sub-arrays and (4) measurement channel. Courtesy of Misha M. Gregersen.

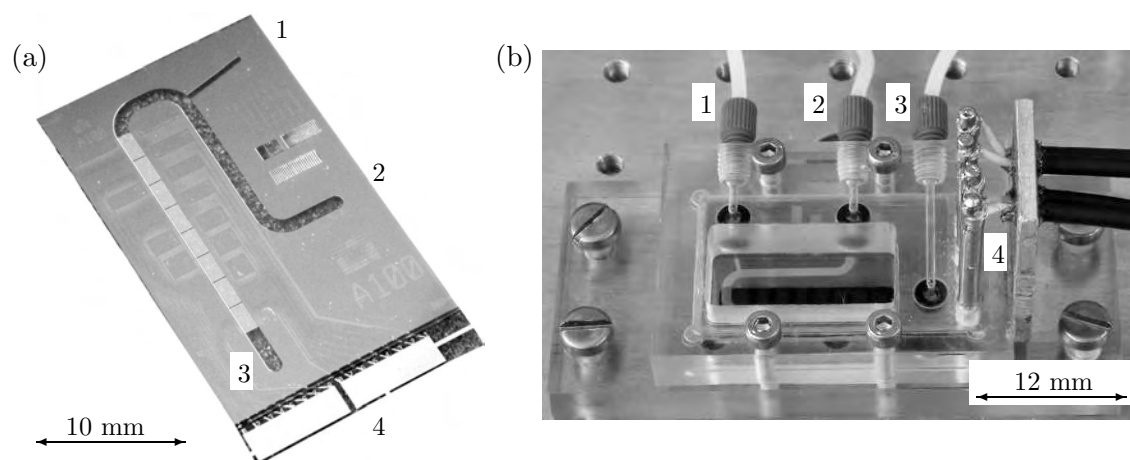


Figure 8.7: (a) Picture of the second generation of IC EO micropumps developed at MIC, courtesy of Misha M. Gregersen. (1) Inlet to measurement channel, (2) outlet, (3) inlet and (4) electrical connection pads. (b) Picture of the chip mounted in the holder. (1-3) Same as in panel (a) and (4) spring-loaded electrical contact pins.

The pump is not designed for actual pumping purposes but more for basic studies of the electrohydrodynamics of the system. The idea is to load fluorescent beads into the measurement channel, Fig. 8.6(a), and then shut of the inlet to the measurement channel while opening an external connection between the inlet and the outlet. In this way it should be possible to measure the induced velocities in the measurement channel without interference from electric fields or liquid-gas interfaces.

A chip holder was constructed, see Fig. 8.7(b). The chip holder uses O-rings to seal the three fluidic connections to the chip. The O-ring geometry is adopted from the Upchurch Nanoports, shown in Fig. 7.4(a). In this way a minimum of dead volume is introduced in the O-ring coupling which can be important when handling bead suspensions. Electrical contact is made using spring loaded contact pins. In this way no epoxy gluing of fittings or soldering of electrical wires are needed.

8.3.5 Conclusion

The work with induced-charge EO pumping (IC EO) is in progress. It is a very exciting and relatively unexplored research field. The IC EO pumping method is better suited for microfabrication than regular EO pumping because of its simple construction. The effect is, however, very weak and the pumps may be used for flow manipulation, such as mixing, rather than pumping bulk volumes. The IC EO pumping is very dependent on the conductivity of the pumped liquid which is a drawback similar to what is observed for regular EO pumping. Stability of the pump may also be a concern. In Refs. [44, 40] it is noted that operating the pump at high voltages and low frequencies damages the electrodes. However, it is still a very elegant way of pumping an electrolyte and it is my belief that it will be used in many applications in the future.

Chapter 9

Outlook and conclusion

Outlook

All of the constructed pumps presented in this thesis exist on a prototype level and operating them require careful preparation and supervision. Thus there is still room for improvements in terms of stability, performance and required maintenance. In this section some suggestions for further research/development projects are made.

The conditioning of a frit-based EO pump is very difficult, especially in the nanoporous case. Sometimes, a pump had a lower flow rate than normal although the current was the unchanged. This indicated that the surface charge had changed. A frit with a more simple and controllable pore geometry would be preferable. It would also be interesting to investigate if other materials than silica would be suitable for EO pumping. Perhaps permanently charged polymers such as those in the ion exchange membranes could be used instead of a silica frit making the EO flow less dependent on the pH value.

The total ion transport in an EO pump is also a subject to further investigations. It would be very interesting to simulate the transient and stationary ion transport during pumping. Simulation of moving pH fronts, Donnan exclusion, diffusion boundary layers etc. does, however, require a very comprehensive analysis. An experimental alternative would be to integrate different sensors inside the pump. Sensors measuring pH, conductivity and temperature could provide valuable information. A pH sensor could give information about the surface charge condition in the frit. A conductivity sensor could give information about ion depletion or accumulation and finally a temperature sensor could perhaps explain some of the long-term transients observed.

The dimensions within the pump need to be very accurate in order to achieve reproducible performance. The assembly of the pump with the flexible gaskets and wiggly ion exchange membranes can therefore be a problem. Especially, the ion exchange membranes are difficult to integrate and position reliably due to their swelling and fragile nature. A more structurally rigid ion exchange arrangement would be advantageous with respect to the control of the diffusion boundary layer width and the compliance.

Conclusion

The purpose of this thesis was to investigate the feasibility of using EO pumping technology for microsystems. Several EO based pumps have been designed, fabricated and tested. Three different operation modes have been investigated: (1) Direct current operation (DC EO), (2) low-frequency alternating current (AC EO) and (3) high-frequency induced-charge (IC EO).

DC EO pumping

In the last decade many DC EO pump designs have been reported in the literature. Our main contribution to this area is the investigation of the stability issues associated with the use of ion exchange membranes in EO pumps. It was discovered that the concept of limiting current density was important in relation to the stability. This knowledge was used to improve the stability by controlling the width of the diffusion boundary layer and thereby increase the limiting current. The control of the diffusion boundary layer was achieved through an engineered flow pattern within the pump.

The DC pump demonstrated excellent stability over several hours of operation. However, unsolved issues such as electrolysis and surface charge stability prevented true continuous operation. The DC EO pump yielded a high pressure capacity for low voltages $\Delta p_m/\Delta V = 0.15 \text{ bar V}^{-1}$, which compares with the best EO pumps developed to this date. The flow rate was approximately $Q_m = 6 \mu\text{L} (\text{min mA})^{-1}$ depending on the buffer concentration. This value is quite low compared to other EO pumps. The reason is that the Debye layers overlap in a nanoporous frit and thereby retards the flow. Increasing the ionic strength and thereby decreasing the Debye length did not help much because the EO mobility decreases at high ionic concentrations. In absolute terms the DC EO pump produced a maximum $\Delta p_m = 4.5 \text{ bar}$ and $Q_m = 6 \mu\text{L min}^{-1}$ at $\Delta V = 30 \text{ V}$.

AC EO pumping

In order to overcome some of the issues associated with DC EO pumping the novel concept of using an EO actuator in a reciprocating pump was developed. We denoted the pumping method AC EO pumping not to be confused with induced-charge EO pumping. The AC EO pumping is in fact almost DC with operating frequencies in the range $f = 10^{-3} - 10^{-1} \text{ Hz}$.

Two different AC EO pumps were developed. The switching from DC to AC was motivated by the issues with electrolysis and dependence on the pumped liquid. In the AC pump, bubble-free palladium electrodes were utilized for the first time in an EO pump. The AC pumping scheme also offers the possibility of making the pump independent on the pumped liquid. A system was constructed but only preliminary tests were performed due to lack of time. The EO actuator is capable of delivering a large stroke volume ($V_{\text{stroke}} = 1 - 10 \mu\text{L}$) with high pressure ($\Delta p = 1 - 10 \text{ bar}$). These qualities along with its low-cost make the EO actuator suited for micropumps.

The downside of AC EO pumping is the need for microvalves which introduces an extra level of complexity to the system. Two different rectifying 4-valve systems were developed: (1) A system of mobile plug valves was produced during my research stay at the

University of Michigan. The fabrication proved to be rather complex and only a few hours of true pumping were achieved during the five month project. It was only due to a very large effort in a +30 °C laboratory that I can present the following pump characteristic, $\Delta p_m = 0.55$ bar and $Q_m = 3 \mu\text{L min}^{-1}$ at $\Delta V = 30$ V and $T = 20$ s. However, the project also gave valuable information about the bubble-free electrodes and the requirements imposed on the microvalve system. (2) The rectifying polymer membrane valves proved to be excellent in terms of low opening pressure and high diodicity. The easy and fast fabrication allowed for optimization of the valve geometry and choice of membrane materials. The only disadvantage was that, due to their relatively large size and flexible nature, they introduced a significant amount of compliance to the system. In absolute terms the AC EO pump produced a maximum $\Delta p_m = 2.0$ bar and $Q_m = 10 \mu\text{L min}^{-1}$ at $\Delta V = 30$ V and $T = 90$ s. The operation was, however, slightly unreliable due to compliance and priming issues.

IC EO pumping

The final EO pumping scheme tested was the induced-charge EO pumping. IC EO is a very exciting and elegant pumping method. The method is very simplistic although the theory behind it is very complex. We have presented solutions for both utilizing and characterizing the pumping effect. The motivation behind the research effort is that the pumping method is very suitable for lab-on-a-chip technology due to the simple fabrication. The expected performance of our first IC EO pump design was $Q_m = 0.5 \text{ nL s}^{-1}$ and $\Delta p_m = 120$ Pa at $\Delta V_{\text{rms}} = 1.2$ V, $f = 2$ kHz. Unfortunately, the project was setback due to fabrication difficulties. The work with the 2nd version is in progress but the pump has already shown pumping within the expected order of magnitude.

Overall

Three different EO pumping schemes have been implemented in microfluidic devices. The main focus has been directed towards DC EO and AC EO pumping. Major advances in DC EO pumping was achieved in terms of stability. The novel concept of AC EO pumping improved the useability of the pump but it came at the cost of increased complexity. Common for the developed prototypes is that they require a lot of maintenance. Personally I had hoped to see the developed EO pumps used in other MIC devices. However, it presents a tremendous challenge to make these micropumps available to nonexpert users. The AC EO pump is the best candidate for becoming more user-friendly, e.g., the very first time I had assembled the pump it performed very well. It is my experience that EO pumping is very rugged but at the same time somewhat unstable. By that I mean that an EO pump will always work, but to a varying degree. Meticulously conditioning of the chemistry involved requires expert knowledge about electrochemistry, membrane technology and surface chemistry. Addressing these issues is one of the next steps towards a product. It is my hope that the reader of this report will have obtained a good insight into the strengths and weaknesses of EO pumping.

Appendix A

Equivalent circuit theory

In this chapter we describe how equivalent circuit theory may be used to predict the behavior of an EO actuator coupled to a rectifying 4-valve system with bubbles, i.e compliance. Simplified models for the valves and bubbles are presented. Table A.1 displays the equivalent symbols.

hydraulic		electrical equivalent	
pressure	p	voltage	U
flow rate	$Q = \frac{dV}{dt}$	current	I
resistance	$R_{\text{hyd}} = p/Q$	resistance	R
compliance	$K = \frac{dV}{dp}$	capacitance	C

Table A.1: List of equivalent sizes in electrical and hydraulic theory.

A capacitance is resistive against fast changes of voltage. In the same way a bubble will not allow the pressure to change momentarily. Volume must be moved before the pressure can change. The pump has two electrode chambers. In principle these chambers may have different compliances because the frit separates the compartments hydraulically. In any case the capacitor should be connected in parallel to the flow through the pump. The internal resistance R_p should be connected in serial. These requirements only allow one configuration, see Fig. A.1(a).

The circuit depicted in Fig. A.1(b) has five independent mask (loop) currents denoted $\mathbf{I} = I_1 \dots I_5$. The total voltage drop in a mask is zero. The five equations are shown in Eqs. (A.5)

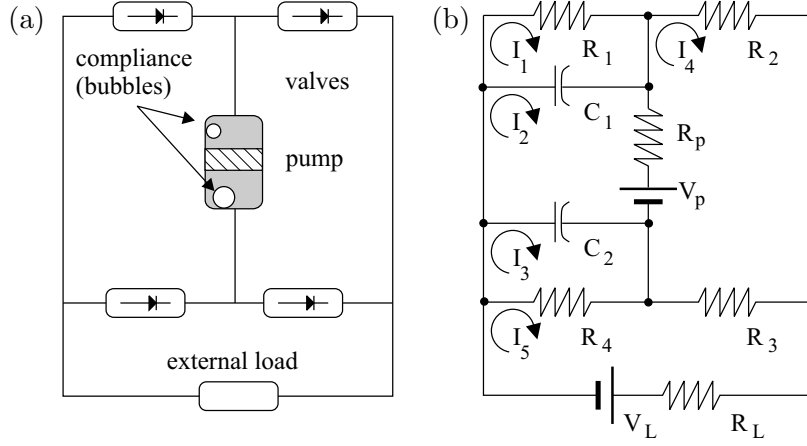


Figure A.1: (a) Flow diagram of the AC EO pump with four rectifying valves. (b) Equivalent circuit model of the system. $R_1 \dots R_4$ are the valve resistances. The internal resistance of the pump is given as $R_p = \Delta p_m / Q_m$. R_L and V_L is the external load. C_p is the compliance of a bubble. Mask current $I_5 = I_L$ is also the current through the load.

$$I_1 R_1 + \int (I_1 - I_2) C_1^{-1} dt = 0 \quad (\text{A.1})$$

$$\int (I_2 - I_1) C_1^{-1} dt + (I_2 - I_4) R_p + V_p + \int (I_2 - I_3) C_2^{-1} dt = 0 \quad (\text{A.2})$$

$$\int (I_3 - I_2) C_2^{-1} dt + (I_3 - I_5) R_4 = 0 \quad (\text{A.3})$$

$$I_4 R_2 + (I_4 - I_5) R_3 - V_p + (I_4 - I_2) R_p = 0 \quad (\text{A.4})$$

$$(I_5 - I_3) R_4 + (I_5 - I_4) R_3 + I_5 R_L + V_L = 0 \quad (\text{A.5})$$

In order to avoid the integral formulation Eqs. (A.5) may be differentiated with respect to time. This gives a system of five linear 1st order ordinary differential equations (ODE's).

$$\begin{bmatrix} R_1 & 0 & 0 & 0 & 0 \\ 0 & R_p & 0 & -R_p & 0 \\ 0 & 0 & R_4 & 0 & -R_4 \\ 0 & -R_p & 0 & R_2 + R_3 + R_p & -R_3 \\ 0 & 0 & -R_4 & -R_3 & R_4 + R_3 + R_L \end{bmatrix} \frac{d\mathbf{I}}{dt} = \begin{bmatrix} (I_2 - I_1) C_1^{-1} \\ (I_1 - I_2) C_1^{-1} + (I_3 - I_2) C_2^{-1} - \dot{V}_p \\ (I_2 - I_3) C_2^{-1} \\ \dot{V}_p \\ -\dot{V}_L \end{bmatrix} \quad (\text{A.6})$$

The differential equations are coupled which means that the equations must be solved simultaneously. We denote the left-hand side of Eq. (A.6) the mass matrix, $\mathbf{M}(t, \mathbf{I})$. The right-hand side of Eq. (A.6) is the forcing term $\mathbf{f}(t, \mathbf{I})$. In short form we may write Eq. (A.6) as

$$\mathbf{M}(t, \mathbf{I}) \frac{d\mathbf{I}}{dt} = \mathbf{f}(t, \mathbf{I}) \quad (\text{A.7})$$

$$\text{if } \det(\mathbf{M}(t, \mathbf{I})) \neq 0 \Rightarrow \quad (\text{A.8})$$

$$\frac{d\mathbf{I}}{dt} = \mathbf{M}(t, \mathbf{I})^{-1} \mathbf{f}(t, \mathbf{I}) \quad (\text{A.9})$$

The mass matrix is state dependent and hence needs to be solved for each time step. This makes the system nonlinear and is caused by the flow dependent resistors, i.e. valves. A MATLAB routine was written to solve the problem. Some preliminary results are shown in Fig. A.3.

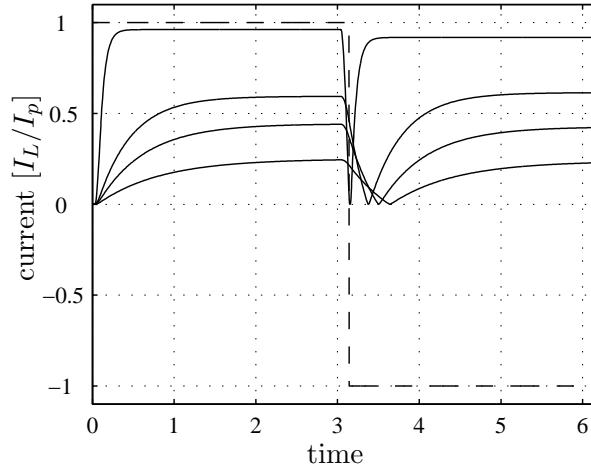


Figure A.2: Current through the external load I_L/I_p as function of R_L/R_p . The terminology is kept electrical. The dashed curve is $I_p = V_p/R_p$ while the solid curves are I_L/I_p . The driving voltage V_p is a square wave with $T = 2\pi$. The internal resistance of the pump is R_p and capacitances are set equal $C_1 = C_2$. The characteristic time $\tau = RC$ varies with the different R_L imposed in the range $0 < R_L < R_p$. The compliance is visible for the high load. Valves are modelled as flow dependent resistors, i.e., $R_{\text{open}} = 10^{-2} R_p$ for $I > 0$ and $R_{\text{closed}} = R_p$ for $I < 0$.

The valves are here modelled as flow dependent resistors. The valves can be described by different resistance models. In the above model we used the two-parameter model from Fig. A.3(b).

The compliance of the system may come from many places. Bubbles in the electrode chamber is largest compliance contributor. For an isothermal expansion

$$p_b \mathcal{V}_b = p_i \mathcal{V}_i \quad (\text{A.10})$$

$$\mathcal{V}_b = \mathcal{V}_i (p_i/p_b) \quad (\text{A.11})$$

$$\mathcal{V}_{\text{sys}} = \mathcal{V}_{\text{res}} - \mathcal{V}_b \quad (\text{A.12})$$

where p_b and \mathcal{V}_b is the actual pressure and volume of the bubble while p_i and \mathcal{V}_i was the initial pressure and volume. Eq. (A.11) displays the volume of the bubble as function of the external pressure when we neglect the surface tension. The volume of the system \mathcal{V}_{sys}

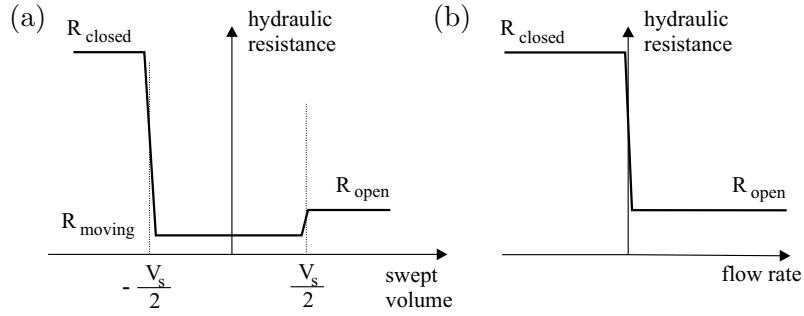


Figure A.3: Two different models for the valve resistance. (a) Valve resistance as function of swept volume. The switch volume of the valve is \mathcal{V}_s . This model operates with three different resistances. (b) If the switch volume is negligible the model can be simplified to a simpler two resistance model as function of flow rate instead of swept volume.

is the volume of the reservoir V_{res} minus the volume of the bubble V_b . The compliance is given as

$$K = \frac{d\mathcal{V}_{\text{sys}}}{dp} = -\frac{dV_b}{dp} = \mathcal{V}_i \frac{p_i}{p_b^2}, \quad (\text{A.13})$$

where the reservoir volume is assumed to be constant. The system expands when the bubble compresses. Note also that the bubble induced compliance is depending on the pressure.

This modelling showcase illustrates that it is possible to expand a the equivalent circuit theory to include more advanced flow components such as pumps, valves and bubbles.

Appendix B

Experimental setup

In this chapter we discuss some of the experimental setups that were constructed during the project. In the DC and AC EO pump projects the electrical circuit for driving the pumps was the same. The required voltage and current capacity was $\Delta V = \pm 30$ V and $I = 100$ mA respectively.

The system is controlled by a 16-bit data acquisition card from National Instruments, Austin, TX, USA. The DAQ card has two analog outputs (AO) in the range $V = \pm 10$ V and eight analog inputs (AI) in the same range. The DAQ card was connected to a terminal box through a shielded cable. A 2×31 V power supply was used together with an custom fabricated $3\times$ -amplifier based on a high quality operation amplifier, see Fig. B.1. This $3\times$ -amplifier was later used together with a lock-in amplifier for the high-frequency induced-charge EO pump. The output voltage ΔV is divided by a factor 11 before the signal is directed to AI to prevent overloading. The electrical current I is measured by a passing the current through a small resistance $R_i = 110$ Ω . A typical current of 1 mA gives a voltage feed of $V_i = 110$ mV. The electrical resistance of the pump is roughly $R_p = 30$ k Ω . The error of having R_i in series is small because R_i is negligible compared to R_p , ($R_p/R_i = 270$). The LABVIEW front panels can be seen in Figs. B.2 and B.4.

The pressure sensors are from Honeywell 40PC150G1A, Freeport, IL, USA. Their range is from 0 – 10 bar and they have built-in signal amplification. They require a 5 V power supply and have a linear output between 0.5 – 4 V depending on the pressure. Mounting of the sensors is discussed in Sec. 6.3.

The balance used is a 0.1 mg precision Sartorius CP224S, Goettingen, Germany, see Fig. B.3. The load range is 0 – 220 g and the absolute precision should be same within the whole range. Communication with the balance is done using the RS232 port with a custom PC serial port cable. Text strings are sent, received and interpreted via the LABVIEW interface, see Fig. B.5. A balance is typically used for weighing objects with a constant mass. This means that the readout is damped in order to obtain fast readouts after a change in the load on the balance. For flow rate measurements this damping or stabilizing algorithm is unwanted because it limits the temporal resolution. In the CP224S it is possible to adjust the level of damping. The setting should be set towards fast release (low damping).

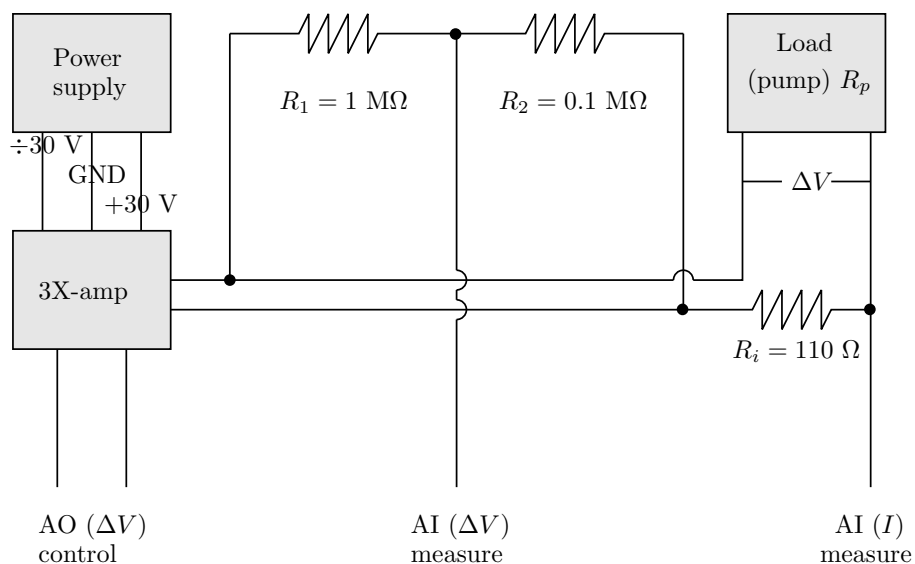


Figure B.1: Diagram of the electrical setup. The applied voltage ΔV can be controlled from the data acquisition card. The applied voltage ΔV is set through the analog output (AO). The applied voltage ΔV and current I signals are conditioned before they are measured with the analog inputs (AI).

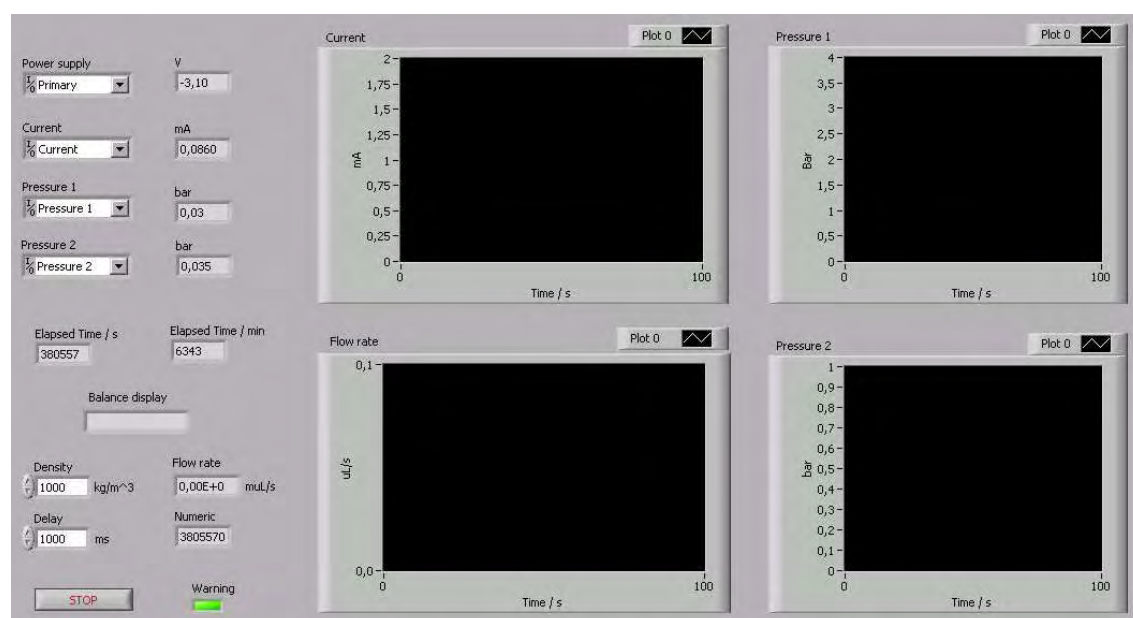


Figure B.2: The LABVIEW front panel used in the DC EO pump experiments. The voltage is kept constant while the current and flow rate are monitored. The upstream and downstream pressure are also monitored.



Figure B.3: Picture of the setup for measuring hydraulic resistance. The equivalent flow diagram is identical to that in Fig. 5.6 but without the switching valves (1-4). In this picture a chip holder similar to that in Fig. 8.7(b) is inserted between the pressure sensors.

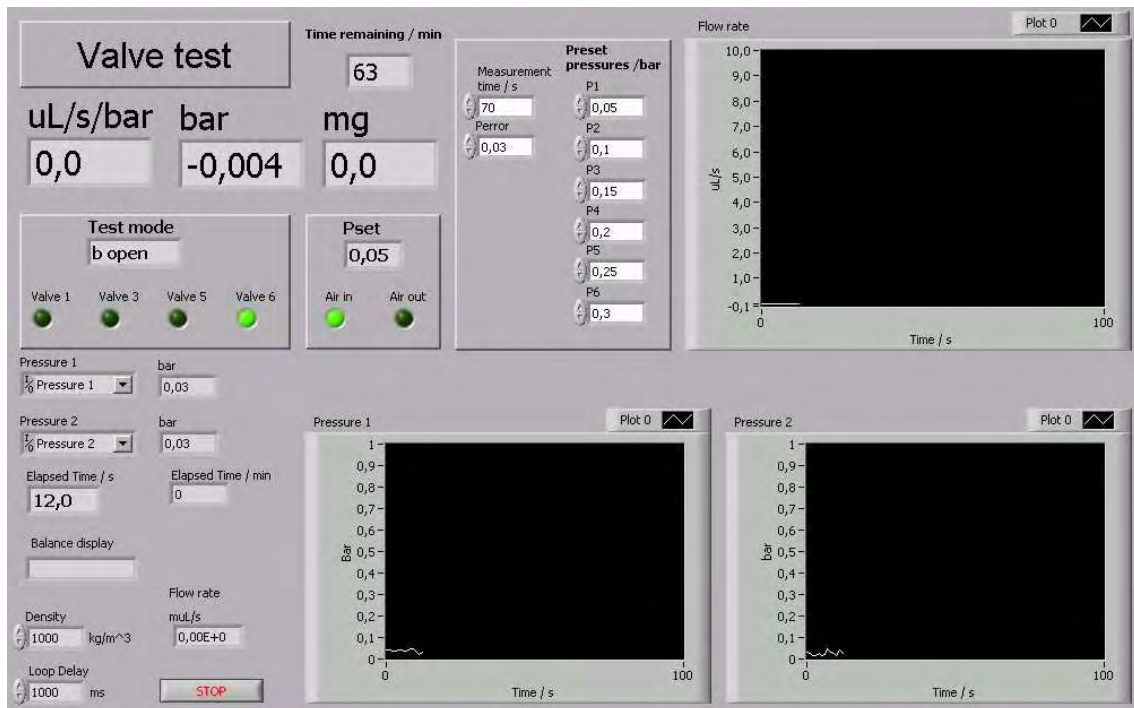


Figure B.4: The LABVIEW front panel used in the automated 4-valve testing. The test mode panel indicates which valve is being tested. The Pset panel indicates the target pressure for the measurement. The measurement time, sequence of target pressures and pressure tolerance can be set manually. The source code is shown in Fig. B.4.

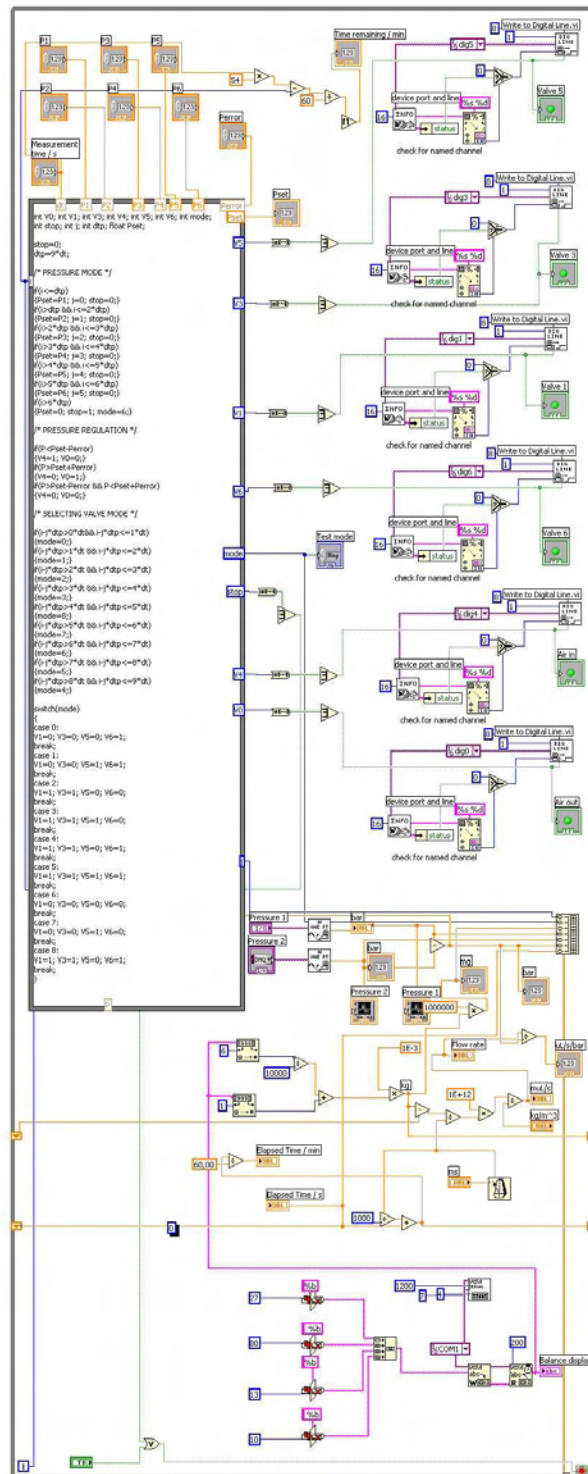


Figure B.5: Layout of the LABVIEW program controlling the valve testing. The pressure regulation and switching of the valves is coded in C-language. The corresponding front panel can be seen in Fig. B.4

Appendix C

Paper published in J. Micromech. Microeng.

Title

A novel electroosmotic pump design for nonconducting liquids:
theoretical analysis of flow rate-pressure characteristics and stability

Authors

Anders Brask, Goran Goranović, Mads Jakob Jensen and Henrik Bruus

Reference

J. Micromech. Microeng., (2005), **15**, 883-891.

A novel electro-osmotic pump design for nonconducting liquids: theoretical analysis of flow rate–pressure characteristics and stability

Anders Brask, Goran Goranović, Mads Jakob Jensen
and Henrik Bruus

MIC—Department of Micro and Nanotechnology, Technical University of Denmark,
Oersteds Plads, Bldg. 345 East, DK-2800 Kgs. Lyngby, Denmark

E-mail: abr@mic.dtu.dk

Received 30 November 2004, in final form 26 January 2005

Published 11 March 2005

Online at stacks.iop.org/JMM/15/883

Abstract

We present the design and theoretical analysis of a novel electro-osmotic (EO) pump for pumping nonconducting liquids. Such liquids cannot be pumped by conventional EO pumps. The novel type of pump, which we term the two-liquid viscous EO pump, is designed to use a thin layer of conducting pumping liquid driven by electro-osmosis to drag a nonconducting working liquid by viscous forces. Based on computational fluid dynamics, our analysis predicts a characteristic flow rate of the order nL/s/V and a pressure capability of the pump in the hPa/V range depending on, of course, achievable geometries and surface chemistry. The stability of the pump is analyzed in terms of the three instability mechanisms that result from shear-flow effects, electrohydrodynamic interactions and capillary effects. Our linear stability analysis shows that the interface is stabilized by the applied electric field and by the small dimensions of the micropump.

1. Introduction

Electro-osmotic (EO) pumps are suitable for microfluidic applications due to their integrability and compatibility with conventional microtechnology, and moreover they can produce a pulse-free flow without containing any moving parts [1–3]. In EO pumps a liquid is pumped by applying an electric field to the Debye layer. This is formed by the ions in the liquid due to electric screening of the immobile charges on the walls of the pump. In order for such a Debye layer to form, the liquid needs to have significant electrical conductivity, i.e., a sufficiently high concentration of dissociated ions. Nonpolar liquids with very low conductivity ($<10^{-6}$ S m $^{-1}$), such as oil, cannot form the necessary double layer and therefore cannot be pumped in this way [4]. However, as analyzed below, this problem is circumvented in our design by introducing a conducting secondary liquid. By presenting our design and the theoretical analysis of it, we hope to inspire experimental groups to test our ideas and fabricate a device.

The paper is organized in the following way. In section 2, we introduce the general concept of the pump and its novel features. In sections 3 and 4, we turn to a particular, realizable pump geometry and analyze it in terms of flow rate–pressure (Q – p) characteristics by means of CFD simulations and equivalent circuit theory. Then, in section 5, we assess the stability of the pump by performing a linear stability analysis of the two-liquid interface. Finally, we draw conclusions in section 6.

2. General concept

There are two main types of inline EO pumping schemes in use today. In direct EO pumping, [5, 6], electrodes are in direct contact with a conducting buffer. The buffer enables both the driving force in an electric field, and, due to the charge separation at the walls of a channel, also a bulk-liquid motion, the actual electro-osmotic flow.

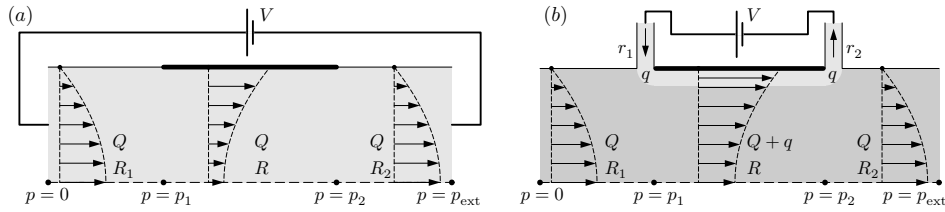


Figure 1. (a) The top half of a symmetric channel containing a conducting liquid (light gray), where the EO mobility on the top wall changes step-wise from zero (thin line) in the first section to α_{eo} (thick line) in the middle section and back to zero (thin line) in the last section. The pressure drops and hydraulic resistances in the three sections are $0 - p_1$ and R_1 , $p_1 - p_2$ and R , and $p_2 - p_{ext}$ and R_2 , respectively. The flow profile is shown in each of the sections of panel (a), but in addition a conducting pumping liquid (dark gray) of flow rate q enters and exits through two side-channels with hydraulic resistances r_1 and r_2 . In both panels are shown the applied voltage V that generates the EO flow. The symmetry plane is indicated by the dashed horizontal line in the bottom.

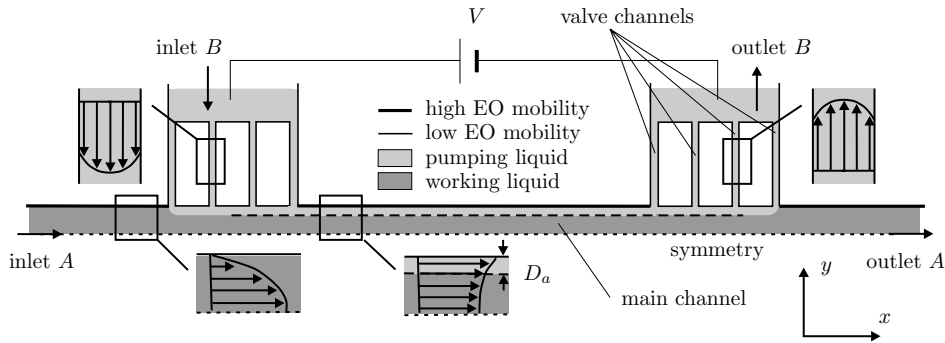


Figure 2. Top view of a possible design of the two-liquid viscous pump. The nonconducting working liquid (dark gray) is being dragged by the EO-driven pumping liquid (light gray) that flows along the edge of the main channel. The pump is mirror-symmetric around the central vertical plane, and only one half is shown. The following specific parameters are chosen to predict the performance of the pump. The displayed microchannels are all $40 \mu\text{m}$ deep. The main channel where the working liquid flows is $150 \mu\text{m}$ long and $10 \mu\text{m}$ wide. The narrow valve channels are $1 \mu\text{m}$ wide and $42 \mu\text{m}$ long. The un-coated walls are marked as the thick edges of the main channel. Coated walls are marked with thin edges. In inlet A and outlet A the flow is parabolic, while in the valves and in the main channel it is a superposition of parabolic and an EO-induced plug flow.

In the so-called indirect EO pumping the liquid in which the electrodes are separated by some barriers from the liquid where the EO flow takes place. The barriers allow ions but not bulk liquid to pass from the electrode chamber to the EO flow region. The barriers between the two regions can be achieved in several ways. (i) A channel filled with a conducting gel with a large hydrodynamic resistance [2]. (ii) An ion-exchange membrane allowing only positive or negative ions to pass [3]. (iii) A nanometer-sized gap (to allow for the Debye layer overlap) in which bulk EO flow can be suppressed allowing practically only flow of ions [7]. Common for these separation methods is that they are based on the Donnan exclusion principle.

Our novel two-liquid viscous pump can be regarded as a hybrid of the two types of EO pumping. There is still a direct contact between the driving and the bulk layers but they now originate from two different liquids. EO flow is used indirectly as it drives layers of conducting secondary liquids, introduced from some side-channels, to pump a nonconducting liquid through the main channel by viscous forces, see figure 1. Such an arrangement, resembling a conveyor belt, allows the pump to be conveniently positioned anywhere within a microfluidic circuit. To our knowledge it is the only EO pumping mechanism that enables inline pumping of nonconducting liquids. In the following subsections we highlight general principles for the operation of the pump:

pressure valves, under-pressure induced by spatial variations in EO mobility and optimized potential drop. These principles are sketched in figure 2.

2.1. Ideal EO flow and pressure valves

In the case of an infinitely thin Debye layer the EO flow rate in a rectangular microchannel of length L , height D , and width a is given by

$$Q_{eo} = u_{eo} Da = \alpha_{eo} V_{eff} \frac{Da}{L} \propto a. \quad (1)$$

Here u_{eo} is the electro-osmotic velocity, α_{eo} is the electro-osmotic mobility and V_{eff} is the electric potential drop inside the channel. We refer to this situation as ideal EO flow. The associated EO pressure p_{eo} is given by

$$\Delta p_{eo} = Q_{eo} R_{hyd} = \alpha_{eo} V_{eff} \frac{aD}{L} R_{hyd}. \quad (2)$$

For high aspect ratios $D \gg a$, the hydraulic resistance is

$$R_{hyd} = \frac{12\mu L}{a^3 D} \frac{1}{1 - 0.63 \frac{a}{D}}, \quad (3)$$

where μ is the dynamic viscosity. The pressure-driven flow rate Q_p through the channel is given by

$$Q_p = \frac{\Delta p}{R_{hyd}} \propto a^3, \quad (4)$$

where Δp is the pressure drop along the channel.

From equations (1) and (4) it follows that the pressure-driven flow will be negligible compared to the EO flow for small values of a . This can be used to obtain a kind of pressure valves in the two-liquid viscous pump: if narrow channels are placed on the sides of the main channel, their large hydraulic resistance prevents a significant loss of the pressure from the pump into the sides, while at the same time allows the driving EO flow to pass through them. The pressure valves offer two additional advantages. The electrode reservoirs separated by the valves can be exposed to atmospheric pressure. Thus bubble formation from electrolysis will not enter the pump and cause problems. Furthermore, this allows for placing the pump anywhere in a fluidic network.

2.2. Under-pressure due to changes in EO flow rate

In order for a nonconducting liquid to enter the pump an under-pressure needs to be induced at the entrance of the pump. This can be achieved by allowing for spatial variation in the EO flow rate Q_{eo} . Mass conservation ensures that the total flow rate $Q = Q_{eo} + Q_p$ is constant, so a change in Q_{eo} implies a change in Q_p and hence a change in pressure. The change in Q_{eo} can be obtained either by variations in the EO mobility or by variations in the channel width a large enough to induce a varying degree of the Debye layer overlap. In this paper we will focus on the first method.

The EO flow given in equation (1) corresponds to a constant EO mobility, in which case no under-pressure is generated inside the channel. If, however, the EO mobility is allowed to change along the channel, a more complex pressure field is obtained. To simplify the discussion without losing the main physics, we study the three-section channel shown in figure 1(a), where the EO mobility changes from zero to α_{eo} and back to zero. It is the inhomogeneity of the EO mobility that is important, not its specific functional form. The hydraulic resistances of the three sections are R_1 , R and R_2 , respectively. The pressure changes from 0 to p_1 , from p_1 to p_2 , and from p_2 to p_{ext} along the first, second and third section, respectively. Thus the EO pump is set up to work against an external backpressure p_{ext} . The expressions for the total constant flow rate Q in each of the three sections are

$$Q = \frac{(0 - p_1)}{R_1} = \frac{(p_1 - p_2)}{R} + Q_{eo} = \frac{(p_2 - p_{ext})}{R_2}. \quad (5)$$

By straightforward algebra this yields

$$Q = \frac{RQ_{eo} - p_{ext}}{R_1 + R + R_2}, \quad (6)$$

$$p_1 = \frac{R_1}{R_1 + R + R_2}(p_{ext} - RQ_{eo}), \quad (7)$$

implying that a positive flow rate will be induced once RQ_{eo} is larger than the backpressure p_{ext} . Moreover, an under-pressure p_1 is induced over the first section of the pump, which ensures that liquid is sucked into the pump.

In figure 1(b) this principle of generating an under-pressure is applied to the two-liquid viscous pump. We study the case of immiscible liquids with a stable interface pinned at the corners of the side-channels. In this case the individual flow rates of the pumping and working liquids are constant. For the sake of simplicity we neglect the curvature effects due

to surface tension and postpone this study until sections 4.1 and 5.

The nonconducting working liquid (dark gray) enters the first section of the large, three-section main channel of the hydraulic resistance R_1 and leaves the section of the hydraulic resistance R_2 with the same flow rate Q given by

$$\frac{1}{R_1}(0 - p_1) = Q, \quad \frac{1}{R_2}(p_2 - p_{ext}) = Q. \quad (8)$$

The conducting pumping liquid (light gray) enters with the flow rate q through the inlet side-channel having the hydraulic resistance r_1 , and exits with the same flow rate q through the outlet side-channel having the hydraulic resistance r_2 . Since we are neglecting the Young–Laplace pressure drops from the curved interfaces the pressures p_1 and p_2 are as above, and the flow rate q is seen to be

$$\frac{1}{r_1}(0 - p_1) = q, \quad \frac{1}{r_2}(p_2 - 0) = q. \quad (9)$$

In the active part of the pump, the middle section with the hydraulic resistance R , the expression for the total flow rate is simplified, if we assume that the two liquids have the same viscosity (this assumption is easily relaxed in numerical simulations):

$$\frac{1}{R}(p_1 - p_2) + Q_{eo} = Q + q. \quad (10)$$

The expressions for Q , p_1 and q become

$$Q = \frac{RQ_{eo} - p_{ext}}{R_1 + (1 + \frac{R_1}{r_1})R + R_2}, \quad (11)$$

$$p_1 = -R_1Q, \quad (12)$$

$$q = \frac{R_1}{r_1}Q. \quad (13)$$

Like for the simple channel equation (6), a positive flow rate Q appears once $RQ_{eo} > p_{ext}$, and in this case an under-pressure p_1 is generated thus making it possible to suck the nonconducting working liquid into the EO pump. A simulation of the induced under-pressure in the regions below the pressure valves is shown in section 4. In the limit of very high resistance of the side-channel, $r_1 \gg R_1$, equation (11) reduces to equation (6). Note, that because we have neglected the Young–Laplace pressure drops, and assumed a stable interface, the external pressure is fixed to be $p_{ext} = [R_1(r_2/r_1) - R_2]Q$. Once the full dynamics of the free interface is introduced, the interfaces will adjust its shape to a given p_{ext} , see section 4.1.

As mentioned, a favorable under-pressure can also be achieved for constant EO mobility by reducing the cross section of the valve region compared to the main channel if the reduction is so large that the Debye layer overlap occurs. The overlap will reduce the EO velocity in the valves and change the flow profile from a plug-like to a parabolic-like one [8]. Since typically the Debye layers are 1–100 nm wide, the pressure valves in this case consist of nanochannels. Depending on the fabrication techniques, the nanochannels can be realized as channels with very high aspect ratio [9], very shallow channels [4], or as parts of nanoporous frits [10].

Regardless of the pump realization, the flow profiles will have some common characteristics. Due to the induced pressures the valve regions and the inlet/outlet regions of the

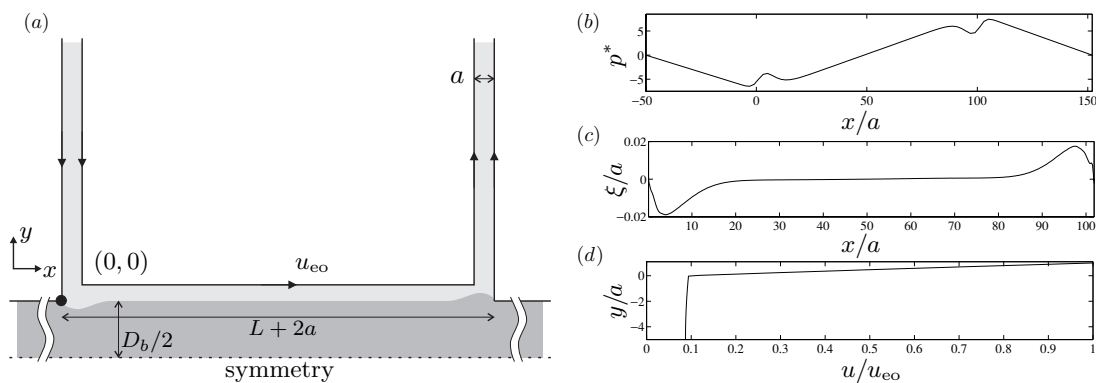


Figure 3. (a) The geometry used in the simulation of the immiscible case, where edges with arrows indicate an EO slip velocity $u_{eo} = 2\text{ mm s}^{-1}$, (b) The pressure $p = p^* \mu_{\text{cond}} u_{eo}/a$, (c) the interface position ξ and (d) velocity profile across the channel. Viscosities are $\mu_{\text{cond}} = 1.0 \times 10^{-3} \text{ Pa s}$ and $\mu_{\text{noncond}} = 300 \times \mu_{\text{cond}}$. The pressure is plotted along the symmetry axis. The deflection of interface is multiplied by a factor 100 for the purpose of visualization. The velocity profile is taken along $x = L/2 + a$.

main channel of the pump will have parabolic flow profiles. In the active part of the main channel the resulting flow is a superposition of an EO flow and an adverse pressure-driven flow, the latter resulting from the mass conservation given in equation (10). Schematic flow profiles are shown in figures 1(b) and 2, while a simulated one is shown in figure 3.

2.3. Optimized potential drop

A larger potential drop is needed in the main channel of the pump as compared to the valves in order to generate a higher pressure, equation (2). A single narrow valve channel has a large flow resistance but also a large electrical resistance. This means that the main potential drop would occur in the valve channels and thus not contribute to any pressure build up. The electrical resistance is inversely proportional to the area of the cross section. So, by making many short and narrow channels a low electrical resistance and high hydraulic resistance is obtained. However if the potential drop in the main channel is too large, it could cause instabilities of the two-liquid interface, see section 5.

2.4. Priming of the pump

In order for the pump to work an initial positioning of the liquid streams must be taken care of. This is termed as priming of the pump. The priming could happen in different ways depending on the viscosities, surface tensions and the surrounding fluidic network. One way of doing it would be to apply a pressure-driven flow to the side-channels q and the main channel Q simultaneously. This would generate a stream of focused nonconducting liquid along the main channel. If the driving pressures are then relaxed at the same time, the interface moves to the pinning points on the side-channels. Computer simulations or experiments may suggest other methods.

3. An example of a possible realization

A possible realization with realistic length scales of the two-liquid viscous pump is shown in figure 2. Two sets of four narrow channels are introduced from each side of the main channel as pressure valves. In figure 2 only one side with

inlet/outlet valves is shown, since the device is symmetric around the center plane. Reactive ion etching systems can deliver narrow and deep channels with the aspect ratio as high as 40. So if a valve channel is $1 \mu\text{m}$ wide it can be $40 \mu\text{m}$ deep. The overall hydraulic resistance of the valves, equation (3), is 26 times larger than that of the EO section.

The Reynolds number is $Re \sim 0.01$ and in this creeping flow regime inertia can be neglected. A characteristic feature for creeping flow is that it is free of vorticity. This means that the valve channels may be positioned perpendicular to the main channel without generating any eddies. For a more detailed discussion see [11].

The Debye layer is roughly 10^4 times smaller than the total width of the main channel so we do not resolve it in the following modeling of the pump. The EO velocity appears simply as a nonzero slip velocity u_{eo} at the walls. The reduced EO flow in the valves is, therefore, realized by a reduction in the EO mobility as discussed in section 2.2.

4. Theoretical and computational analysis

We have analyzed the performance of the pump described in section 3 using computational fluid dynamics (CFD) simulations and equivalent circuit theory.

4.1. Computational fluid dynamics

The simulation effort is divided into two parts: (1) simulations with immiscible liquids, simplified geometry, free surface and velocity boundary conditions, and (2) simulations with miscible liquids, full geometry and EO mobility boundary conditions.

The problem depicted in figure 2 is simulated including the full free surface dynamics. The model is based on the FemLab 3.1 FEM solver and an in-house MatLab based free surface code [12]. The model solves the 2D Stokes equation while enforcing the full free surface stress condition including the Young–Laplace contribution to the pressure. As the problem is very complex only two side-channels are considered, in order to reduce computational time, which still ended to be of the order 24 h on a high performance computer. At the

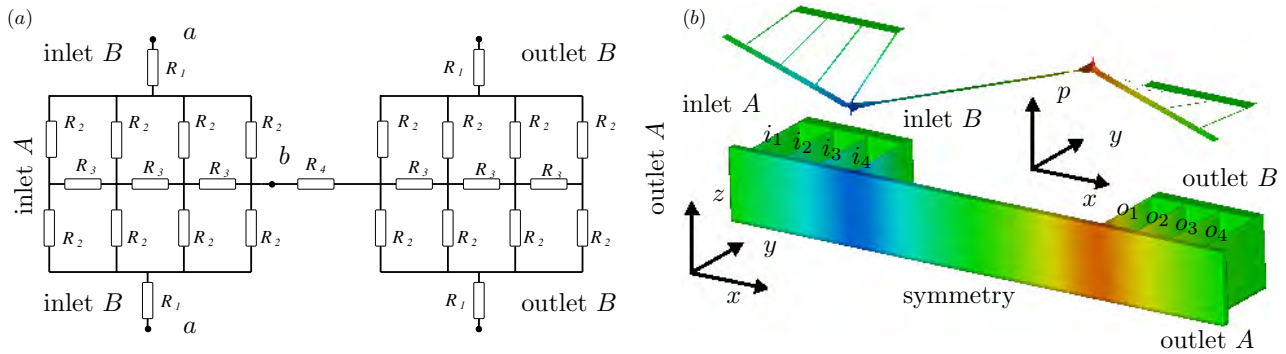


Figure 4. (a) The equivalent electric circuit of the two-liquid viscous EO pump. Note that the whole pump/circuit is depicted. The overall resistance is calculated as $R_{\text{total}} = 2R_{\text{ab}} + R_4$, where R_{ab} is the resistance between node point a and b . R_4 is the resistance of the EO section. (b) The calculated pressure distribution inside the pump obtained by numerical simulation in the miscible case with the uniform viscosity $\mu = 1 \times 10^{-3}$ Pa s. The inset floating above the pump shows how the pressure varies linearly in the main channel between the pressure valves, implying uniform flow. There is no external pressure difference, but note the pressure drop in the pressure valve region ($i_1 - i_4$) which sucks the working liquid into the main channel. Parameters: the dimensions are as in figure 2, while $\alpha_{\text{eo}}^{\text{low}} = 0.005 \text{ mm}^2 \text{ V}^{-1} \text{ s}^{-1}$, $\alpha_{\text{eo}}^{\text{high}} = 0.05 \text{ mm}^2 \text{ V}^{-1} \text{ s}^{-1}$, $p_{\text{in}} = p_{\text{out}} = 0$, $V = 10$ V. The peak pressure levels are $p = \pm 10$ Pa.

walls we use velocity boundary conditions to account for the electro-osmotic effects. Figure 3 depicts the simulated geometry with boundary conditions.

The insets (a), (b) and (c) in figure 3 show the dimensionless pressure p^* along the symmetry axis, the interface position ξ , and a velocity profile along the vertical symmetry line, respectively. From the results we see that the interface is only slightly deformed and has a thickness comparable to the inlet valve dimensions. The curved shape is a result of the pressure balance including the Young–Laplace pressure. Moreover, we notice that the slip velocity at the interface is about 10% of the wall velocity.

CFD simulations with miscible liquids were made using Coventor 2001.3. The program solves the Laplace equation for the electrical potential and the Navier–Stokes equation for the velocity field. These simulations are complementary to the more complicated free surface simulations. If the pumping liquid is chosen to be water the EO mobility along un-coated walls is typically $\alpha_{\text{eo}} = 0.05 \text{ mm}^2 \text{ V}^{-1} \text{ s}^{-1}$. In the valve channels the walls are coated to lower the EO mobility by a factor 10. With these parameters numerical simulations yield a maximal flow rate per volt of $0.03 \text{ nL s}^{-1} \text{ V}^{-1}$ and a backpressure capacity of 3 Pa V^{-1} . The value for the flow rate is specific for the given geometry. According to equations (2) and (3) the backpressure is independent of the length of the pump but strongly dependent on the width of the main channel and the viscosities in the two liquid case. Visualization of the pressure distribution is shown in figure 4(b). Note the under-pressure in the region between valve i_1 and i_4 . The pressure distribution from the immiscible (figure 3(a)) and the miscible case (figure 4(b)) agree qualitatively. Note, that in the miscible case the liquids will mix due to diffusion. Two time scales are involved: (1) the time it takes for the liquid to pass through the pump $T_{\text{pump}} = L/u_{\text{eo}}$, (2) and time it takes for the two miscible streams to mix $T_{\text{diff}} = D_b^2/D$, where D is the diffusion constant. The ratio $T_{\text{pump}}/T_{\text{diff}} = 1.5$ indicates that the liquids will be completely mixed downstream of the pump.

4.2. Equivalent circuit model

The aim is to establish a model that can predict the Q – p characteristic of the pump. The creeping flow regime allows us to analyze the flow by the equivalent circuit method. We only give an outline here as the detailed procedure is described in [13].

The first step is to find the effective potential drop across the EO section by analyzing the circuit in figure 4(a). In the miscible case with uniform conductivity the result is that 52% of the applied voltage is dropped over the EO section, R_4 in figure 4(a). This value represents a worst case since the main channel is full of conducting liquid leading to a lower voltage drop. In the immiscible case the analysis is complicated by the fact that the resistance R_4 is dependent on the position of the free interface, and an exact result is not obtainable due to lack of computational power. However, our simulations in the two-channel case, section 4.1, indicate that the width of the conducting layer is the same as the width of the side-channels. Since most of the electric field is inside the conducting layer, it is easy to obtain a rough estimate, and we find that 90% of the voltage is dropped over the EO section.

The next step in the equivalent circuit model procedure is to find the hydraulic resistance R_{hyd} of each of the channel segments. Since the channel cross sections are all rectangular we make use of equation (3). We then find the backpressure analogous to the treatment in section 2.2.

5. Stability analysis

The interface between the two immiscible liquids in the two-liquid viscous pump is generally prone to instabilities. Small perturbations can grow and eventually break-up the surface and disrupt the pumping operation. As sketched in figure 5 there are altogether three types of instability mechanisms at play: shear-flow, electrohydrodynamic and capillary instability. In the following we shall describe and assess the most relevant aspects of each mechanism.

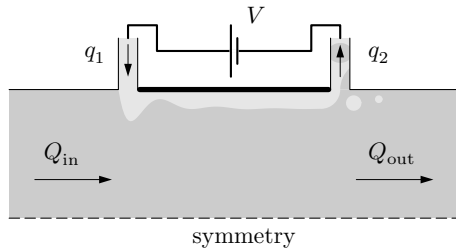


Figure 5. A schematic diagram of instabilities in the two-liquid viscous pump. Three main mechanisms of instability are at play: shear-flow and electrohydrodynamic instability are relevant in the main channel and in the outlet valve, while capillary instability plays a role below the valves where the interface curves to compensate for the induced pressures. In the case of break-up of the interphase q_1 and q_2 as well as Q_{in} and Q_{out} may differ in contrast to the case of figure 1(b).

5.1. Approximations and methods

As long as the conducting layers are thin compared to the nonconducting region, the (in)stability modes on the two interfaces of the symmetric pump from figure 2 will be decoupled from each other. In addition, the symmetric pump can sustain larger adverse pressures known to stabilize the flow [14]. Thus, it suffices to determine the instability window of the simpler asymmetric configuration containing only one interface, i.e., a pump with only one conveyor belt. We further notice that for the high aspect ratio channels under consideration the problem is effectively reduced to two dimensions.

Perturbations of the interface are assumed to be small, and we subject the governing equations and boundary conditions to the usual hydrodynamic linear stability analysis, [15]. The unperturbed interface lies in the xy plane given by $z = 0$. Any slight disturbance of the interface is described as a displacement $z = \zeta(x, y)$. We expand all perturbed field f (velocity \mathbf{u} , pressure p , electric potential ϕ and vector \mathbf{n} normal to the interface) in terms of the small interface position ζ

$$f = f_0 + \alpha f_1 + \alpha^2 f_2 + \dots, \quad (14)$$

where f_0 represents the unperturbed steady-state solution, α is the perturbation strength, and f_1 is the first-order solution. Putting the perturbed variables f into the governing equations and boundary conditions, the steady-state solution cancels out, and by maintaining only terms up to linear order in α we arrive at the linearized equations which govern the perturbations. The first-order solutions are further expressed in terms of normal modes with the wave vector $\mathbf{k} = (k_x, k_y)$ and frequency $\omega_{\mathbf{k}}$

$$f_1(x, y, z, t) = \hat{f}_1(z) \exp[i(k_x x + k_y y) - i\omega_{\mathbf{k}} t]. \quad (15)$$

By inserting the normal modes back into the linearized equations, the problem is eventually transformed into an eigenvalue problem for the frequency $\omega_{\mathbf{k}}$, generally a complex number of the form $\omega_{\mathbf{k}} = \text{Re}(\omega_{\mathbf{k}}) + i \text{Im}(\omega_{\mathbf{k}})$. It is seen from equation (15) that

$$f_1 \propto \exp[-i \text{Re}(\omega_{\mathbf{k}}) t] \exp[+i \text{Im}(\omega_{\mathbf{k}}) t]. \quad (16)$$

Therefore, an instability (exponential growth in time) is present when $\text{Im}(\omega_{\mathbf{k}}) > 0$. In some cases $\omega_{\mathbf{k}}$ is real for a while before developing a positive imaginary part. In other cases the onset of instability is right at $\omega_{\mathbf{k}} = 0$. The former case is known as overstability while the latter as static instability.

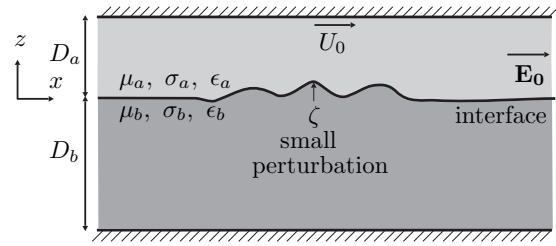


Figure 6. The simplified model with a single interface (a single ‘conveyor belt’) used to assess the instability regimes of our pump. Two shearing liquids are confined between two large (high aspect ratio) parallel plates in a Couette–Poiseuille flow. The liquids differ in dynamic viscosities, dielectric constants and conductivities. They are further exposed to a tangential electric field. The Debye layer is assumed negligibly thin so the driving EO velocity appears only as a boundary condition.

5.2. Shear-flow instability

Shear-flow instability is particularly relevant in the active part of the main channel, where the liquids are exposed to mutual stresses. Microfluidic shear flows between two viscous, immiscible liquids can result in a variety of regular droplet patterns, as the shear force (constant for a given relative velocity and a fixed geometry) overcomes the cohesive surface tension force, [16].

In our case, due to the conveyor-belt action, the two liquids flow between two large parallel plates in a Couette–Poiseuille setup, figure 6. In each liquid the governing equations are the Navier–Stokes equation and the continuity equation

$$\rho_{(i)} (\partial_t \mathbf{u}_{(i)} + \mathbf{u}_{(i)} \cdot \nabla \mathbf{u}_{(i)}) = -\nabla p_{(i)} + \mu_{(i)} \nabla^2 \mathbf{u}_{(i)}, \quad (17)$$

$$\nabla \cdot \mathbf{u}_{(i)} = 0, \quad (18)$$

where $i = a, b$ indicates liquid a and b , ρ is the density, p is the pressure, μ is the dynamic viscosity, and $\mathbf{u}(x, y, z) = (u, v, w)$ is the velocity field. Note that we did not include the gravitational body force as it is negligible in our microfluidic system¹.

When the linear stability analysis is performed on equations (17) and (18), we arrive at the Orr–Sommerfeld equations for two liquids, [17], and a set of eight boundary conditions. These include the no-slip velocity conditions at rigid boundaries and fairly complicated interface conditions—continuity of velocities and tangential stresses, and balance of normal stresses. The whole system is then solved for eigenfrequencies as mentioned earlier. The analytical procedure is rather involved. Here we apply the full description, found in [18–21], in the relevant limits.

An important conclusion from the analysis is that a difference between the viscosities of the two liquids cause the instability in shear flows at low Reynolds number. Once the viscosities differ, the relative thickness of the liquid layers becomes important, too.

We have estimated the onset of instability in the long-wavelength limit for the water–oil (a – b) system of figure 6. In figure 7 $\text{Im}(\omega_{\mathbf{k}})$ is shown as a function of the viscosity ratio μ_b/μ_a . The graphs are shown for three different thickness

¹ The ratio between gravitational and capillary force in the system is the Bond number, $Bo = (\rho^{(2)} - \rho^{(1)})ga^2/\gamma$. If we consider oil and water, and $a = 10 \mu\text{m}$ is the width of the main channel in the pump, we get $Bo \sim 10^{-6}$. This allows the liquids in the pump to flow sidewise.

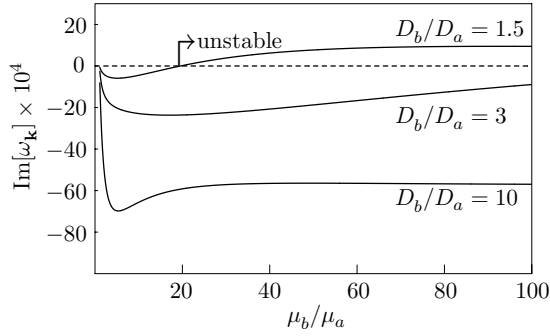


Figure 7. A shear-flow stability study of a water–oil system (liquids a and b , respectively, in figure 6). For three different values of the thickness ratio D_b/D_a the imaginary part of the frequency $\text{Im}[\omega_k]$ is plotted as a function of the viscosity ratio μ_b/μ_a for an EO velocity $u_{eo} = 1 \text{ mm s}^{-1}$, a surface tension $\gamma = 18 \times 10^{-3} \text{ N m}^{-1}$, and a zero counter-pressure. For $D_b/D_a = 1.5$, instability sets in for $\mu_b/\mu_a > 20$ where $\text{Im}[\omega_k] > 0$. This is an example how an increase in viscosity actually enhances instability. Increasing the oil thickness, the window of stability is increased.

ratios D_b/D_a . Keeping D_a constant, stability increases with increasing thickness ratio, while it decreases with increasing viscosity ratio, except that in the limit of very large viscosity ratios the system becomes stable again.

The above results can be used to operate the pump within a given stability window. If D_a is as thin as a few Debye lengths, the pump will practically always be stable with respect to the shear flow.

5.3. Electrohydrodynamic (EHD) instability

Another important aspect is electrohydrodynamic (EHD) instability present when liquids of different dielectric constants and conductivities are exposed to electric fields. Numerous studies of EHD instability have been published over the years, e.g. [22–27], and more recently with special attention to microfluidics [18, 19, 28].

In this brief account of EHD instability we use the formalism from [18, 25], and apply it in the relevant limits with regard to our pump. Essentially, the equations governing electric fields and charge transport in each liquid need to be added to equations (17) and (18)

$$\nabla \cdot (\epsilon_{(i)} \mathbf{E}_{(i)}) = \rho_{(i)}^{\text{el}}, \quad (19)$$

$$\nabla \times \mathbf{E}_{(i)} = 0, \quad (20)$$

$$\nabla \cdot (\sigma_{(i)} \mathbf{E}_{(i)} + \rho_{(i)}^{\text{el}} \mathbf{v}_{(i)}) + \partial_t \rho_{(i)}^{\text{el}} = 0, \quad (21)$$

where ϵ is the dielectric constant, σ is the conductivity, ρ^{el} is the free charge density and \mathbf{E} is the electric field in each liquid. In equations (19)–(21) it is assumed that magnetic effects are negligible and that Ohm’s law of conduction is valid. The interface boundary conditions are expanded to account for electric stresses and conservation of free charge.

There are two main effects which influence the behavior of the interface between two liquids in an electric field. First, there are polarization forces that act normally on the interface, due to a difference in the dielectric constants. And second, there are tangential shear forces resulting from the free charges that relax at the interface, due to a difference in the conductivities. Relevant in microfluidics are effects involving

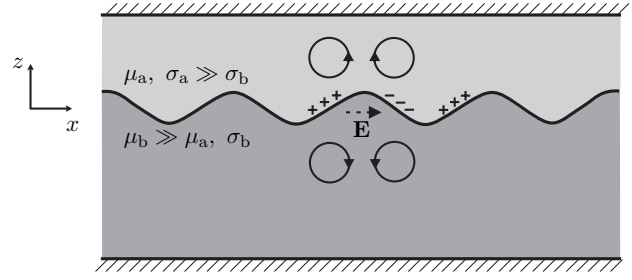


Figure 8. Overstability mechanism in the pump. A perturbation of the interface between a conducting and a nonconducting liquid results in the accumulation of free surface charge. As it screens the imposed field from the conducting region, the charge is shifted in phase with respect to the perturbation [25]. Charge motion in a tangential field induces shear stresses in the liquids above and below, which can either stabilize or further destabilize the interface. In the depicted case $\mu_b \gg \mu_a$ and $\sigma_a \gg \sigma_b \approx 0$, so the interface will be stabilized.

Debye layers, but these are out of the scope of this preliminary account.

In our pump a thin layer of conducting liquid drags a viscous nonconducting dielectric liquid. There is a huge difference in conductivities and the liquids are exposed to a tangential electric field. Therefore, the shear forces due to free charges will play the most important role, possibly causing overstability or oscillatory instability, which we now assess.

In equilibrium no current passes through the unperturbed interface and no free charges accumulate on it. However, interface perturbations cause a change in the fields which in turn attract free charges at the interface. The charges position themselves to shield out the imposed field from the high conductivity region. As the charges move under the influence of electric field, shear stresses are passed onto the liquids below and above the interface, creating fluid cells, figure 8. If the liquids have the same viscosity these effects will cancel each other, but a difference in viscosities will make these cells to further deform or possibly suppress the perturbations.

We now make a use of the general eigenvalue solution (equation (34) in [25]) applicable to our problem sketched in figure 6. In the two-liquid viscous pump the two liquids are such that the conductivities $\sigma_a \gg \sigma_b$ which results in a very short charge relaxation time $\tau = (\epsilon_a + \epsilon_b)/\sigma_a$. We are interested in the viscosity limit $\mu_a \ll \mu_b$, i.e., when the more conducting liquid is much less viscous. An involved analysis gives for the critical field that induces overstability

$$E_c^2 = -\frac{2\mu_b\sigma_a}{\epsilon_b(\epsilon_a + 3\epsilon_b)}. \quad (22)$$

The minus sign indicates that in this limit no field can induce the instability. In light of figure 8, the imparted viscous stresses, pronounced in the more viscous liquid, act to suppress the interface deformation. On the other hand, if the conducting liquid is the one with a much higher viscosity (e.g. pumping of a gas), the critical field is positive and given by

$$E_c^2 = \frac{2\mu_a\sigma_a}{\epsilon_b(\epsilon_b + 3\epsilon_a)}, \quad (23)$$

or, for $\epsilon_a \gg \epsilon_b$,

$$E_c = \left(\frac{2\mu_a\sigma_a}{3\epsilon_a\epsilon_b} \right)^{\frac{1}{2}}. \quad (24)$$

When equation (24) is evaluated for common fluids, the fields are on the order of 10^6 V m^{-1} . In the studied example (operating voltage 10 V), the electric field within the main channel is $E = 4 \times 10^4 \text{ V m}^{-1}$, a much lower value.

The above results show that our viscous liquid pump is stable with respect to the EHD overstability. In the case when a more viscous, nonconducting liquid is pumped, stability is always present whereas in the case of low-viscosity dielectrics the critical fields are much higher than the operating ones. In passing we remark that the normal polarization forces also stabilize the interface when the liquid of higher conductivity has also a higher dielectric constant, which is usually the case.

5.4. Capillary instability

The pressure drop over the interface between two immiscible fluids is given by the Laplace equation

$$\Delta P = \gamma \left(\frac{1}{r_1} + \frac{1}{r_2} \right), \quad (25)$$

where γ is the surface tension while r_1 and r_2 are the principal radii of curvature. We take the width a and depth D of a valve channel to correspond to $2r_1$ and $2r_2$, respectively. In a high aspect ratio valve $a \ll D$, hence only the width a contributes to the capillary pressure.

The pressure induced below the valves in the two-liquid pump will tend to deform the interface according to equation (25), as simulated in figure 3(c). We now estimate under which conditions the breaking of two streams sketched in figure 5 could occur and why. For an oil–water interface $\gamma = 18 \times 10^{-3} \text{ N m}^{-1}$ and a valve width of $a = 1 \mu\text{m}$ it takes a pressure of 36 kPa to push an oil droplet through the valve opening.

The backpressure capacity of the pump is $\Delta p = 30 \text{ Pa}$ for 10 V using a conducting liquid. In the case of the water–oil interface the pressure increases to $9 \text{ kPa} \times 0.1 = 900 \text{ Pa}$ at 10 V due to the higher viscosity of oil ($\mu_{\text{oil}} = 300\mu_{\text{water}}$) and the reduced oil velocity, see figure 3(d). This value is still lower than the capillary pressure thus the interface will be stable in normal operation.

If the interphase breaks due to instabilities, e.g., in the case of lower surface tension, oil droplets may enter the outlet valve to account for the mass conservation ($q_1 \neq q_2$). Hence the pinched-off conducting droplets shown in figure 5. Similar effects of variable flow resistance on droplet break-up is demonstrated in [29]. Obviously, such behavior would eventually disrupt the pumping operation.

We conclude this section by saying that the pressure valves will prevent an immiscible liquid from entering them if the backpressure capacity of the pump is smaller than the capillary pressure associated with the valve openings.

6. Conclusion

We have presented a novel electro-osmotic pump which can be used to pump nonconducting liquids by the viscous drag of a conducting secondary liquid. In order to achieve a

viable pump, the liquids must be immiscible, stability must be ensured and three main features need to be employed: a favorable under-pressure, pressure valves and an optimized potential drop.

The flow rate–pressure characteristic of the two-liquid viscous EO pump largely depends on the geometrical factors and can be significantly enhanced by advanced etching techniques. The pump design still works for miscible liquids, but here the working liquid gets mixed with the pumping liquid due to diffusion.

Numerical simulations and the equivalent circuit model of the design presented here yield a maximal flow rate per volt of $0.03 \text{ nL V}^{-1} \text{ s}^{-1}$ and a backpressure capacity per volt of $3\text{--}90 \text{ Pa V}^{-1}$ depending on the liquids in the pump. These values are quite small and the pump is therefore suited for precise flow manipulation rather than pumping bulk volumes.

Three effects play a role with regard to the stability of the pump: (1) shear-flow instability happens only when the liquids differ in viscosities and is suppressed when the conducting-liquid layer is thin compared to the nonconducting one. (2) Electrohydrodynamic overstability is suppressed when the conducting liquid has a much smaller viscosity than the nonconducting liquid. (3) Capillary instability is suppressed by a large surface tension and by a large value of the capillary pressure stemming from a small width of the pressure valves.

Future work involves time-dependent two-phase simulations. Such work could give valuable information about priming of the pump. We are currently preparing papers containing the detailed mathematical analysis of the stability mechanisms [19, 20]. Finally a prototype should be manufactured. Because of the possibility of pumping all types of liquids in a precise and controlled manner, the described concept and design appear promising.

Acknowledgments

This work is partly supported by the Danish Technical Research Council, μTAS Frame Program Grant No. 26-00-0220.

References

- [1] Laser D J and Santiago J G 2004 A review of micropumps *J. Micromech. Microeng.* **14** R35–R64
- [2] Takamura Y, Onoda H, Inokuchi H, Adachi S, Oki A and Horiike Y 2001 *Proc. μTAS 2001 (Monterey CA, USA, Oct.)* pp 230–2
- [3] Morf W E, Guenat O T and de Rooij N F 2001 *Sensors Actuators B* **72** 266
- [4] Chen C H and Santiago J G 2002 *J. Microelectromech. Syst.* **11** 672–83
- [5] Yao S, Mikkelsen J C and Santiago J G 2001 *Proc. IMECE: ASME International Mechanical Engineering Congress and Exposition (New York, Nov.)*
- [6] Zeng S, Chen C H, Mikkelsen J C and Santiago J G 2001 *Sensors Actuators B* **79** 107–14
- [7] Alarie J P, Jacobson S C, Scott Broyles B, McKnight T E, Culbertson C T and Ramsey J M 2001 *Proc. $\mu\text{TAS}'01$ (Monterey, CA, USA, Oct.)* pp 131–2
- [8] Levine S, Marriott J R and Robinson K 1974 *J. Chem. Soc. Faraday Trans.* **II** 1–11
- [9] Mogensen K B, Eriksson F, Nikolajsen R P H and Kutter J P 2004 *Proc. $\mu\text{TAS}'04$ (Malmö, Sweden, Sept.)* vol 1 pp 39–41

- [10] Brask A, Bruus H and Kutter J P 2004 *Proc. μ TAS'04 (Malmö, Sweden, Sept.)* vol 2 pp 136–8
- [11] Patankar N A and Hu H H 1998 *Anal. Chem.* **70** 1870–81
- [12] Jensen M J, Garstecki P, Fuerstman M, Bruus H, Whitesides G M and Stone H A 2004 *Proc. μ TAS'04 (Malmö, Sweden, Sept.)* vol 1 pp 626–8
- [13] Brask A, Goranović G and Bruus H 2003 *Sensors Actuators B* **92** 127–32
- [14] White F M 1991 *Viscous Fluid Flow* 2nd edn (Singapore: McGraw-Hill)
- [15] Chandrasekhar S 1961 *Hydrodynamic and Hydromagnetic Stability* (Oxford: Oxford University Press)
- [16] Thorsen T, Roberts R W, Arnold F H and Quake S 2001 *Phys. Rev. Lett.* **86** 4163–6
- [17] Drazin P G and Reid W H 1991 *Hydrodynamic Instability* (Cambridge: Cambridge University Press)
- [18] Goranović G 2003 *PhD Thesis* Technical University of Denmark online at <http://www.mic.dtu.dk/research/MIFTS>
- [19] Goranović G, Sørensen M P, Brøns M and Bruus H 2004 *Proc. μ TAS'04 (Malmö, Sweden, Sept.)* vol 1 pp 617–9
- [20] Goranović G, Sørensen M P, Brøns M and Bruus H 2004 in preparation
- [21] Yih C-S 1967 *J. Fluid. Mech.* **27** 337–52
- [22] Rayleigh Lord 1882 *Phil. Mag. Ser.* **5** 184–6
- [23] Melcher J R 1963 *Field-Coupled Surface Waves: a Comparative Study of Surface-Coupled Electrohydrodynamic and Magneto hydrodynamic Waves* (Cambridge MA: MIT Press)
- [24] Melcher J R and Smith C V Jr 1969 *Phys. Fluids* **12** 778–90
- [25] Melcher J R and Schwarz W J Jr 1968 *Phys. Fluids* **11** 2604–16
- [26] Saville D A 1997 *Annu. Rev. Fluid Mech.* **29** 27–64
- [27] Mestel A J 1994 *J. Fluid Mech.* **274** 93–113
- [28] Lin H, Storey B D, Oddy M H, Chen C-H and Santiago J G 2004 *Phys. Fluids* **16** 1922–35
- [29] Link D R, Anna S L, Weitz D A and Stone H A 2004 *Phys. Rev. Lett.* **92** 54503

Appendix D

Paper published in Sens. Actuators B

Title

Theoretical analysis of the low-voltage cascade electroosmotic pump

Authors

Anders Brask, Goran Goranović and Henrik Bruus

Reference

Sens. Actuators B, (2003), **92**, 127-132.

Theoretical analysis of the low-voltage cascade electro-osmotic pump

Anders Brask, Goran Goranović, Henrik Bruus*

Mikroelektronik Centret (MIC), Technical University of Denmark, DK-2800 Kongens Lyngby, Denmark

Received 11 July 2002; received in revised form 19 December 2002; accepted 17 January 2003

Abstract

The recently published experimental results obtained by Takamura et al. [Y. Takamura, H. Onoda, H. Inokuchi, S. Adachi, A. Oki, Y. Horiike, in: J.M. Ramsey, A. van den Berg (Eds.), Proceedings of the μ TAS 2001, Monterey, CA, USA, Kluwer Academic Publishers, Dordrecht, 2001, p. 230], on their low-voltage cascade electro-osmotic pump are analyzed using two different theoretical approaches. One is the semi-analytical equivalent circuit theory involving hydraulic resistances, pressures, and flow rates. The other is a full numerical simulation using computational fluid dynamics. These two approaches give the same results, and they are in good qualitative agreement with the published data. However, our theoretical results deviate quantitatively from the experiments. The reason for this discrepancy is discussed. © 2003 Elsevier Science B.V. All rights reserved.

PACS: 47.11.+j; 47.60.+i; 47.85.Dh; 82.45

Keywords: Electro-osmotic pump; Equivalent circuit model; CFD simulation

1. Introduction

Micropumps play a key role in the quest for fabricating versatile, cheap, and highly efficient microfluidic lab-on-a-chip devices. In this growing field especially micropumps based on electroosmotic flow (EOF) [1–3] are becoming important [4–9]. They contain no moving parts and are compact. Moreover, they are relatively easy to integrate in microfluidic circuits during fabrication.

One major drawback in the conventional design of EOF micropumps is the use of high voltage to drive the pump. The invention in 2001 of the low-voltage cascade EOF pump by Takamura et al. [5] therefore marks an interesting development in the field. In the future, EOF pumps may be powered by battery; and hence, portable.

The aim of our work is two-fold. (1) We want to provide the first theoretical analysis of the experimental results obtained by Takamura et al. [5,10]. (2) Using computational fluid dynamics (CFD) we want to demonstrate that the complex EOF pump is adequately described by the semi-analytical equivalent circuit theory involving hydrodynamic resistances, pressures, and flow rates. Both calculational methods are approximate, but since they are independent

and yield comparable results, we have gained confidence in our theoretical results.

2. Principles of the EOF pump

To set the stage for our analysis we briefly recapitulate the working principles of the low-voltage cascade EOF pump [5]. The pump is designed to work as an effective pressure source for low applied voltages. The layout of the pump is shown in Fig. 1.

The main principle is to connect multiple EOF pumps in series in order to accumulate pressure. Each elementary EOF pump (denoted a step) consists essentially of a narrow channel section, marked B in Fig. 1, containing 10 parallel channels, followed by a wide channel section, marked C in Fig. 1, containing a single channel. The EOF in the narrow channel section acts as a high pressure pump with forward electric field. In the wide channel section the electric field is reversed, but here the channel is so wide that the induced back pressure is small compared to the previous pressure. After flowing through one such pump step the accumulated voltage is thus zero, while an appreciable pressure is maintaining a net flow. This ensures EOF pumping using a low operating voltage, indeed an attractive feature allowing the pump to be operated with a battery and thus to be portable. Furthermore, it is more safe to use low voltages.

* Corresponding author. Tel.: +45-4525-6399; fax: +45-4588-7762.
E-mail address: bruus@mic.dtu.dk (H. Bruus).

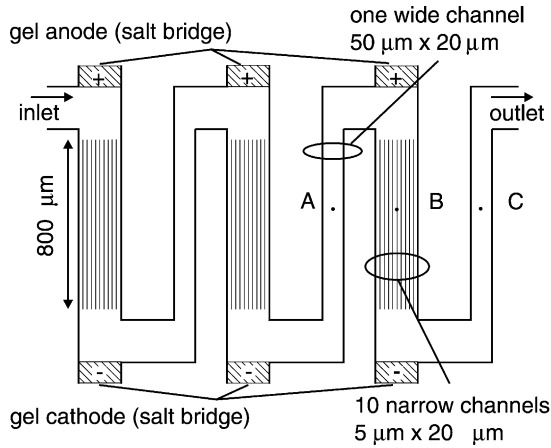


Fig. 1. Top view of the low-voltage cascade EOF pump with three steps (adapted from Fig. 3 in [5]). The total pressure is proportional to the number of steps. The EOF is driven through many parallel narrow channels by a forward electric field and through one wide channel with a reversed electric field. A net flow is thus generated without accumulation of voltage.

The disadvantage of a cascade pump is the extra complexity of the many electrodes.

We begin our analysis by noting that water at room temperature has the kinematic viscosity $\nu = 10^{-6} \text{ m}^2/\text{s}$, and when, as in the experiment, it flows with the velocity $u \approx 10^{-3} \text{ m/s}$ through a channel of width $D = 50 \text{ }\mu\text{m}$, the Reynolds number, Re , is minute:

$$Re = \frac{uD}{\nu} = 0.05. \quad (1)$$

For such a low Reynolds number the flow is laminar and the viscous forces are dominant. In the case of uniform flow, i.e. zero spatial derivatives in the flow direction, the Navier-Stokes equation becomes linear.

In this limit, for a steady-state flow through a channel with a hydraulic resistance R_{hyd} , the flow rate Q_{hyd} induced by the pressure drop Δp_{hyd} is

$$Q_{\text{hyd}} = \frac{\Delta p_{\text{hyd}}}{R_{\text{hyd}}}. \quad (2)$$

Polar liquids offer another possibility beyond pure hydrodynamics to generate a flow: namely the electrically driven EOF [1–3]. Ions in the liquid form a thin ($<100 \text{ nm}$) electric double layer, the Debye layer, at the walls of the channel, and when an electric potential drop $\Delta\phi_{\text{eo}}$ is applied along the channel an EOF is initiated. In the limit of infinitely thin Debye layers, the flow velocity u_{eo} at the walls is given by the Smoluchowski expression

$$u_{\text{eo}} = \mu_{\text{eo}} \frac{\Delta\phi_{\text{eo}}}{L}, \quad (3)$$

where μ_{eo} is the so-called electroosmotic mobility, and L the length of the channel. For a pure EOF, the flow rate Q_{eo} in a channel with cross-sectional area A is given by

$$Q_{\text{eo}} = u_{\text{eo}}A = \mu_{\text{eo}} \frac{\Delta\phi_{\text{eo}}}{L} A \frac{R_{\text{hyd}}}{R_{\text{hyd}}} \equiv \frac{\Delta p_{\text{eo}}}{R_{\text{hyd}}}, \quad (4)$$

where R_{hyd} and the EOF pressure Δp_{eo} is introduced in the second and third equality, respectively, so that Q_{eo} appears as Q_{hyd} in Eq. (2). In accordance with [6], Δp_{eo} is thus defined by:

$$\Delta p_{\text{eo}} = \mu_{\text{eo}} \Delta\phi_{\text{eo}} R_{\text{hyd}} \frac{A}{L} = \mu_{\text{eo}} \Delta\phi_{\text{eo}} R_{\text{hyd}} \frac{\rho_{\text{el}}}{R}, \quad (5)$$

where the geometry ratio A/L equals the ratio between the electric resistivity ρ_{el} of the liquid phase and the electric resistance R of the channel.

Equivalently, Δp_{eo} can be defined as the hydraulic back pressure needed to balance an EOF, i.e. $|Q_{\text{eo}}| = |Q_{\text{hyd}}|$. The total flow rate Q of a channel with both a pressure-driven flow and an EOF is simply

$$Q = Q_{\text{eo}} + Q_{\text{hyd}} = \frac{\Delta p_{\text{eo}} + \Delta p_{\text{hyd}}}{R_{\text{hyd}}}. \quad (6)$$

Likewise, the resulting velocity profile is given by a superposition of the velocity profiles of the EOF and the pressure-driven flow, respectively [2].

Consider a pump in a fluidic network. If the back pressure Δp_{hyd} is zero, the flow is denoted a "free run flow" and the corresponding flow rate is termed Q_{max} . The counter pressure needed to stop the flow (i.e. $Q = 0$) through the entire pump is denoted the maximum back pressure p_{max} .

3. Analysis of the EOF pump

From Eq. (5), it follows that the EOF-induced pressure buildup is very large in the narrow channel section, and thus the flow profile in this section becomes only slightly deformed under the influence of the actual back pressure. The resulting velocity profile u_1 , shown in Fig. 2, is a sum of a large, positive

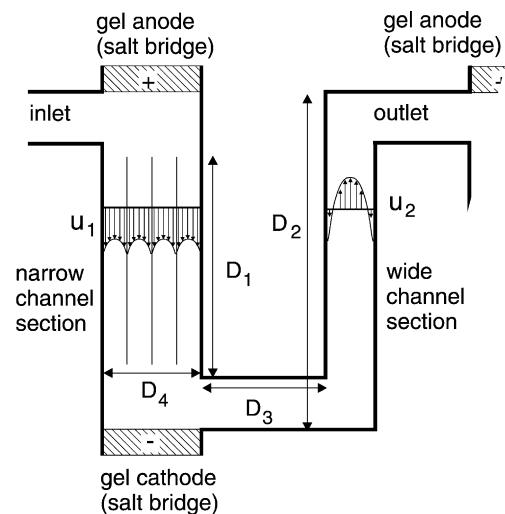


Fig. 2. Simplified schematics of one step of the cascade EOF pump shown in Fig. 1. The flow profiles in both narrow and wide channels are shown. There are 10 channels in the narrow channel section, but for clarity only 4 are depicted. Even though the flow is reversed near the wall in the wide channel, the net flow is still positive. The parameters taken from [5] are: $D_1 = 800 \text{ }\mu\text{m}$, $D_2 = 1230 \text{ }\mu\text{m}$, $D_3 = 170 \text{ }\mu\text{m}$, and $D_4 = 185 \text{ }\mu\text{m}$.

and flat EOF velocity profile and a small, negative and parabolic back pressure velocity profile. The pressure buildup in the narrow channel section is denoted Δp_{eo}^N .

In the wide channel the electric field is reversed. A part of the pressure generated in the narrow section is therefore used both for overcoming the reversed, small, and flat EOF profile and for driving the flow by pressure. The resulting velocity profile is the large, forward parabolic-like velocity profile u_2 shown in Fig. 2. It is evidently imperative to make the channel width considerably larger in this section to keep its back pressure to a minimum. The pressure drop in the wide channel section is denoted Δp_{eo}^W .

The final pressure buildup Δp_{step}^{max} along the whole step is the EOF pressure buildup in the narrow channel section minus the back pressure drop in the wide channel section,

$$\Delta p_{step}^{max} = \Delta p_{eo}^N - \Delta p_{eo}^W. \quad (7)$$

3.1. Equivalent circuit theory

The concepts from the previous section can be used to analyze the pump using the so-called equivalent circuit theory. In this theory, the hydraulic resistance of a fluidic network is calculated by representing individual sections with equivalent hydraulic resistors using the usual rules for series and parallel resistors. The flow rate and the pressure drop for a hydraulic resistor are related by Eq. (2). For details see [6].

The equivalent circuit theory is only exact for a uniform and laminar flow. Hence, it is not possible to analyze the flow near a bend. In the following analysis the bends are neglected, an approximation justified in Section 3.2 by CFD simulation.

The first step is to find the equivalent diagram for the pump. It consists of a parallel coupling of $N = 10$ identical resistors $R_{hyd,1}$ followed by $R_{hyd,3}$ and $R_{hyd,2}$ in series as shown in Fig. 3b. For a single rectangular channel of width W and height H , R_{hyd} is given by [6],

$$R_{hyd} = \frac{12\eta LH^{-4}}{(W/H) - \sum_{m=0}^{\infty} (192/(\pi^5(2m+1)^5)) \tanh [((2m+1)\pi W)/2H]}, \quad (8)$$

where η is the dynamic viscosity. $R_{hyd,1}$ and $R_{hyd,2}$ are then computed using Eq. (8). The short channel connecting the narrow and wide channel sections can safely be neglected,

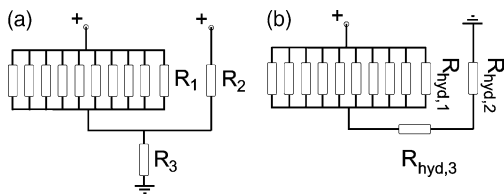


Fig. 3. (a) The equivalent electrical circuit used in the calculation of potential drop across the EO section. (b) The slightly different equivalent circuit for the fluidic network used in the calculation of flow rates. There are $N = 10$ narrow channels each with the hydraulic resistance $R_{hyd,1}$. In our calculations $R_{hyd,3}$ is neglected.

since $R_{hyd,3} \ll R_{hyd,1}, R_{hyd,2}$. The total hydraulic resistance R_{hyd}^{total} is therefore given as

$$R_{hyd}^{total} = N^{-1}R_{hyd,1} + R_{hyd,2}. \quad (9)$$

To drive the EOF an external electrical potential, $\Delta\phi_{ch}$, is applied to the resistor network (Fig. 3a). Only a fraction α of $\Delta\phi_{ch}$ is dropped over the EOF channels. This effective potential drop is denoted $\Delta\phi_{eo}$,

$$\Delta\phi_{eo} = \alpha \Delta\phi_{ch}. \quad (10)$$

Using the circuit diagram we determine α . The electrical resistance of a single rectangular channel with length L , width W , and height H is given by

$$R = \rho_{el} \frac{L}{HW}. \quad (11)$$

Combining this with the actual geometry of Fig. 1, it follows that

$$\alpha = \frac{(N/R_1 + 1/R_2)^{-1}}{(N/R_1 + 1/R_2)^{-1} + R_3} = 0.885. \quad (12)$$

The actual applied potential $\Delta\phi_{app}$ does not equal $\Delta\phi_{ch}$ because further potential drops occur in the gel electrodes. Hence, $\Delta\phi_{eo}$ is unknown but could have been estimated if the electrical current and conductivity of the liquid had been measured experimentally.

At this point the EOF pressures Δp_{eo}^W , Δp_{eo}^N , and Δp_{step} can be found for a given potential. However, it remains to verify the validity of the approximate equivalent circuit theory. This is done by numerical simulations in the following.

3.2. Computational fluid dynamics

A full numerical simulation was performed using the commercial computational fluid dynamics program Coven-

tor 2001.3. The program can simulate EOF in the limit of infinitely thin Debye layers. The electric potential is calculated first, and by the Smoluchowski relation Eq. (3) it is used to establish the boundary conditions for the velocity field at the walls. The accuracy of the CFD could be measured for straight channels with rectangular cross-section, since there the equivalent circuit model gives analytical answers.

In order to save calculation time, it is important to identify the minimal computational domain. Only one pump step needs to be analyzed. Further simplifications can be achieved by symmetry considerations. Clearly, the pump is symmetric about the horizontal plane at half the channel depth. Due to the very low Reynolds number, $Re < 0.05$, the flow is said to be creeping. Numerical investigation by Yang

et al. [11] showed that for a 90° bend, inertial effect was negligible for $Re < 5$. Consequently, it does not matter which way the liquid flows. The flow pattern in the first half of a pump step (e.g. between A and B in Fig. 1) therefore equals that in the second half (e.g. between B and C in Fig. 1). Hence, only half of the computational domain needs to be considered. This was verified by a full-geometry simulation. The flow rate and pressure buildup for the complete pump step are twice the values obtained using the symmetry-reduced geometry.

The CFD simulation was done with various grids to find those yielding grid-independent results. We focused especially on problems at the corners, since they are known to be problematic [12]. We ended using a grid containing 10^5 rectangular cells with 14×7 cells in each cross-section. The CFD results for this grid matched the analytical circuit model within 5%.

4. Results and discussion

4.1. Velocity profiles

A simulation of the low-voltage cascade EOF pump gave the velocity profiles depicted in Fig. 4. There is one profile for the wide channel, and one for a single narrow channel. The profiles have been extracted from the symmetry plane. The CFD program solves the Poisson equation for a given potential drop $\Delta\phi_{ch}$ and finds that the electric fields are slightly different in the wide and narrow channels. In the circuit model they are assumed to be the same. The calculated velocity profiles at two positions are sketched in Fig. 2.

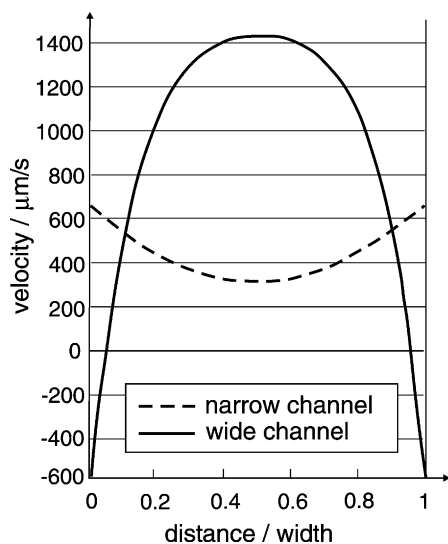


Fig. 4. CFD simulated velocity profiles at the symmetry plane in a wide and a narrow channel. The velocity at the walls is the EOF velocity. The parameters are: $\eta = 1.00 \times 10^{-3}$ Pa s, $\mu_{eo} = 0.06$ mm²/(V s), and $\Delta\phi_{ch} = 10$ V.

4.2. Comparison with experiments

The circuit model is now used to calculate the back pressure p_{max} and the EOF velocity u_{eo} as a function of the potential drop. Unfortunately, neither the actual potential drop $\Delta\phi_{ch}$ nor the EOF mobility μ_{eo} was measured in the experiment. However, both back pressure and flow velocity depend linearly on the product $\mu_{eo} \Delta\phi_{ch}$, and, as we shall see, this makes a comparison between experiments and theory possible.

In the case of a 15-step cascade pump, Takamura et al. [5] measured a max back pressure of 800 Pa and for the same voltage and under free run conditions, a max velocity $u_{max} = 0.50$ mm/s. The velocity measurements were conducted in the last wide section, which had no electric field. Hence, the flow is solely pressure driven.

The relation between the back pressure and the product $\mu_{eo} \Delta\phi_{ch}$ is found using Eqs. (5) and (7), and it is plotted in Fig. 5. From the figure, it is found that the measured 800 Pa corresponds to $\mu_{eo} \Delta\phi_{ch} = 0.114$ mm²/s. Using this value the model predicts the flow rate $Q_{max} = 0.110$ nl/s. From this flow rate, the maximum velocity u_{max} may be calculated in the wide channel section.

Using the aspect ratio as a variable parameter, we performed a general analysis of the relation between flow rates and maximal flow velocities in rectangular channels with cross-section area A . For the actual aspect ratio $W/H = 2.5$ we found a numerical factor 0.52:

$$u_{max} = \frac{Q_{max}}{0.52A} = 0.21 \text{ mm/s}, \quad (13)$$

where $A = 50 \times 20 \mu\text{m}^2$. This velocity, found both by simulation and by the circuit model, deviates by a factor 2.4 from the measured 0.50 mm/s.

In [5], results from a 6-step and 15-step pump are presented. The back pressure measurements give 380 and 860 Pa for the 6-step and 15-step pump, respectively, at $\phi_{app} = 25$ V. The corresponding ratio is then $860/380 = 2.26$ which should be compared with $15/6 = 2.5$. Hence, it can be concluded that the pressure is not accumulated linearly with the number of steps in contrast to theoretical expectations. The deviation may be within the range of uncertainty for the pressure measurements.

To obtain realistic estimates for the absolute values of the EOF pump parameters, we use some typical values for μ_{eo} and $\Delta\phi_{ch}$. The results for Q_{max} , p_{max} , and R_{hyd} obtained by model calculations and simulations are compared in Table 1

Table 1
Comparisons between equivalent circuit model and numerical simulation for a single pump step

	Q_{max} (nl/s)	p_{max} (Pa)	R_{hyd} (kg/(m ⁴ s))
Model	0.577	281.0	4.88×10^{14}
Simulation	0.560	274.0	4.89×10^{14}
Deviation	3%	2%	0%

Parameters: $\mu_{eo} = 0.06$ mm²/(V s), $\eta = 1.0 \times 10^{-3}$ Pa s, $\Delta\phi_{ch} = 10$ V.

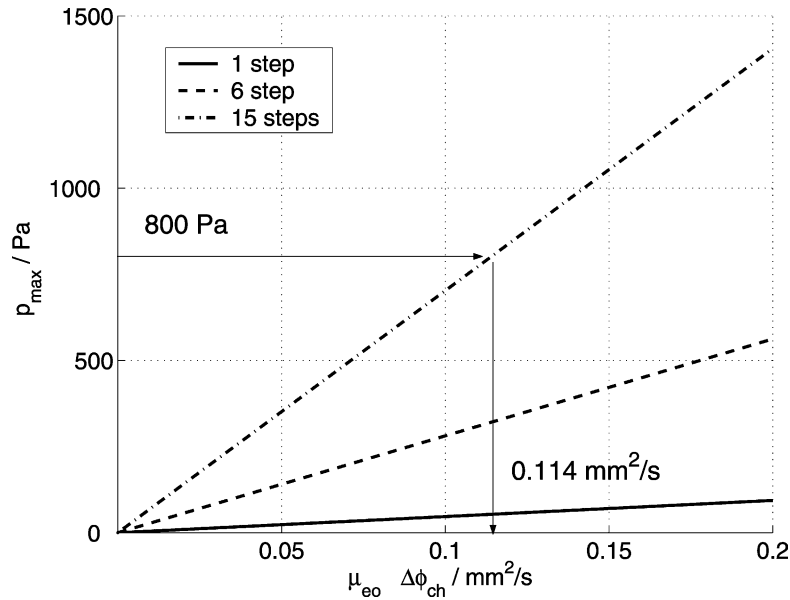


Fig. 5. Maximum back pressure as a function of $\mu_{eo} \Delta\phi_{ch}$. The pressures are calculated using the equivalent circuit theory. The one step slope is $468 \text{ Pa s} / \text{mm}^2$ for $\eta = 1.00 \times 10^{-3} \text{ Pa s}$, $\alpha = 0.885$. The measured pressure of 800 Pa leads to a value $\mu_{eo} \Delta\phi_{ch} = 0.114 \text{ mm}^2/\text{s}$.

for a given set of parameters. The two sets of results agree well. Calculations with $\mu_{eo} = 0.06 \text{ mm}^2/(\text{V s})$ give considerably larger pressures than those measured, e.g. 4200 Pa for the 15-step pump with $\Delta\phi_{ch} = 10 \text{ V}$. This indicates the possibility for improving the performance of the pump.

5. Discussions and conclusions

Discussions with Takamura [10] have led to the following conclusions regarding the discrepancies between experiment and theory.

- (1) The velocity mismatch of a factor of 2.4 is probably due to fabrication difficulties. The actual width of the narrow channels may have been as large as $8 \mu\text{m}$ instead of the design value of $5 \mu\text{m}$ [10]. Since $\Delta p_{eo} \propto W^{-2}$ for $W \ll H$, the pressure for a $8 \mu\text{m}$ wide channel is $(8/5)^2 = 2.6$ times smaller than for a $5 \mu\text{m}$ channel. This would lower the slopes of the lines in Fig. 5 and instead of reading off $0.114 \text{ mm}^2/\text{s}$ on the abscissa, we would get $0.296 \text{ mm}^2/\text{s}$. Using this number for $\mu_{eo} \Delta\phi_{ch}$, we obtain $u_{\text{max}} = 0.55 \text{ mm/s}$. This result agrees better with the observed 0.5 mm/s . A source for minor inaccuracies is the actual shape of the channel cross-section.
- (2) The pressure does not increase linearly with the number of stages. Two possible explanations of this observation are: (a) due to the design of the pump the individual gel electrodes do not have the same potential; (b) pressure-dependent hydraulic resistances of the gel electrodes, i.e. leaks in the gel electrodes increases with increasing pressure.

- (3) The experimental accuracy of the velocity and pressure measurements is 15–30%. Part of the discrepancies could therefore simply arise from inaccurate measurements.

The above explanations can account for the large quantitative deviations between theory and experiment, and the problems will be addressed in coming improved version of the low-voltage cascade EOF pump [10].

In summary, we have presented a simple analytical model for the low-voltage EOF pump obtained by using equivalent circuit theory. This approximate model has proved sufficient for making good estimates of the performance of the pump. Full CFD numerical simulations were made to verify the model and to provide more detailed information about the flow. The model and the simulations agree within 3%. Our theoretical analysis was compared to experimental results obtained by Takamura et al. [5], and good qualitative agreement was observed. However, a considerable quantitative deviation (a factor of 2.4) was found for values of calculated versus measured maximum velocity. The possible sources for this discrepancy were identified as inaccuracies in the measurement of various parameters (channel widths, velocities, and pressures) and pressure leakages.

Our work shows the advantage of theoretical analysis as a supplement to the experimental approach in the study of EOF pumps. Our pressure calculations indicate, for example, that there is room for improving the performance of the pump. We have also shown that, although approximate, the equivalent circuit model is applicable to the cascade EOF pump. This is mainly because the corrections from electrical and hydraulic corner effects are negligible. Use of the circuit model facilitates the analysis of the pump enormously.

Acknowledgements

We are grateful to Yuzuru Takamura and his colleagues at the University of Tokyo for their openness and great help in our discussions by email during this work and for providing us with experimental details not presented in [5]. We also thank our colleagues from the μ TAS project at Mikroelektronik Centret, especially Jörg Kutter, for support and stimulating discussions. This work was partly supported by the Danish Technical Research Council, μ TAS Frame Program Grant No. 9901288.

References

- [1] J.F. Osterle, *J. Appl. Mech.* 31 (1964) 161.
- [2] C.L. Rice, R. Whitehead, *J. Phys. Chem.* 69 (1965) 4017.
- [3] A. Manz, C.S. Effenhauser, N. Burggraf, D.J. Harrison, K. Seiler, K. Fluri, *J. Micromech. Microeng.* 4 (1994) 257.
- [4] P.H. Paul, D.W. Arnold, D.J. Rakestraw, *Proceedings of the μ TAS 1998*, Banff, Canada, 1998, p. 49.
- [5] Y. Takamura, H. Onoda, H. Inokuchi, S. Adachi, A. Oki, Y. Horiike, in: J.M. Ramsey, A. van den Berg (Eds.), *Proceedings of the μ TAS 2001*, Monterey, CA, USA, Kluwer Academic Publishers, Dordrecht, 2001, p. 230.
- [6] W.E. Morf, O.T. Guenat, N.F. de Rooij, *Sens. Actuators B-Chem.* 72 (2001) 266.
- [7] O.T. Guenat, D. Ghiglione, W.E. Morf, N.F. d Rooij, *Sens. Actuators B-Chem.* 72 (2001) 273.
- [8] S. Zeng, C.-H. Chen, J.C. Mikkelsen Jr., J.G. Santiago, *Sens. Actuators B-Chem.* 79 (2001) 107.
- [9] D.R. Reyes, D. Lossifidis, P.-A. Auroux, A. Manz, *Anal. Chem.* 74 (2002) 2623.
- [10] Experimental parameters not quoted in the original experimental paper were kindly provided by Dr. Y. Takamura, Univ. Tokyo.
- [11] R.-J. Yang, L.-M. Fu, Y.-C. Lin, *J. Colloid Interf. Sci.* 239 (2001) 98.
- [12] N.A. Patankar, H.H. Hu, *Anal. Chem.* 70 (1998) 1870.

Bibliography

- [1] H.A. Stone, A.D. Strook and A. Ajdari, *Annual Review of Fluid Mechanics*, 2004, **36**.
- [2] A. Manz, N. Graber and H.M. Widmer, *Sens. Actuators B*, 1990, **1**, 244.
- [3] D.J. Laser and J.G. Santiago, *J. Micromech. Microeng.*, 2004, **14**, R35-R64.
- [4] F. Kohlrausch, *Ann. Phys. Chem*, 1897, **62**, 209-239.
- [5] R.J. Hunter, *Zeta Potential in Colloidal Science: Principles and Applications*, Academic Press, London, 1981.
- [6] R.F. Probstein, *Physicochemical Hydrodynamics, An Introduction 2nd Edition*, John Wiley and Sons, Massachusetts Institute of Technology, 1994.
- [7] C.L. Rice and R. Whitehead, *J. Phys. Chem.*, 1965, **69**, 4017.
- [8] A. Brask, *Principles of electroosmotic pumps*, Master thesis, ISBN: 87-89935-31-4, 2002.
- [9] B.P. Mosier, R.W. Crocker, J.L. Rognlien and K.D. Patel, *Am. Soc. Mech. Eng., FED*, 2003, **259**, 511.
- [10] A. Brask, J.P. Kutter and H. Bruus, *Lab. Chip.*, 2005, **5**, 730-738.
- [11] A. Brask, J.P. Kutter and H. Bruus, *J. Adv. Nat. Sci.*, 2004, **5**, 423-430.
- [12] A. Brask, D. Snakenborg, J.P. Kutter and H. Bruus, *Lab. Chip.*, 2006, **6**, 280-288.
- [13] A. Brask, G. Goranović, M.J. Jensen and H. Bruus, *J. Micromech. Microeng.*, 2005, **15**, 883-891.
- [14] A. Brask, G. Goranović and H. Bruus, *Sens. Actuators B*, 2003, **92**, 127-132.
- [15] S. Yao, D. Huber, J.C. Mikkelsen and J.G. Santiago, *Proc. IMECE USA*, 2001, **3**, 639.
- [16] W.E. Morf, O.T. Guenat and N.F. de Rooij, *Sens. Actuators B*, 2001, **72**, 266.

- [17] O.T. Guenat, D. Ghiglione, W.E. Morf and N.F. de Rooij, *Sens. Actuators B*, 2001, **72**, 273.
- [18] P.K. Dasgupta and S. Liu, *Anal. Chem.*, 1994, **66**, 1792.
- [19] C.H. Chen, and J.G. Santiago, *J. Microelectromech. syst.*, 2002, **11**, 672.
- [20] Y. Takamura, H. Onoda, H. Inokuchi, S. Adachi, A. Oki and Y. Horiike, *Electrophoresis*, 2003, **24**, 185.
- [21] S. Zeng, C.H. Chen, J.C. Mikkelsen and J.G. Santiago, *Sens. Actuators B*, 2001, **79**, 107.
- [22] D.S. Reichmuth, G.S. Chirica and B.J. Kirby, *Sens. Actuators B*, 2003, **92**, 37.
- [23] W. Gan, L. Yang, Y.-Z. He, R.-H. Zeng, M.L. Cervera and M. Guardia, *Talanta*, 2000, **51**, 667.
- [24] S. Yao and J.G. Santiago, *J. Colloid Interface Sci.*, 2003, **268**, 133-142.
- [25] S. Yao, D.E. Hertzog, S. Zeng, J.C. Mikkelsen and J.G. Santiago, *J. Colloid Interface Sci.*, 2003, **268**, 143-153.
- [26] C.T. Culbertson, R.S. Ramsey and J.M. Ramsey, *Anal. Chem.*, 2000, **72**, 2285-2291.
- [27] M. Mulder, *Basic Principles of Membrane Technology 2nd Edition*, Kluwer Academic Publishers, Dordrecht, 1996.
- [28] H. Klank, J.P. Kutter and O. Geschke, *Lab Chip*, 2002, **2**, 242.
- [29] M. F. Jensen, M. Noerholm, L.H. Christensen and O. Geschke, *Lab Chip*, 2003, **3**, 302.
- [30] P. Vainshtein and C. Gutfinger, *J. Micromech. Microeng.*, 2002, **12**, 252.
- [31] D. Burgreen and F.R. Nakache, *J. Phys. Chem.*, 1964, **68**, 1084-1091.
- [32] Dr. Bernd Bauer, FuMA-Tech GmbH, Vaihingen an der Enz, Germany, private communications.
- [33] Minivalve International, Jaartsveldstraat 5a 7575 BP Oldenzaal, The Netherlands, www.minivalve.com.
- [34] J.E. Rehm, T.J. Shepodd and E.F. Hasselbrink, Proc. μ TAS 2001, Monterey, USA, p. 227-229.
- [35] E.F. Hasselbrink, T.J. Shepodd and J.E. Rehm, *Anal. Chem.*, 2002, **74**, 4913.
- [36] B.J. Kirby, D.S. Reichmuth, R.F. Renzi, T.J. Shepodd and B.J. Wiedenman, *Lab Chip*, 2005, **5**, 184.

- [37] T. M. Squires and S. R. Quake, *Rev. Mod. Phys.*, 2005, **77**, 977.
- [38] S. Zeng, C.-H. Chen, J. G. Santiago, J.-R. Chen, R. N. Zare, J. A. Tripp, F. Svec and J. M. J. Frechet, *Sens. Actuators B*, 2002, **82**, 209.
- [39] N. G. Green, A. Ramos, A. González, and A. Castellanos, H. Morgan, *J. Electrostat.*, 2001, **53**, 71.
- [40] V. Studer, A. Pépin, Y. Chen and A. Ajdari, *Analyst*, 2004, **129**, 944-949.
- [41] A. Ramos, H. Morgan, N. G. Green, A. González and A. Castellanos, *J. Appl. Phys.*, 2005, **97**, 084906-1
- [42] I-yuan Wei and Jerry Brewer, *AMP Journal of Technology*, 1996, **5**.
- [43] C. Goll, W. Bacher, B. Bustgens, D. Maas, R. Ruprecht and W.K. Schomburg, *J. Micromech. Microeng.*, 1997, **7**.
- [44] V. Studer, G. Hang, A. Pandolfi, M. Ortiz, W.F. Anderson, S.R. Quake, *J. App. Phys.*, 2004, **95**.
- [45] Warren C. Young, *Roarks Formulas for Stress and Strain, 6th Edition*, McGraw-Hill, Inc., New York 1989.
- [46] M. Stjernstrom and J. Roeraade, *J. Micromech. Microeng.*, 1998, **8**, 33-38.
- [47] M. J. Madou, *Fundamentals of Microfabrication, 2nd Edition*. CRC Press, Boca Raton, FL, 1997.
- [48] A. Ajdari, *Phys. Rev. E.*, 2000, **61**.
- [49] S.R. Yeh, M. Seul and B.I. Shraiman, *Nature (London)*, 1997, **386**, 57.
- [50] A. Ramos, H. Morgan, N.G. Green, A. Castellanos, *J. Phys. D.*, 1998, **31**, 2338.
- [51] A.D. Brown, C.G. Smith and A.R. Rennie, *Phys. Rev. E.*, 2000, **63**.
- [52] V. Studer, A. Pépin, Y. Chen and A. Ajdari, *Microelectron. Eng.*, 2002, **61**, 915.